



HAL
open science

Infrared magneto-spectroscopy of relativistic-like electrons in three-dimensional solids

Michael Hakl

► **To cite this version:**

Michael Hakl. Infrared magneto-spectroscopy of relativistic-like electrons in three-dimensional solids. Materials Science [cond-mat.mtrl-sci]. Université Grenoble Alpes, 2017. English. NNT : 2017GREAY085 . tel-01795505

HAL Id: tel-01795505

<https://theses.hal.science/tel-01795505>

Submitted on 18 May 2018

HAL is a multi-disciplinary open access archive for the deposit and dissemination of scientific research documents, whether they are published or not. The documents may come from teaching and research institutions in France or abroad, or from public or private research centers.

L'archive ouverte pluridisciplinaire **HAL**, est destinée au dépôt et à la diffusion de documents scientifiques de niveau recherche, publiés ou non, émanant des établissements d'enseignement et de recherche français ou étrangers, des laboratoires publics ou privés.

THÈSE

Pour obtenir le grade de

DOCTEUR DE LA COMMUNAUTÉ UNIVERSITÉ GRENOBLE ALPES

Spécialité : **Physique de la Matière Condensée et du Rayonnement**

Arrêté ministériel : 7 Août 2006

Présentée par

Michael Haki

Thèse dirigée par **Dr. Milan Orlita**
et codirigée par **Dr. Marek Potemski**

préparée au sein **Laboratoire National des Champs
Magnétiques Intenses, CNRS, Grenoble, France**

dans l'Ecole Doctorale de Physique

Infrared magneto-spectroscopy of relativistic-like electrons in three- dimensional solids

Thèse soutenue publiquement le **7 Décembre 2017**,
devant le jury composé de :

Dr. Denis Basko

Laboratoire de Physique et Modélisation des Milieux Condensés, CNRS,
Grenoble, France, Président

Prof. Sergey Ganichev

University of Regensburg, Allemagne, Rapporteur

Prof. Jerzy Łusakowski

University of Warsaw, Pologne, Rapporteur

Prof. Gloria Platero

Instituto de Ciencia de Materiales de Madrid, Espagne, Examineur

Dr. Frederic Teppe

Laboratoire Charles Coulomb, Montpellier, France, Examineur

Dr. Anne-Laure Barra

LNCMI, CNRS, Grenoble, France, Examineur



Acknowledgement

I would like to deeply acknowledge the thesis supervisor Dr. Milan Orlita for introducing me into Fourier infrared spectroscopy and into the domain of relativistic-like electrons in solids. I appreciate his patience, guidance into how to become an independent researcher, share of ideas and personal attitude that extends beyond the field of physics. It has also been a honour to be his first Ph.D. student.

My cordial gratitude belongs to the thesis advisor and the head of the semiconductor group Dr. Marek Potemski for the opportunity to pursuit a Ph.D. project and also for his suggestions, productive critics and proofreading of the manuscript.

I am thankful to the fellowship of the close colleagues for providing a friendly atmosphere and stimulating environment, in particular to my officemate Maciej Molas for his helpful advices and understanding, to Arthur Slobodeniuk for the invaluable theoretical explanations, to Gerard Martinez for the experience in the optical adjustments and the assistance during the measurements, to Benjamin Piot for the performing of the transport characterization, to Karol Nogajewski for the help with sample preparation and their manipulation, to Clemént Faugeras for the complementary Raman measurements, to Ivan Breslavetz and Eyub Yildiz for the technical support of the experimental instruments, to Jakub Kuba for the experiment automation, to Iris Crassee for her scientific contributions and abundant help, to Leonid Bovkun for the affinity and cooperation in the infrared laboratory and to Benoit Roberge, Miroslav Bartoš, Maciej Koperski, Johannes Binder, Ashish Arora, Zhiguo Chen, Younes Henni, Kristupas Tikuišis, Ivo Hlavička, Lucien Woguia, Łukasz Bala, Magdalena Grzeszczyk, Jan Wyzula and Diana Václavková.

Acknowledgement for to the collaboration on Cd₃As₂ project:

I am indebted to Sergueï Tchoumakov and Mark Goerbig from LPS, University Paris-Sud for the elaboration of k.p-theory with Landau level computations. I am also grateful to Ana Akrap and Iris Crassee from DQPM, University of Geneva for carrying out the absolute reflectivity measurements and to Jérôme Debray from the Néel Institute in Grenoble for an access to the polishing machines and instructive training and to Jiří Novák, Ondřej Caha from CEITEC, Brno for the crystallographic orientation. Further, the work would not be possible without the specimen growers E. Arushanov and A. Nateprov from the Institute of Applied Physics in Chisinau, Wei-Li Lee and Raman Sankar from the Institute of Physics in Taipei and Q. D. Gibson and R. J. Cava from the Department of Chemistry, Princeton University.

Acknowledgement for to the collaboration on Bi₃Se₂ project:

In regards to this project my appreciation goes to G. Martinez for the design of a photoluminescence setup, related measurements and also for his measurement of transmission in high magnetic fields on thin slabs. I also appreciate performing of transport measurements by B. A. Piot and a help of A. Slobodeniuk for theoretical advices in the behaviour of dichroism in the saturation regime. I am thankful to Lukáš

Ohnoutek from the Charles University in Prague for the measurement of the Faraday rotation at low magnetic fields, to Martin Veis for the development of the theory of the rotational mechanism. My thanks also go to Jiří Novák, Ondřej Čaha from CEITEC, Brno for crystallographic orientation and to the crystal growers Č. Drašar from the Faculty of Chemical Technology in Pardubice and to A. Materna, G. Strzelecka from the Institute of Electronic Materials Technology in Warsaw for providing their samples.

Acknowledgement for to the collaboration on HgTe project:

I thank to Laurens Molenkamp, Harmuth Buhmann, Christoph Brüne from the University of Würzburg for involving me into the project and in particular I am thankful to Philipp Leubner for the epitaxial growth of layers, to David Mahler for the supplementary transport measurement and to Roman Stepniewski from the Faculty of Physics in Warsaw for the help with data interpretation.

It is also my pleasure to thank all jury members - Dr. Denis Basko, Prof. Sergey Ganichev, Prof. Jerzy Łusakowski, Prof. Gloria Platero, Dr. Frederic Teppe and Dr. Anne-Laure Barra for the acceptance to review this thesis.

The author also conveys thanks to the staff of Laboratoire National des Champs Magnétiques Intenses for the hospitality and access to the installation and laboratory facilities, specifically to the secretaries for the help with the administration, to Robert Pankow, Julien Jousset for the user support, to Claude Mollard for the technical support in the mechanical workshop, to Fatima Rida and Ghenadie Novitchi for the support with chemistry and their kind encouragement throughout the research. I am also thankful to the Nanofab team in the Néel institute's cleanrooms.

This work was done under auspices of the Université Grenoble Alpes and was funded from the ERC project MOMB (No. 320590).

Abbreviations

ARPES	Angular resolved photoemission spectroscopy
B-field	Magnetic field
BHZ	Bernevig, Hughes and Zhang
BZ	Brillouin zone
CB	Conduction band
CF	Crystal field
CVD	Chemical vapour deposition
DFT	Density functional theory
DOS	Density of states
DP	Dirac point
E	Electron band
FR	Faraday rotation
FTIR	Fourier transform infrared spectroscopy
HH	Heavy hole band
IR	Infra-red
LH	Light hole band
LL	Landau level
MBE	Molecular beam epitaxy
MB	Moss-Burstein shift
NMR	Nuclear magnetic resonance
PL	Photoluminescence
SdH	Shubnikov-de Haas
SH	Spin-split hole band
SOC	Spin-orbit coupling
SS	Surface states
STM	Scanning tunnelling microscopy
THz	Terahertz
VB	Valence band
WP	Weyl point

List of selected symbols

A	Area, vector potential
B	Magnetic field
D	Density of states
E	Energy
\mathbf{E}	Electric field
\mathbf{e}	Polarization of light
e	Electron charge
g	g-factor
H	Hamiltonian
k, k_B	Momentum (in B -direction)
κ_B	Boltzmann constant
$L_{n \rightarrow n'}$	Energy of inter Landau level transition
m	Particle mass
N	Carrier density
P	Kane interband matrix parameter
V	Verdet constant
v	Velocity parameter
α	Fine-structure constant, T-parameter
Γ	Broadening, Dirac matrix
δ	Crystal field splitting
Δ	SOC parameter, halfgap
ε	Dielectric function
μ	Mobility
μ_B	Bohr magneton
ξ	Phase factor
χ	Chirality, valley index
σ	Conductivity, spin operator
Θ	Faraday angle
ζ	Degeneracy factor, inclination
ω	Photon frequency

Contents

Abstract (Eng)	3
Resumé (Fr)	7
1 Introduction	13
1.1 Preface	13
1.2 Origin of relativistic particles	14
1.3 Consequence of discrete symmetries	15
1.4 From Dirac to Kane model	16
1.5 Topological insulators and surface states	19
1.6 Optical response	22
1.7 Effect of quantization in magnetic field	24
2 Experimental technique	31
2.1 Infrared Fourier transform spectroscopy	31
2.2 Transport measurement	35
3 Magneto-optics of Cd₃As₂	39
3.1 The state of the art	39
3.2 Bodnar Hamiltonian at zero field	42
3.3 Landau level spectrum for Bodnar model in (001)-orientation	44
3.4 Sample preparation	46
3.5 Optical response at zero magnetic field	48
3.6 Transport measurement	55
3.7 Magneto-optics in a classical regime	58
3.8 Cyclotron resonance in a quantum regime	62
3.9 Interband transitions in a quantum regime	67
3.10 Summary	73
4 Magneto-optics of bulk Bi₂Se₃	77
4.1 The state of the art	77
4.2 Band structure from the BHZ-hamiltonian	78
4.3 Determination of the bandgap	81
4.4 Magneto-circular dichroism	86
4.5 Interband Faraday rotation	92
5 Conclusion	101
6 Perturbative approach for (112)-oriented Bodnar Hamiltonian	105
7 Selection rules	107
8 On formation of Dirac cones	109
9 Landau level structure in Bi₂Se₃	111

10 Publications and communication related to this work	115
Bibliography	116

Abstract (Eng)

The use of the Dirac/Weyl equation provides us a conceptual simplification in the description of various solid-state materials. Within recent years, such an approach appeared to be particularly successful for our understanding of electronic band structures of a number of materials. Typically, these systems are characteristic by conical bands, such as graphene, the surface states of topological insulators or recently discovered three-dimensional Dirac/Weyl semimetals. Surprisingly, for many materials with a well-defined electronic band gap such as bulk states of topological and topological crystalline insulators, the same description can be adopted as well. In all mentioned systems, a standard relativistic-like formula for E - k dispersion represents a continuous crossover from the linear to parabolic bands with an effective electron rest mass defining a bandgap. Such paradigm became a starting point for the explanations of various observed physical phenomena.

The primary experimental technique in the this work, infrared Fourier transform spectroscopy combined with a magnetic field, represents a powerful tool to probe and study an electronic structure and magneto-optical response in a wide range of energies. The method of infrared magneto-spectroscopy becomes in particular beneficial when utilized at the high-field installation of resistive coils in LNCMI-CNRS, Grenoble. Probing condensed-matter systems under such extreme conditions, often allows us to overcome their limited electronic quality (typical of all novel materials at the cutting edge of research) and to probe them in the quantum regime with well resolved Landau levels and often also in the quantum limit, with all electrons occupying the fundamental level.

In the first part, we introduce cadmium arsenide (Cd_3As_2). This material has recently reappeared in the condensed matter physics, thanks to theoretical predictions and subsequent experimental reports, as the first candidate of a 3D symmetry-protected Dirac semimetal stable under ambient conditions. In this work, however, we provide an alternative view, indicating a realization of a gapless Kane semimetal that is characteristic by an hourglass-like conical band structure that is further intersected at the nodal point by an extra flat band. Such a system is typically realized in zincblende structures close to the point of a semiconductor-semimetal transition at the crossover between the inverted and normal band ordering. The tetragonal distortion of the Kane model allows a formation of the tilted Dirac cones at the smaller scale as a consequence of the crossing between the conical and flat band.

A method how to qualitatively distinguish between the Dirac and Kane systems was elaborated. On the basis of the observed magneto-optical results, we found the nearly gapless Kane model to be a consistent explanation at the investigated energy scale contradicting thus the existence of the pure Dirac cones. A striking similarity between the band structure of cadmium arsenide and HgCdTe at the critical composition was found. Primarily, the magneto-reflectivity showed a cyclotron resonance mode with a characteristic \sqrt{B} -dependence in the high magnetic field and which was in addition independent of the initial Fermi level in the quantum limit of the system. Secondly, the

magneto-transmission revealed a set of interband Landau level resonances that could be interpreted only as a flat-to-cone type in order to preserve the consistency of the model. Besides, the linearity of the dynamic conductivity measured at zero field serves as a hallmark of the conical bands. The Dirac cones are proposed to coexist within the Kane model in the form of a substructure (at low energy scale) formulated using the Bodnar model based on the conventional eight-band k.p theory.

The second part of the thesis is dedicated to bismuth selenide (Bi_2Se_3) which often serves as an archetypal example of a 3D topological insulator. Though, its surface states are well defined and form a single 2D Dirac cone on the crystal facets, they are hardly experimentally accessible for optics and electronic transport since the optical response is in vast majority of cases determined by intra and interband excitations in bulk. From such a reason, we mainly focus on the bulk structure and study a peculiar condition fulfilled between the mass term, bandgap and velocity in the Bernevig, Hughes and Zhang Hamiltonian. The p-like character of the both conduction and valence bands with pronounced electron-hole symmetry brings intriguing relation between the Zeeman and cyclotron energy, the specific pinning between fancharts of Landau subsets or nearly equal Zeeman energy of electrons and holes.

The observation of a relatively strong photoluminescence signal from bulk Bi_2Se_3 suggests the existence of a direct band gap, in agreement with the earlier Landau level spectroscopy performed in high fields. This observation gives a new and controversial insight to the ARPES data, which in most cases conclude a camel-back-like profile of the valence band at the center of the Brillouin zone. The basic characterization from the transmission measurements at zero-field documents the presence of the Moss-Burstein shift, that effectively increases the optical gap, and which is directly connected to the cross section of the Fermi surface (frequency of the Shubnikov-de Haas oscillations) obtained from the magneto-transport. The intriguing magneto-optical response then may be understood in terms of Pauli paramagnetism, or in other words, as due to occupation effects of a degenerate electron gas in a parabolic band with a strong Zeeman splitting. Such behaviour is evinced in the transmission as a gradual splitting of the interband absorption edge with a successive saturation regime due to the partial/total spin polarization of electrons. The dichroism gives rise to a strong linear-in-B Faraday rotation which can be described by a simple model of the Verdet constant that depends only on the initial Fermi level, effective mass and bandgap. In higher fields, the Faraday rotation also follows the edge splitting until the quantum limit is reached, when the optical gap becomes determined by absorption into the lowest electron Landau level. Bismuth selenide can host various optical phenomena following the thickness of the explored sample. These phenomena may arise from the surface states and 2D quantum confinement in the case of thin films, over a bulk interband absorption with a fundamental edge and Landau level transitions for an intermediate thickness, up to the Faraday rotation or plasma edge optimized on hundreds- μm -thick slabs.

The manuscript is organised as follows

Chapter 1 - Introduction

We start with an analogy between the solid state physics and high energy physics to describe single-particle excitations using a relativistic approach of linear E - k dispersion. Then, the consequence of discrete symmetries on existence of the Weyl/Dirac points is discussed. The Kane gapless system, an alternative model for description of semimetals, is introduced in a connection with the Dirac formalism. The concept of topological matter and surface states is shown on simplified examples. The optical response is explained within the context of the Kubo-Greenwood formula. The Landau level energy structure, emergent upon a presence of the magnetic field, is compared for the three different systems - parabolic vs. linear Dirac/Kane bands respectively.

Chapter 2 - Experimental

Infrared Fourier transform spectroscopy, coupled to an external magnetic field and performed at liquid He temperature, serves as a main experimental technique in this study and it is schematically presented in the configuration of transmission, reflectivity and photoluminescence. The magnetic field is essential for driving the system into a quantum phase with discrete Landau levels and allows to observe related electronic excitations. The stationary field is generated either using a superconductive coil or by a resistive magnet (up to 35 T). The electronic transport is used as a complementary method for optical measurements.

Chapter 3 - Magneto-optics of Cd_3As_2

In this chapter, we focus on cadmium arsenide and we try to resolve the type and size of conical bands recently proposed for this material. We revise the Bodnar model elaborated in the literature. Then, the experimental part follows starting with a basic optical characterization of various samples carried out at zero-field. The magneto-optical response in a classical regime was investigated at low magnetic fields and supported by transport measurements revealing Shubnikov-de Haas oscillations. A significant contradiction with the Dirac model is found. The decisive arguments about the realization of the Kane model in the studied system is obtained from the cyclotron resonance measured in high magnetic fields. Additionally, a series of inter-Landau level transitions from the flat to the conical band was observed in the transmission. In summary, we propose a scenario for the band structure in which the Dirac and Kane cones are feasible to coexist on two distinct energy scales.

Chapter 4 - Magneto-optics of Bi_2Se_3

This chapter is dedicated to the magneto-optical response of bulk Bi_2Se_3 . In the beginning, the state-of-art knowledge about the band structure is reviewed and a simple BHZ-theory is introduced. A widely disputed bandgap was determined by comparing the results from photoluminescence, transport and transmission. Then a splitting of

an absorption edge in the magnetic field was found and an associated strong magneto-circular dichroism was investigated. Such behaviour gives rise to a peculiar Faraday rotation which experiences a linear regime followed by saturation.

Chapter 5 - Conclusion & Appendices

In conclusion, the main findings are summarized in a connection to the important questions related to the Dirac and topological matter. In the first appendix, a situation of the specific experimental geometry is discussed for Cd_3As_2 , when the magnetic field is not oriented in parallel with axes of the coordination system. In the second appendix, we comment in detail on the extrapolation procedure that was used for the estimation of the bandgap in Cd_3As_2 . The third annex addresses the selection rules of optical transitions and compares their intensities in both studied systems. The fourth supplement develops an idea of the realization of a quasi-Dirac structure in epitaxial layers of zincblende-like compounds using a mechanical strain. In the last appendix, we provide a brief review of the Landau level structure for Bi_2Se_3 as it is derived from the BHZ-theory to extend a theoretical background beyond the classical response.

Resumé (Fr)

L'équation de Dirac/Weyl fournit une description simplifiée des propriétés électroniques de divers matériaux. Cette approche a fait ses preuves en décrivant efficacement la structure des bandes électroniques coniques de certains systèmes récemment découverts tels que le graphène, les états de surface des isolants topologiques et les semi-métaux de Dirac et de Weyl. Cette méthode peut être étonnamment appliquée pour plusieurs autres systèmes avec un gap électronique distinct, tels que les états localisés dans le volume des isolants topologiques ou encore les isolants topologiques cristallins. Pour tous ces systèmes, la forme relativiste de la formule décrivant la relation de dispersion permet de décrire la frontière entre le régime linéaire et le régime parabolique avec l'aide d'une masse effective de l'électron au repos. Ce paradigme est devenu la pierre angulaire pour la description de nombreux phénomènes physiques observés.

La principale technique expérimentale utilisée dans ce travail, soit la spectroscopie infrarouge à transformée de Fourier sous champ magnétique, est un outil puissant pour sonder et étudier la structure électronique ainsi que la réponse magnéto-optique pour une large plage d'énergies. Celle-ci est particulièrement utile avec les bobines résistives à fort champ magnétique situé au LNCMI-CNRS à Grenoble. Sonder des systèmes physiques sous forts champs permet souvent de s'affranchir des problèmes liés à la qualité des échantillons (problèmes fréquents dans tous nouveaux matériaux à la fine pointe de la recherche) en permettant de les sonder dans le régime quantique où les niveaux de Landau sont bien résolus et parfois dans la limite quantique, où tous les électrons occupent le niveau fondamental.

Dans la première partie, nous introduisons l'arséniure de cadmium (Cd_3As_2). Les propriétés électroniques de ce matériau ont été récemment redécouvertes grâce aux prédictions théoriques combinées à des travaux expérimentaux. Leurs conclusions décrivent ce composé comme un semi-métal de Dirac protégé par symétrie qui reste stable à température et pression ambiante. Ce travail propose une interprétation alternative et originale expliquant les propriétés de ce composé. L'arséniure de cadmium serait un semi-métal de Kane sans gap caractérisé par la présence de bande électronique conique en forme d'un sablier croisé au point nodal par une bande additionnelle plate. Ce type de système est retrouvé dans la structure de zincblende proche du point de transition entre l'état semiconducteur et l'état semi-métal, soit à la frontière où les bandes se croisent pour s'inverser.

Une méthode de distinction qualitative entre les systèmes Dirac et Kane a été élaborée. Sur la base des résultats magnéto-optiques observés, nous concluons que le modèle de Kane presque irrégulier est une explication cohérente pour l'échelle d'énergie étudiée, contredisant ainsi l'existence des cônes de Dirac purs. Une similarité frappante entre la structure de bande de l'arséniure de cadmium et celle du HgCdTe à la composition critique a été trouvée. Premièrement, la magnéto-réflexivité montre un mode de résonance cyclotron avec une dépendance caractéristique \sqrt{B} sous champ magnétique élevé qui est indépendante du niveau de Fermi initial dans la limite quantique du système. Deuxièmement, la magnéto-transmission révèle un ensemble de résonances

des transitions de niveaux de Landau qui ne peuvent être interprétés que comme le croisement d'une bande conique avec une bande plate afin de préserver la cohérence du modèle. En outre, la linéarité de la conductivité dynamique mesurée à champ nul est une caractéristique des bandes coniques. Les cônes de Dirac sont proposés pour coexister dans le modèle de Kane sous la forme d'une sous-structure décrite à l'aide du modèle Bodnar basé sur la théorie conventionnelle de $k \cdot p$ de huit bandes.

La deuxième partie de la thèse est consacrée au sélénure de bismuth (Bi_2Se_3) qui est l'exemple d'un isolant topologique en 3D. Malgré que ses états de surface sont distincts et qu'ils forment un seul cône Dirac 2D sur la surface cristalline, ceux-ci ne sont presque pas visibles par les mesures optiques et les mesures de transport électronique, puisque la réponse optique est généralement déterminée par des excitations intra et interbandes dans le volume du cristal. Ainsi, nous nous concentrons principalement sur le cristal massif et étudions un cas particulier du terme de masse, du gap et de la vitesse dans l'Hamiltonien de Bernevig, Hughes et Zhang. Le caractère typique des orbitales p des deux bandes de conduction et de valence combiné à une symétrie électron-trou crée une relation intrigante entre l'énergie de Zeeman et l'énergie cyclotronique, une disposition particulière des niveaux de Landau ou une énergie de Zeeman équivalente entre les électrons et les trous.

L'observation d'une photoluminescence relativement intense provenant du volume Bi_2Se_3 suggère l'existence d'un gap électronique directe, en accord avec la spectroscopie des niveaux de Landau effectuée antérieurement sous champs élevés. Cette observation donne un aperçu à la fois original et contradictoire des mesures ARPES, qui, dans la plupart des cas, observent une bande de valence ayant le profil d'un dos de chameau au centre de la zone de Brillouin. La caractérisation à partir des mesures de transmission sous champ nul permet l'observation d'un décalage Moss-Burstein, qui augmente efficacement l'écart optique et qui est directement relié à la section transversale de la surface de Fermi (fréquence des oscillations Shubnikov-de Haas observées avec les mesures de magnéto-transport). La réponse magnéto-optique peut alors être expliquée par du paramagnétisme de Pauli, ou en d'autres termes, par des effets d'occupation d'un gaz d'électrons dégénéré dans une bande parabolique avec une forte division de Zeeman. Un tel comportement se manifeste dans la transmission par un fractionnement progressif du seuil d'absorption interbande avec des points de saturation successifs causé par la polarisation partielle/totale des spins des électrons. Le dichroïsme donne lieu à une forte rotation de Faraday linéaire, en fonction du champ magnétique appliqué, qui peut être décrit par un modèle simple de la constante de Verdet dépendant uniquement du niveau de Fermi, de la masse effective et du gap. Dans les champs supérieurs, la rotation de Faraday suit également le fractionnement du seuil jusqu'à ce que la limite quantique est atteinte, soit lorsque l'écart optique est déterminé par l'absorption du niveau de Landau le plus bas. Le sélénure de bismuth peut héberger divers phénomènes optiques dépendant de l'épaisseur de l'échantillon exploré. Ces phénomènes peuvent résulter des états de surface et du confinement quantique 2D dans le cas de films minces. Ils peuvent également résulter de l'absorption interbande du cristal massif avec un seuil d'absorption fondamental et des transitions de niveaux Landau pour une épaisseur intermédiaire. Finalement, on retrouve la rotation de Faraday et un plasma de

bord optimisé sur les échantillons plus volumineux (quelques centaines de dalles μm d'épaisseurs).

Le manuscrit est organisé comme suit

Chapitre 1 – Introduction

Nous commençons par une analogie entre la physique de l'état solide et la physique des hautes énergies pour décrire les excitations à une seule particule en utilisant une approche relativiste de la dispersion linéaire $E-k$. Ensuite, on discute de l'effet de symétries discrètes sur l'existence des points de Weyl/Dirac. Le système Kane sans gap, un modèle alternatif décrivant les semi-métaux, est introduit en lien avec le formalisme de Dirac. Le concept de matière topologique et les états de surface sont présentés avec des exemples simplifiés. La réponse optique est expliquée dans le contexte de la formule de Kubo-Greenwood. La structure de niveau de Landau est comparée pour les trois systèmes différents, soient les bandes paraboliques, les bandes de Dirac linéaires et les bandes de Kane.

Chapitre 2 – Expérimental

La spectroscopie infrarouge à transformée de Fourier sous champs magnétiques externes et à température de l'hélium liquide est la principale méthode expérimentale utilisée dans ce travail. Celle-ci est schématisée dans trois différentes configurations possibles, soit la configuration en transmission, en réflexion et en photoluminescence. Le champ magnétique est essentiel pour conduire le système dans une phase quantique avec des niveaux discrets de Landau permettant ainsi d'observer leurs excitations électroniques associées. Le champ stationnaire est généré par une bobine supraconductrice ou par une bobine résistive (jusqu'à 35 T). Le transport électronique est utilisé comme méthode complémentaire pour les mesures optiques.

Chapitre 3 - Magnéto-optique de Cd_3As_2

Dans cette section, nous nous concentrons sur l'arséniure de cadmium et nous essayons de déterminer le type et la taille des bandes coniques récemment proposées pour ce matériau. Nous révisons le modèle Bodnar décrit dans la littérature. Ensuite, la partie expérimentale commence par une caractérisation optique de divers échantillons effectués sous champ nul. La réponse magnéto-optique dans un régime classique a été étudiée sous faibles champs magnétiques, étude soutenue par des mesures de transport révélant les oscillations de Shubnikov-de Haas. On y retrouve une contradiction importante avec le modèle Dirac. La résonance cyclotron mesurée sous champs magnétiques élevés apporte des arguments décisifs sur la validité du modèle de Kane. En outre, une série de transitions de niveaux de Landau de la bande plate à la bande conique a été observée dans la configuration en transmission. En résumé, nous proposons un scénario pour la structure de bande dans laquelle les cônes de Dirac et Kane peuvent coexister sur deux échelles d'énergie distinctes.

Chapitre 4 - Magnéto-optique de Bi_2Se_3

Ce chapitre est consacré à la réponse magnéto-optique du volume Bi_2Se_3 . Au début, l'état de l'art sur la structure de la bande est revu et une simple théorie BHZ est introduite. Un gap dont l'existence, largement contestée en communauté, a été déterminé en comparant les mesures de photoluminescence, du transport et de la transmission. Ensuite, un fractionnement d'un seuil d'absorption dans le champ magnétique a été trouvé ainsi qu'un dichroïsme fortement magnéto-circulaire associé. Un tel comportement donne lieu à une rotation de Faraday qui subit un régime linéaire suivi d'une saturation.

Chapitre 5 - Conclusion & Appendices

En conclusion, les principaux résultats sont résumés en lien avec les questions importantes liées aux cônes de Dirac et à la topologie des bandes. Dans la première annexe, une situation expérimentale spécifique est discutée dans le cas du Cd_3As_2 , lorsque le champ magnétique n'est pas orienté en parallèle avec les axes cristallins. Dans la deuxième annexe, nous commentons en détail la procédure d'extrapolation qui a été utilisée pour l'estimation du gap dans le Cd_3As_2 . La troisième annexe traite des règles de sélection des transitions optiques et compare leurs intensités dans les deux systèmes étudiés. Le quatrième supplément développe une idée de la réalisation d'une structure quasi-Dirac dans des couches épitaxiales de composés de structure zincblende utilisant une souche mécanique. Dans la dernière annexe, nous revisons brièvement la structure des niveaux de Landau dans le Bi_2Se_3 dérivée avec la théorie BHZ pour obtenir une théorie valide au-delà de la réponse classique.



1. Introduction

1.1 Preface

In the last decade, the scientific attention has been drawn towards an intensive search for a linear E - k dispersion hosted in emerging materials. In this context graphene represents a 2D archetypal system that exhibits the conical (hourglass resembling) structure with a Dirac point that coincides with the position of the intrinsic Fermi level. It turned out that other 2D allotropes as silicene, germanene, bismuthene, phosphorene show also a semimetallic character at the K-point valleys due to the specific hexagonal lattice [1, 2].

In many cases, a low-energy expansion of complex Schrödinger Hamiltonians results in simplified Hamiltonians identical or closely resembling those used in relativistic quantum electrodynamics, implying thus the well-known relativistic-like energy dispersion $E^2 = m_0^2 c^4 + p^2 c^2$ that reduces for a large momentum p and small mass m_0 to the linear expression $E = pc$ [3, 4]. For instance, such a situation occurs in rocksalt semiconductors with the bandgap approaching to zero, when the parabolic conduction and valence bands meet and reshape into cones as was observed in the ternary compound $\text{Pb}_x\text{Sn}_{1-x}\text{Se}$ for the critical composition [5].

Those systems imply intriguing properties such as a square-root dispersion of the Landau levels in the magnetic field, a dynamical conductivity increasing linearly with the photon energy or a Klein tunnelling that could be harnessed as key elements for several applications in sensing, photovoltaics, THz emission or Landau lasing.

Topological insulators represents an interesting class of materials with an inverted insulating phase in the bulk that gives rise to metallic surface states residing on the crystal facets that cross within the bandgap and which could be naively viewed as graphene sheets surrounding faces of the insulating crystal [6].

1.2 Origin of relativistic particles

The Dirac equation was derived to describe a behaviour of the relativistic particles with $\frac{1}{2}$ -spin

$$i\hbar \partial_t \psi = (c\mathbf{\Gamma}\cdot\mathbf{p} + \Gamma_4 m_0 c^2) \psi, \quad (1.1)$$

where c denotes the speed of light, m_0 is a rest mass of the particle and $\mathbf{\Gamma} = (\Gamma_1, \Gamma_2, \Gamma_3)$, Γ_4 are the Dirac matrices written in the standard representation [7] as

$$\Gamma_1 = \begin{pmatrix} \sigma_x & 0 \\ 0 & -\sigma_x \end{pmatrix}, \Gamma_2 = \begin{pmatrix} \sigma_y & 0 \\ 0 & -\sigma_y \end{pmatrix}, \Gamma_3 = \begin{pmatrix} \sigma_z & 0 \\ 0 & -\sigma_z \end{pmatrix}, \Gamma_4 = \begin{pmatrix} 0 & \mathbb{I} \\ \mathbb{I} & 0 \end{pmatrix} \quad (1.2)$$

that satisfies the anticommutator algebra

$$\{\Gamma_i, \Gamma_j\} = 2\delta_{ij}, \{\Gamma_i, \Gamma_4\} = 0, \Gamma_i^2 = \Gamma_4^2 = \mathbb{I}$$

for $i, j = 1..4$ with $\sigma_x, \sigma_y, \sigma_z$ being Pauli matrices. The wavefunction has four components and it can be expressed as a double bispinor $\psi = (\psi_R, \psi_L)^\top$ with more explicit forms in two equations

$$\begin{aligned} (i\hbar \partial_t - c\boldsymbol{\sigma}\cdot\mathbf{p})\psi_R &= m_0 c^2 \psi_L, \\ (i\hbar \partial_t + c\boldsymbol{\sigma}\cdot\mathbf{p})\psi_L &= m_0 c^2 \psi_R. \end{aligned} \quad (1.3)$$

The associated eigenenergies are doubly degenerate with respect to the spin

$$E_{\pm} = \pm \sqrt{p^2 c^2 + m_0^2 c^4}. \quad (1.4)$$

The negative energy solution could be interpreted as an antiparticle state in the Dirac sea awaiting for recombination over an energy gap of $2m_0 c^2$ with a real particle. Each bispinor belongs to the two-dimensional spin subspace generated by the basis vectors for spin up and down $\uparrow = (1, 0)^\top$, $\downarrow = (0, 1)^\top$. The expansion of the energy dispersion (1.4) with respect to the kinetic energy provides either a classical Schödinger expression or purely massless form

$$E(k) = \begin{cases} \pm \frac{p^2}{2m_0} \pm m_0 c^2 & \text{for } \frac{p}{m_0} \ll c \\ \pm pc & \text{for } m_0 = 0. \end{cases}$$

In this context, we can further define an operator of the spin as

$$\mathbf{S} = \frac{\hbar}{2} \begin{pmatrix} \boldsymbol{\sigma} & 0 \\ 0 & \boldsymbol{\sigma} \end{pmatrix}, \quad (1.5)$$

and a helicity as a projection of the spin to the direction of motion $h = \frac{2\mathbf{S}\cdot\mathbf{p}}{|\mathbf{p}|}$. In the limit of the zero rest mass, the equations (1.3) are no longer coupled

$$i\hbar \partial_t \psi_{R,L} = \pm c \boldsymbol{\sigma}\cdot\mathbf{p} \psi_{R,L} \quad (1.6)$$

and they are referred as the Weyl equations that describes purely massless $\frac{1}{2}$ -spin particles.

The last equations can be mapped to the certain situations realized in the condensed matter, however the overall context of the band structure at the larger scale needs to be respected. Such a specific description is beneficial for the characterization of the low energy excitations close to the point-contact of the two linear bands. Then the obtained charge neutrality point, that obeys one of the equations (1.6), is called a Weyl node. The velocity c is a positive parameter and the sign before determines the node's chirality $\chi = \pm 1$.

1.3 Consequence of discrete symmetries

The specific properties of Dirac/Weyl electrons closely reflect symmetries present in a given material. Firstly, let us introduce a time reversal operation $\mathcal{T} : x, t \mapsto x, -t$ that reverses the direction of the timeline and thus particle's motion too. The time reversal may be represented by an anti-unitary operator $\mathcal{T} = -i\sigma_y K$, which acts equally on $\psi_{R,L}$ and where K denotes the charge conjugation¹. Its main consequence is the Kramers theorem saying that in a system with a half-integer total spin (whenever the time reversal symmetry is fulfilled, i.e. in the absence of the external magnetic field) there needs to exist a partner eigenstate for any Bloch state, which has the same energy. This means that the initial k -dependent Hamiltonian $H_{\mathbf{k}}$ and its transformed version $H_{-\mathbf{k}} = \mathcal{T}H_{\mathbf{k}}\mathcal{T}^{-1}$ have equal eigenvalues $E_{\mathbf{k},\uparrow} = E_{-\mathbf{k},\downarrow}$ but their eigenstates remain orthogonal $\psi = e^{i\mathbf{k}\mathbf{r}}(u_{\mathbf{k}\uparrow}(\mathbf{r}), u_{\mathbf{k}\downarrow}(\mathbf{r}))^T$, $\mathcal{T}\psi = \psi_{-\mathbf{k}}(\mathbf{r}) = e^{-i\mathbf{k}\mathbf{r}}(-u_{\mathbf{k}\downarrow}^*(\mathbf{r}), u_{\mathbf{k}\uparrow}^*(\mathbf{r}))^T$. An analogical statement holds for a system with an inversion symmetry defined as $\mathcal{P} : x, t \mapsto -x, t$ inverting spatial coordinates. Then, the Hamiltonians $H_{\mathbf{k}}$ and $H_{-\mathbf{k}} = \mathcal{P}H_{\mathbf{k}}\mathcal{P}^{-1}$ imply a degeneracy of energies $E_{\mathbf{k},\uparrow} = E_{-\mathbf{k},\uparrow}$ with conserving the orthogonality between the states ψ and $\mathcal{P}\psi = \psi_{-\mathbf{k}}(\mathbf{r}) = e^{-i\mathbf{k}\mathbf{r}}(u_{\mathbf{k}\uparrow}(-\mathbf{r}), u_{\mathbf{k}\downarrow}(-\mathbf{r}))^T$.

It entails that for a given energy, whenever both symmetries \mathcal{T} and \mathcal{P} are satisfied, either a gap between a pair of bands is opened or the bands need to be four-fold degenerate, in the form of the double crossing at \mathbf{k} and $-\mathbf{k}$ or as a single pointlike intersection at $\mathbf{k} = 0$. The tendency for a gap opening depends on a specific form of the Hamiltonian and dimensionality of the system [8]. It can be shown that the total chirality (sum of chiralities of all Weyl points) in the entire Brillouin zone must be zero due to the translational invariance and therefore Weyl nodes always arise in pairs of the opposite handedness [9]. In a system with the simultaneous \mathcal{T} , \mathcal{P} symmetries, the two Weyl points must overlap in the k -space resulting in either gap opening through their annihilation, or in a creation of a single Dirac point (DP), where the Weyl nodes coincide one onto the each other [8, 10]. Thus, in order to have isolated Weyl nodes, the time reversal symmetry or the inversion needs to be broken. Each symmetry breaking separates the Weyl points (WP) in a different way. For the broken time reversal symmetry, e.g. realized by the presence of an external magnetic field or by adding a magnetic impurity, WPs are displaced in the momentum space at points \mathbf{K}_W and $-\mathbf{K}_W$ [11]. On

¹In genuine $\frac{1}{2}$ -spin systems

the other hand, when the inversion symmetry is violated (e.g. in non-centrosymmetric point groups), WPs get mutually shifted in the energy axis by a term χQ_0 . The both cases can be formally expressed as [12]

$$H_{W,\chi} = \chi \hbar v \boldsymbol{\sigma} \cdot (\mathbf{k} - \chi \mathbf{K}_W) + \chi Q_0 \mathbb{I}, \quad (1.7)$$

where the velocity parameter v substitutes the speed of light c in real systems. As examples of Weyl semimetals serve TaAs or NbAs with the broken inversion or YbMnBi₂ lacking the time reversal symmetry [13].

The presence of a rotational axis in a crystallographic point group may have analogous consequence as the two former types of symmetries [14]. Here, a rotational operator of an n -fold axis $\mathcal{C}_n : x, t \mapsto R_n^{-1}x, t$ with 3×3 rotational matrix R_n needs to obey $H_{(R_n \mathbf{k})} = \mathcal{C}_n H_{\mathbf{k}} \mathcal{C}_n^{-1}$ and thus brings about a degeneracy of n equivalent sites in the Brillouin zone (BZ). Secondly, it can be proven on the basis of deeper considerations that a symmetry-protected Dirac point is forbidden to take place at the Γ -point in three dimensions [15]. But, if the Dirac points are located on the rotational axis, they become protected by this extra symmetry, which turned out to be advantageous for the systems with the time reversal but lacking the inversion [15]. For the case of the Weyl nodes, a small variations in the system can only move slightly WPs in the k -space but without the introducing of a gap. The only way that WPs could be destroyed is to introduce a perturbation strong enough to merge them together, inducing thus their mutual annihilation, or by breaking the conservation of chirality [16].

1.4 From a Dirac to the Kane model

It turns out that a two-dimensional system with the honeycomb lattice (e.g. graphene) can be viewed in terms of the Weyl physics as following. The Dirac cones located at valleys \mathbf{K} and $\mathbf{K}' = \chi \mathbf{K}$ give rise after the transform $\mathbf{k} \rightarrow \mathbf{k} - \chi \mathbf{K}$ to the different pseudochiralities in the sense of the equation (1.7). In the spinor notation (1.5), the operator $\boldsymbol{\sigma}$ retains the meaning of the pseudospin related to the individual triangular sublattice instead of the classical $\frac{1}{2}$ -spin. Let us assume a coordination system chosen in the way where the x -axis lies along the line $\overline{\mathbf{K}\mathbf{K}'}$, then the graphene Hamiltonian reads

$$H_{W,\chi}^{\frac{1}{2}} = \hbar v \begin{pmatrix} 0 & \chi k_x - i k_y \\ \chi k_x + i k_y & 0 \end{pmatrix} \quad (1.8)$$

giving a dispersion $E = \pm \hbar v |\mathbf{k}|$ and the corresponding wavefunctions

$$\psi = \frac{1}{\sqrt{2}} (1, \pm \chi e^{i\chi\theta})^T e^{i\mathbf{k}\mathbf{r}}, \quad (1.9)$$

where the sign is associated with the electrons or holes. The angle θ is measured between the momentum $\mathbf{k} = k(\cos \theta, \sin \theta, 0)^T$ and the x -axis. The mean value of the pseudospin $\langle \boldsymbol{\sigma} \rangle = \pm (\chi \cos \theta, \sin \theta)^T$ points in parallel to \mathbf{k} for the electrons or anti-parallel for holes (for $\chi = 1$).

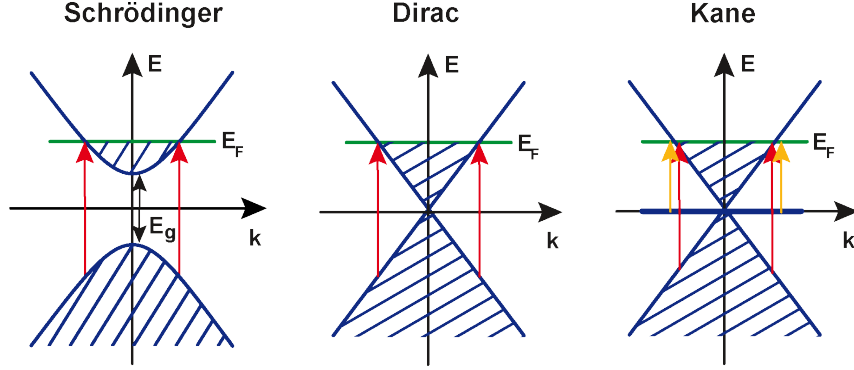


Figure 1.1: Three basic types of dispersions studied in this work. Schrödinger fermions are constrained in parabolic bands with classical kinetic energy $E = \frac{\hbar^2 k^2}{2m_0}$. The half-gap has a meaning of particle's rest mass $E_g/2 = m_0 v^2$, where the velocity v plays the role of the speed of light c . On contrary, the conical bands describe massless particles with the relativistic kinetic energy $E = v\hbar k$. The Kane model is particular to the case of the Dirac by the existence of an additional flat band that intersects the apex. The onset of the interband optical transitions is affected by the position of the Fermi level (since Pauli-blocked transitions can not be realized) by a factor (so called Moss-Burstein shift) which for the case of symmetric parabolic bands becomes $2E_F$. Thus, the onset begins at $E_g + 2E_F$, versus E_g for a purely intrinsic case.

When the honeycomb lattice is upgraded with an extra triangular sublattice with the points residing in centers of the old hexagons, a new lattice pattern is formed with the motif of a dice lattice [17, 18]. The addition of an extra atom to the each primitive cell gives rise to a flat band intersecting the Dirac point and thus producing a singularity in the density of states with a large impact on the various physical features [17]. The Hamiltonian expressed in the basis - top cone, flat band, bottom cone has a simple form [19]

$$H_{W,\chi}^1 = \frac{\hbar v}{\sqrt{2}} \begin{pmatrix} 0 & k_- & 0 \\ k_+ & 0 & k_- \\ 0 & k_+ & 0 \end{pmatrix} \quad (1.10)$$

that can be constructed using the orbital angular momentum matrices L_x, L_y for 1-pseudospin as $v(p_x L_x + p_y L_y)$ and characterized in the terms of the tri-spinor wavefunctions. Momenta k_+, k_- are defined as $k_+ = k_x + ik_y, k_- = k_x - ik_y$.

The fusion of the honeycomb and dice lattices gives rise to a general model α -T₃ [20, 21] that continuously interpolates the transition between the both boundary situations via a parameter α as follows

$$H_{W,\chi}^\alpha = \frac{\sqrt{2}\alpha}{\sqrt{1+\alpha^2}} H_{W,\chi}^1 + \frac{2(1-\alpha)}{\sqrt{1+\alpha^2}} H_{W,\chi}^{\frac{1}{2}} \oplus 0. \quad (1.11)$$

The genuine graphene is obtained for $\alpha = 0$, whilst the opposite choice with $\alpha = 1$ gives the dice lattice, since the value of the α -parameter expresses a relative hopping amplitude to the third sublattice lattice. So even for graphene, the third sublattice could be constructed and imagined as always present but not interacting with the others. Then, the obtained extra flat-band never interacts or mixes with the Dirac

cones and therefore its presence is not relevant for the actual band structure and can be disregarded in this case. The Hamiltonian for the opposite chirality (or K' -point) is obtained via a simple unitary transform [18] and the whole problem could be formulated in a block-diagonal form as $H_W^\alpha = H_{W,+ \chi}^\alpha \oplus H_{W,- \chi}^\alpha$.

More interestingly, a zinc-blende structure of semiconductors under certain circumstances may resemble a specific case of α -T₃ model (1.11) for $\alpha = \frac{1}{\sqrt{3}}$ from the simple reasons [22]. Firstly, the projection of zinc-blendes in the direction $\frac{1}{\sqrt{3}}(1, 1, 1)^\top$ coincides with the dice lattice [23]. Secondly, the effective hybridization of orbital basis $(s, u_x, u_y, u_z) \otimes (\uparrow, \downarrow)$ in zinc-blende structures results in the same spin-space as for the α -T₃ model that includes both pseudo-chiralities. In a conventional eight-band approximation, the s-state $\mathbf{L}_0 \otimes \mathbf{S}_{\frac{1}{2}}$ decouples from the mixed p-states $\mathbf{L}_1 \otimes \mathbf{S}_{\frac{1}{2}}$ and the LS-basis is formed as

$$(s \uparrow, u_{-1} \uparrow, u_0 \uparrow, u_{+1} \uparrow, s \downarrow, u_{-1} \downarrow, u_0 \downarrow, u_{+1} \downarrow), \quad (1.12)$$

with u_n functions built for $L = 1$ as

$$u_{-1} = \frac{i}{\sqrt{2}}(u_x - iu_y), \quad u_0 = iu_z, \quad u_1 = \frac{-i}{\sqrt{2}}(u_x + iu_y). \quad (1.13)$$

By introducing the total angular momentum $\mathbf{J} = \mathbf{L} + \mathbf{S}$, the p-states are rearranged into JM-basis for $J = \frac{3}{2}, \frac{1}{2}$ as

$$\begin{aligned} E^\uparrow \quad s_{\frac{1}{2}, +\frac{1}{2}} &= is \uparrow \\ HH^\uparrow \quad u_{\frac{3}{2}, +\frac{3}{2}} &= u_{+1} \uparrow \\ LH^\uparrow \quad u_{\frac{3}{2}, -\frac{1}{2}} &= \sqrt{\frac{2}{3}}u_0 \uparrow + \sqrt{\frac{1}{3}}u_{+1} \downarrow \\ SH^\uparrow \quad u_{\frac{1}{2}, +\frac{1}{2}} &= \sqrt{\frac{1}{3}}u_0 \uparrow - \sqrt{\frac{2}{3}}u_{+1} \downarrow \\ E^\downarrow \quad s_{\frac{1}{2}, -\frac{1}{2}} &= is \downarrow \\ HH^\downarrow \quad u_{\frac{3}{2}, -\frac{3}{2}} &= u_{-1} \downarrow \\ LH^\downarrow \quad u_{\frac{3}{2}, +\frac{1}{2}} &= \sqrt{\frac{2}{3}}u_0 \downarrow + \sqrt{\frac{1}{3}}u_{-1} \uparrow \\ SH^\downarrow \quad u_{\frac{1}{2}, -\frac{1}{2}} &= -\sqrt{\frac{1}{3}}u_0 \downarrow + \sqrt{\frac{2}{3}}u_{-1} \uparrow \end{aligned} \quad (1.14)$$

that is associated with the notation E, HH, LH, SH classifying the bands as the electron, light hole, heavy hole and the spin-split hole band. As it is common for the semiconductors with the strong spin-orbit coupling (SOC), the spin-split hole band is shifted downwards in energy by a factor Δ and plays a minor role, while the electron band is interpreted as the top band, the heavy hole band as the flat band and the light hole band as the bottom band in the convention of the (normally-ordered) α -T₃ model.

The conventional Kane model utilized for the description of the band structure of zincblende semiconductors in the six-band approximation (i.e. omitting the spin-split hole band) is constructed in JM-basis at Γ -point as following

$$H_K = \begin{pmatrix} H_{W,\uparrow}^{\frac{1}{\sqrt{3}}} & \hbar v k_z C \\ \hbar v k_z C^\top & H_{W,\downarrow}^{\frac{1}{\sqrt{3}}} \end{pmatrix} \quad (1.15)$$

where the matrices have the explicit forms

$$H_{W,\uparrow}^{\frac{1}{\sqrt{3}}} = \gamma \begin{pmatrix} 0 & \sqrt{3}k_- & 0 \\ \sqrt{3}k_+ & \bar{E}_g & -k_- \\ 0 & -k_+ & 0 \end{pmatrix}, H_{W,\downarrow}^{\frac{1}{\sqrt{3}}} = \gamma \begin{pmatrix} 0 & k_- & 0 \\ k_+ & \bar{E}_g & -\sqrt{3}k_- \\ 0 & -\sqrt{3}k_+ & 0 \end{pmatrix}, C = \begin{pmatrix} 0 & 0 & 0 \\ -1 & 0 & 0 \\ 0 & -1 & 0 \end{pmatrix} \quad (1.16)$$

with factor $\gamma = \hbar v/2$ and the chirality $\chi = \uparrow, \downarrow$ assigned to the pseudospin [22]. The matrix C describes the k -dependence in the z -direction and $\bar{E}_g = E_g/\gamma$ represents a renormalized gap between the top and bottom cone. When $k_z = 0$ is assumed, the matrices $H_{W,\uparrow}^{\frac{1}{\sqrt{3}}}$, $H_{W,\downarrow}^{\frac{1}{\sqrt{3}}}$ become decoupled. Then, for an intrinsic system with the Fermi level placed at the nodal point, the in-plane electron excitations are governed by one of those blocks in dependence on the spin. Such situation can be formally mapped to the case of the two pseudochiralities $\pm\chi$ occurring in the $\frac{1}{\sqrt{3}}$ -T₃ model.

The size of the gap determines whether a particle moves with a finite rest mass $m_0 = \frac{E_g/2}{v^2}$ in pseudo-parabolic bands or without any mass for strictly linear bands. The sign of the gap usually correlates with the mean atomic number of the semiconductor compound. The heavier elements the smaller direct gap (e.g. InAs, InSb) or the larger inverted (e.g. HgSe, HgTe) is found [24]. The strength of SOC follows a similar tendency. The HH band is degenerate with the LH bands at $\mathbf{k} = 0$. Consequently, the sign of a gap also affects whether the HH flat band is attached either to the top or bottom band as it can be deduced from the energy dispersion

$$E_{E,LH} = \frac{E_g}{2} \pm \sqrt{\frac{E_g^2}{4} + (\hbar vk)^2}, \quad E_{HH} = 0. \quad (1.17)$$

The basic band structures with parabolic (Schödinger) and linear (Dirac and Kane) dispersions, further studied in this text, are summarized in Fig. 1.1.

The gapless Kane system can be realized in zincblendes at the Γ -point by semiconductor-to-semimetal transition, e.g. in $\text{Hg}_x\text{Cd}_{1-x}\text{Te}$. Then, CdTe plays the role of a direct gap semiconductor with the normal band ordering E, HH, LH and HgTe is a semimetal with the inverted ordering LH, HH, E and negative bandgap separating E from LH/HH (Fig. 1.2). The size of the gap linearly interpolates between the two extremal cases with a possibility to reach the critical point for the composition, where $E_g = 0$, in order to form Kane cones with the flat band intersecting their apices. Then the Kane node is a result of an accidental degeneracy without any topological or symmetry protection and thus vulnerable to the gap opening easily by a small deviation in the composition or by temperature that affects the bandgap [4]. The electronic structure is described at low energies by the $\frac{1}{\sqrt{3}}$ -T₃ model for $k_z = 0$ [20] or more rigorously by the considering of the full eight-band k.p model [25, 26].

1.5 Topological insulators and their surface states

A topological insulator can be described in a simplified manner as an insulating phase with the inverted band ordering in the bulk and with semimetallic gapless edges at the

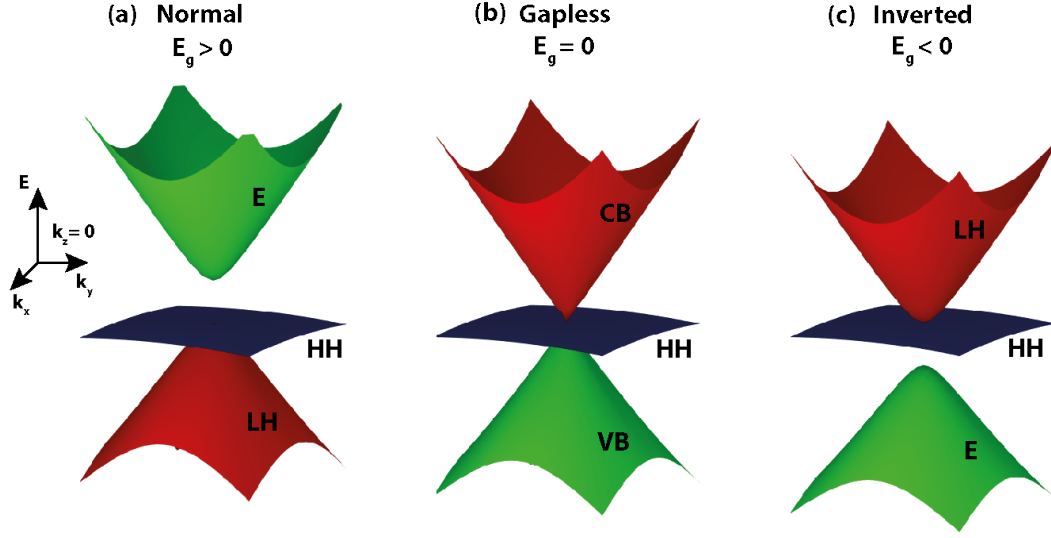


Figure 1.2: A continuous transition from a semiconductor (a) to the semimetal (c) is achieved for zincblende crystals at the Γ -point by reversing a positive E_g to the negative value. Then the s-type electron band E becomes inverted with the p-type light hole band LH. The heavy hole band HH is attached to LH due to the four-fold degeneracy at $k = 0$. A ternary compound $\text{Hg}_{1-x}\text{Cd}_x\text{Te}$ serves as an archetypal system for the realization, since the bandgap linearly interpolates as the composition x is smoothly varied between CdTe with the normal band ordering and $E_g = 1.6$ eV to inverted HgTe with $E_g = -0.3$ eV. The gap is closed when the critical concentration is finely tuned at low temperature to $x = 0.17$. Then, the electron and light-hole bands become purely conical and touch each other at a single point with the six-fold accidental degeneracy. This nodal point is not protected by any symmetry and any small perturbation can reopen the gap.

crystal surface. Those surface states (SS) exist due to an impossibility of the continuous interpolation between the bulk structure and vacuum without closing the gap since the both phases have non-equivalent topological classes (Fig. 1.3). In this context, the topology is characterized via an integer genus n_C of the closed manifold and represents an invariant property postulated by the Euler-Bonnet theorem

$$n_C = \frac{1}{2\pi} \int \mathcal{F}_m d^2\mathbf{k}. \quad (1.18)$$

When the curvature \mathcal{F}_m is integrated over the continuous surface of various shapes, the genus n_C is conserved and describes a number of holes in the manifold. Using the best known example, referring to the surface of simple geometrical objects, a sphere and torus are regarded as non-equivalent with $n_C = 0, 1$ that can not be mapped one-to-one using a single parametrization [27].

The topological band theory applies the same concepts to characterize periodic solid state systems and studies the correspondence between the k -space spanning the Brillouin zone and an associated Hilbert space of the Bloch functions $|u_m(\mathbf{k})\rangle$ with the mapping mediated by a Hamiltonian H_k . The curvature \mathcal{F}_m is constructed from the Berry connection $\mathcal{A}_m = i\langle u_m(\mathbf{k})|\nabla_{\mathbf{k}}|u_m(\mathbf{k})\rangle$ as a circulation $\mathcal{F}_m = \nabla_{\mathbf{k}} \times \mathcal{A}_m$. Then, the genus n_C is referred as the Chern number and has a meaning of the Berry phase that an electron acquires along a closed path in BZ.

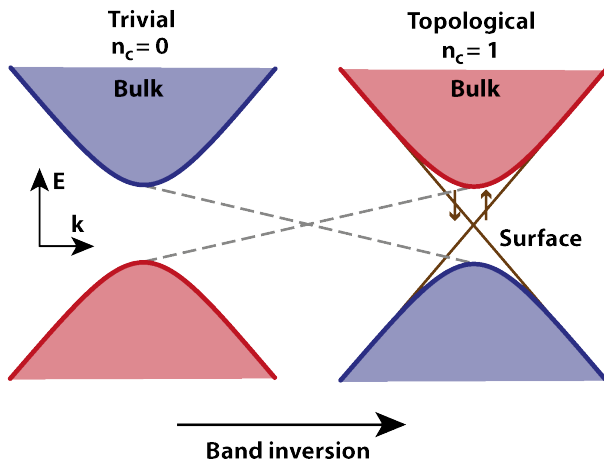


Figure 1.3: An illustration of two types of the insulator with different band orderings (trivial vs. topological) characterized by a Chern number. The inversion can be induced by a mass term (see Hamiltonian 1.19). A continuous transition between the both phases is not possible without a band crossing at the interface that gives rise to semimetallic chiral surface states.

The physical interpretation can be easily addressed in 2D with the use of the Haldane-Semenov Hamiltonian $H_{\text{HS}} = d_1(k)\sigma_x + d_2(k)\sigma_y + d_3(k)\sigma_z = \mathbf{d}(k) \cdot \boldsymbol{\sigma}$ that promotes new topological features through introducing an essential mass term $d_3(k) \neq 0$ to the simpler Dirac version (1.8) with $d_1(k) = k_x$, $d_2(k) = k_y$, $d_3(k) = 0$ [6, 7, 27]. With the construction of a unit vector $\hat{\mathbf{d}}(k) = \frac{\mathbf{d}}{|\mathbf{d}|} = (\cos \varphi_k \sin \theta_k, \sin \varphi_k \sin \theta_k, \cos \theta_k)^\top$ we can define a Bloch sphere for $|\mathbf{d}| \neq 0$ that allows to classify the solution of the eigenproblem H_{HS} with the energy $E_{\text{E,H}} = \pm |\mathbf{d}(k)|$ and wavefunctions $\psi_{\text{E}} = (\cos \frac{\theta_{\mathbf{k}}}{2} e^{i\varphi_{\mathbf{k}}}, \sin \frac{\theta_{\mathbf{k}}}{2})$ and $\psi_{\text{H}} = (\sin \frac{\theta_{\mathbf{k}}}{2} e^{-i\varphi_{\mathbf{k}}}, -\cos \frac{\theta_{\mathbf{k}}}{2})$ for the electron and hole bands E, H.

In graphene, the poles of the sphere $d_3(k = \pm \mathbf{K}) = 0$ are attributed to the Dirac points, whereas in the case of the Semenov and Haldane insulator with $d_3(k = \pm \mathbf{K}) = M_S$ and $d_3(k = \pm \mathbf{K}) = \chi M_H$, respectively, this depends on the valley index χ since $\mathbf{d} = (\chi k_x, k_y, d_3)$, see eq. (1.8). For the insulators the phase, accumulated at $\mathbf{k} = \pm \mathbf{K}$ by a winding around the same pole applying (1.18), relies on the sign of the mass and thus the partial Chern numbers either add or subtract as $n_C = \frac{1}{2} \pm \frac{1}{2}$. This means that the Semenov insulator is trivial, while the Haldane phase becomes topological.

The analogical fact holds in 3D for a Weyl semimetal with a Hamiltonian $H_{\text{W}}^{\frac{1}{2}} = \hbar v \boldsymbol{\sigma} \mathbf{k}$. The Berry curvature of the occupied band $\mathcal{F}_H = \chi v \frac{\mathbf{k}}{2|\mathbf{k}|}$, which penetrates through the surface enclosing multiple Weyl nodes, is anything but the sum of the inner chiralities. Thus each WP represents a monopole of the Berry curvature in the k -space. But the total flux through the entire BZ needs to be zero due to the periodicity of the Berry curvature $\mathcal{F}_m(\mathbf{k}) = \mathcal{F}_m(\mathbf{k} + \mathbf{G})$ with respect to the reciprocal lattice vector \mathbf{G} . So, WPs appear in pairs of the opposite chiralities.

When the two phases with different Chern numbers are put into a contact at $x = 0$ (e.g., Semenov and Haldane insulator, junction of semiconductors with the inverted and normal band ordering), the sign of the mass term is reversed between the both phases and nullified at the interface. From this reason, the dispersion of the edge states in the tangent direction to the surface is expected to be gapless, Dirac-like and with a defined direction of the spin. The wavefunction parallel to x -axis has a character of the mass domain wall called a Jackiw-Rebbi soliton. In 3D the interface is planar and the

Table 1.1: Examples of materials with distinct types of the band structure in dependence on the dimensionality (I-insulator, SM-semimetal, QW-quantum well).

	Trivial I	Topological I	Dirac SM	$\frac{1}{\sqrt{3}}$ -T ₃ /Kane SM	Weyl SM
2D	h-BN	HgTe QW [30]	Graphene [31]	?	?
3D	PbSe	Bi ₂ Se ₃ [32]	Pb _{0.77} Sn _{0.23} Se [5]	Hg _{0.17} Cd _{0.83} Te [25]	TaAs [13]

surface states in the k_x - k_y plane exhibit a spin texture locked with the momentum [28]. In addition, the surface states are also robust against perturbation due to the time-reversal symmetry.

For a 3D topological insulator, the spin nature needs to be taken into account and for a two-band model with the opposite parities the minimal 4×4 Hamiltonian after Bernevig, Hughes and Zhang [29] has a form $H_{\text{BHZ}} = \hbar v \mathbf{k} \cdot \mathbf{\Gamma} + (E_g + Mk^2)\Gamma_0$ with the use of the Dirac matrices Γ_i , or more explicitly expressed in the basis $H^\downarrow, E^\uparrow, H^\uparrow, E^\downarrow$

$$H_{\text{BHZ}} = \begin{pmatrix} \frac{E_g}{2} + Mk^2 & \hbar v k_+ & 0 & -\hbar v k_z \\ \hbar v k_- & -\frac{E_g}{2} - Mk^2 & \hbar v k_z & 0 \\ 0 & \hbar v k_z & \frac{E_g}{2} + Mk^2 & \hbar v k_- \\ -\hbar v k_z & 0 & \hbar v k_+ & -\frac{E_g}{2} - Mk^2 \end{pmatrix}. \quad (1.19)$$

The BHZ-hamiltonian in such a simplified form is essentially a 3D Dirac Hamiltonian with a gap E_g and mass term M added in order to induce the band inversion. The topological phase occurs, when M and E_g have different signs, and the trivial phase for the same signs respectively. Selected examples of topological materials are presented in Tab. 1.1.

1.6 Optical response

Optical spectroscopy is a traditional method in condensed-matter physics relevant for a number of single-particle or collective excitations in a broad range of materials, such as semiconductors, two-dimensional electron gases, oxides, magnetic compounds, strongly correlated metals, etc. [33]. Recently emerged topological systems, with their gapless or at most narrow-gap character, are a natural target of such (magneto-)optical investigations in the infrared and THz spectral ranges. Electronic band structures of many materials can be deduced with a relatively high precision/resolution using experiments in magnetic fields, in the quantum regime with well-resolved Landau levels. In a magnetic field, the classical free-carrier absorption is shifted to the finite energies and turns into a cyclotron resonance, from whose dispersion an effective mass can be extracted. Similarly, a direct interband absorption is modulated into the sharp interband inter-Landau level transitions, whose analysis resolves band parameters such as a bandgap or the interband coupling constants. In contrast to the nowadays popular and widely applied ARPES technique, it is also a suitable tool for probing of unoccupied state

(final state of an optical excitation) in a significantly higher energy resolution. On the other hand, the electronic transport concerns only the excitation in the proximity of the Fermi level.

The optical response, due to various excitations from the initial ψ_i to final states ψ_f , may be deduced from the following single-particle Hamiltonian with the classically introduced (not quantized) electromagnetic field

$$H_I = \frac{e}{m_0} \mathbf{p} \cdot \frac{\mathbf{E}_0}{2i\omega} (e e^{i\omega t} - \mathbf{e}^* e^{-i\omega t}), \quad (1.20)$$

where e is an electric charge of the particle, \mathbf{E}_0 denotes amplitude of the external electric field, ω is the frequency of incident light and \mathbf{e} signifies a unit vector of the polarization [34].

Both the interband and intraband components contribute to the total optical response represented by complex dynamical conductivity. In a classical picture the behaviour of the intraband transitions is characterized at low energies using the simple Drude term

$$\sigma_D(\omega) = \varepsilon_0 \omega_p^2 \frac{i\omega + \Gamma}{\omega^2 + \Gamma^2} \quad (1.21)$$

where $\Gamma = \hbar/\tau$ stands for the scattering rate (τ relaxation time) and the plasma frequency

$$\omega_p = \sqrt{\frac{N_e e^2}{\varepsilon_0 \varepsilon_r^\infty m_e}} \quad (1.22)$$

that forms a steep edge in the reflectivity below which all the light is reflected. The vacuum and the background permittivity are denoted as ε_0 , ε_r^∞ . The Drude-type term in most cases well describes (for non-correlated electrons) both dissipative (via its real part) as well as non-dissipative component (imaginary part) via processes implied by the presence of free charge carriers in the system with a density N_e and mass m_e . The quantitative description of interband processes usually requires a full quantum formalism. In the framework of the Kubo-Greenwood formula (linear response theory), the optical conductivity is given by

$$\begin{aligned} \sigma_{x_i x_j}(\omega) = \frac{\sigma_0}{\omega} \sum_{\alpha, \beta} \int \frac{d^3 \mathbf{k}}{(2\pi)^3} \langle \alpha \mathbf{k} | v_i | \beta \mathbf{k} \rangle \langle \beta \mathbf{k} | v_j | \alpha \mathbf{k} \rangle \times [f(E_\alpha(\mathbf{k})) - f(E_\beta(\mathbf{k}))] \\ \times \delta(\hbar\omega - (E_\beta(\mathbf{k}) - E_\alpha(\mathbf{k}))) \end{aligned} \quad (1.23)$$

which includes only process vertical in the k -space, i.e. those which conserve quasi-momentum of excited electrons ($k_\alpha = k_\beta$). Here, we assume a dipole transition between the initial state $|\alpha \mathbf{k}\rangle$ and the final state $|\beta \mathbf{k}\rangle$ with energies $E_\alpha(\mathbf{k})$, $E_\beta(\mathbf{k})$ in bands indexed as α , β . The conductivity is expressed in quantum units $\sigma_0 = \pi e^2 / \hbar^2$ and depends on three components - the square of the velocity matrix element $\langle \beta \mathbf{k} | v_i | \alpha \mathbf{k} \rangle$, the joint occupation ($f_\alpha - f_\beta$) with Fermi distribution f and the joint density of states given by a δ -function². The summation over the bands decides a number of the contributions

²The joint density of states is well defined quantity, only if the velocity matrix element does not

to the total response.

The interband transitions within the two different bands is a single photon absorption process, whose probability is proportional in the first order to the fine-structure constant α_0 and which depends crucially on the system's dimensionality via the joint density of states $D_j(E)$ and on the actual E - k dispersion as $\text{Re } \sigma(E) \propto D_j(E)/E$ [35] (Fig. 1.4). For example, in graphene an each sheet additively increases the absorption by a factor $\frac{\alpha_0}{\pi}$ that is constant in the energy due to the two-dimensional nature of the $D_j(E)$. In contrast, in a 3D Dirac system the optical conductivity becomes $\text{Re } \sigma_{xx}(\omega) = \frac{1}{12} \frac{c\varepsilon_0\alpha_0}{v} \omega$ [12, 25]. In a gapless Kane system, the conductivity reads $\text{Re } \sigma_{xx}(\omega) = \frac{13}{12} \frac{c\varepsilon_0\alpha_0}{v} \omega$ due to the presence of the flat band causing that flat-to-cone transitions dominate over cone-to-cone interband excitations (ratio 1:12), mostly due to the large difference in the joint density of states. In contrary, for parabolic bands the absorption scales as $\propto \frac{1}{x} \sqrt{x-1}$ with $x = \frac{E}{E_g}$.

The Fermi level E_F is another important parameter for the optical response. At low temperatures, it gives rise to so-called Pauli-blocking (in the context of conventional semiconductors often referred to as Burstein-Moss shift) which due to the carrier occupation suppresses otherwise optically active excitations (Fig. 1.1). The onset of the minimal excitation energy E_{\min} depends on the type of the dispersion and for the conical bands it is $2E_F$, E_F for the intercone or flat-to-cone transitions respectively, whereas for the symmetric parabolic bands separated by a gap, one obtains $E_g + 2E_F$.

1.7 The effect of the quantization in a magnetic field

In the classical picture/approach, any charge carrier undergoes a periodic (cyclotron) motion when a magnetic field is applied. When the field becomes strong enough to induce sizeable quantum effects, only some of cyclotron orbits (so called-Landau levels) become allowed.

To describe this quantization quantitatively, we introduce the magnetic field \mathbf{B} into the corresponding Hamiltonian via Peierls substitution $\mathbf{p} \rightarrow \boldsymbol{\pi} = \mathbf{p} - e\mathbf{A}$. Let us assume the magnetic field to point in the z -direction, then the perpendicular momentum operators obey the gauge-invariant commutation relations

$$[\pi_x, \pi_y] = -\frac{i\hbar^2}{l_B^2}, [\pi_x, \pi_z] = 0 \quad (1.24)$$

with a magnetic length $l_B = \sqrt{\hbar/eB}$, which allows to construct the ladder operators

$$a = \frac{l_B}{\sqrt{2\hbar}}(\pi_x - i\pi_y), \quad a^\dagger = \frac{l_B}{\sqrt{2\hbar}}(\pi_x + i\pi_y) \quad (1.25)$$

satisfying the standard commutator $[a, a^\dagger] = 1$. The problem can be treated with an algebra of the linear harmonic oscillator in a recurrent form

$$a^\dagger |n\rangle = \sqrt{n+1} |n+1\rangle, \quad a |n\rangle = \sqrt{n} |n-1\rangle \quad (1.26)$$

depend on momentum.

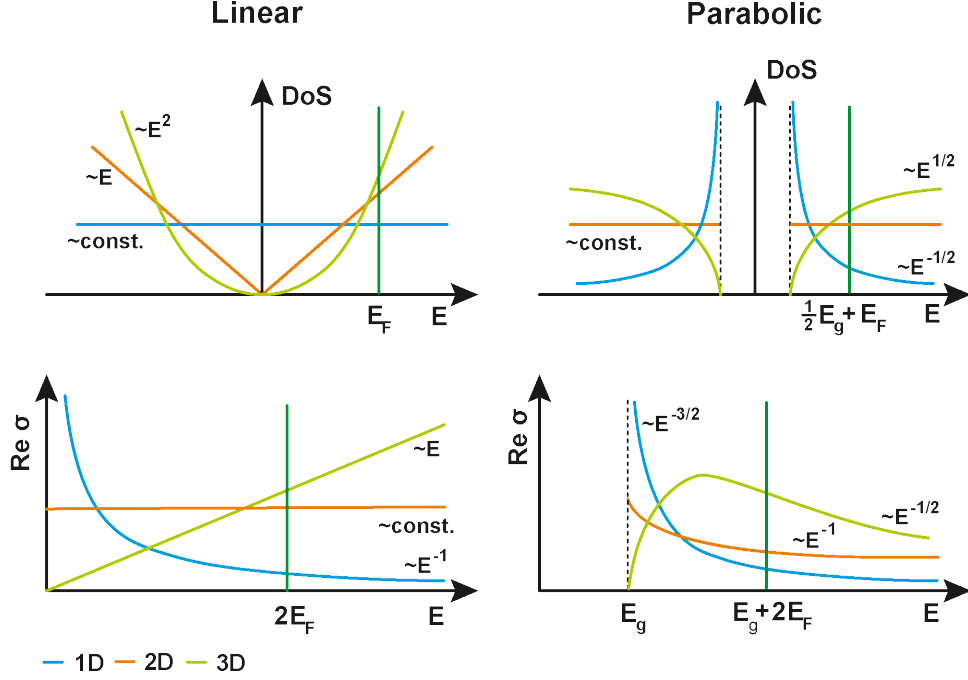


Figure 1.4: An illustration how a dimensionality affects the absorption of the system for a linear and parabolic shape of the bands. An additional dimension increases the capacity for electron population and thus enlarges the absorption weight, represented here as an optical conductivity, via incrementing the polynomial power in the energy. For a 3D system, the presence of the magnetic field decomposes the spatial dependence into the quantized 2D in-plane component and free 1D out-of-plane component.

or in an explicit form

$$a|0\rangle = 0, |n\rangle = \frac{(a^\dagger)^n}{\sqrt{n!}}|0\rangle, a^\dagger a|n\rangle = n|n\rangle. \quad (1.27)$$

In a case of the 3D electron gas with parabolic bands and well-defined effective electron mass m_e , this procedure is particularly easy due to a simple Hamiltonian

$$H_{3\text{DEG}} = \frac{1}{2m_e}(p_x^2 + p_y^2 + p_z^2). \quad (1.28)$$

After the quantization, one obtains

$$H_{3\text{DEG,B}} = \frac{\hbar}{m_e l_B^2} \left(a^\dagger a + \frac{1}{2} \right) + \frac{p_z^2}{2m_e} \quad (1.29)$$

that gives a spectrum of the Landau levels

$$E_n = \hbar\omega_c \left(n + \frac{1}{2} \right) + \frac{\hbar^2 k_z^2}{2m_e} \quad (1.30)$$

with the cyclotron frequency $\omega_c = \frac{eB}{m_e}$ and leaves the out-of-plane dispersion intact. If an additional Zeeman interaction is added $E_Z = g\mu_B\sigma_z B$, where $\mu_B = \frac{e\hbar}{2m_0}$ is the Bohr magneton and g stands for a g-factor, then the levels become split by $2E_Z$ difference. An

analogical result holds also for holes. By combining the both electron and hole states of the Hamiltonian (1.29) separated by a bandgap E_g , a dispersion of the trivial four-band semiconductor is received with a LL fanchart visualized in the Fig. 1.5. An each spin-split level has a 2D degeneracy $\zeta_{2D} = B/\Phi_0 = eB/h$ per unit area, where $\Phi_0 = h/e$ is a quantum of the magnetic flux. In the Landau gauge the n -th state has the form

$$\psi_n(\mathbf{r}) = \frac{1}{2\pi} e^{i(k_y y + k_z z)} \phi_n(x) \quad (1.31)$$

with a harmonic oscillator eigenfunction

$$\phi_n(x) = \frac{1}{\sqrt{2^n n!} \sqrt{\pi} l_B} \mathbf{H}_n\left(\frac{x - x_0}{l_B}\right) e^{-(x-x_0)^2/2l_B^2}, \quad (1.32)$$

where $x_0 = l_B^2 k_y$ and \mathbf{H}_n denotes a Hermite polynomial. The momentum k_x is no longer a good quantum number and it is replaced by the Landau level index n , a coordinate x_0 represents the x -position of the guiding centre. The y -coordinate is smeared out over the sample's length with the plane wave e^{ik_y} . The momentum k_z and band index N remain unchanged.

In the similar manner, the relativistic case of the Weyl Hamiltonian can be approached yielding

$$H_{\text{W}}^{\frac{1}{2}} = \hbar v \begin{pmatrix} k_z & \frac{\sqrt{2}}{l_B} a \\ \frac{\sqrt{2}}{l_B} a^\dagger & -k_z \end{pmatrix} \quad (1.33)$$

with the zeroth modes $E_{n=0} = \pm k_z$ for $\psi = (0, |0\rangle)^\top$ and with the spectrum

$$E_{n \geq 1} = \pm \hbar v \sqrt{\frac{2n}{l_B^2} + k_z^2} = \pm v \sqrt{2ne\hbar B + (\hbar k_z)^2} \quad (1.34)$$

for the higher ($n > 0$) electron(+) and hole(-) states respectively and with the wavefunctions

$$\psi_{n \geq 1} = \frac{1}{\sqrt{2}} (a_1 |n\rangle, \pm a_2 |n+1\rangle)^\top. \quad (1.35)$$

We obtained the spectrum with \sqrt{B} -dependence that is featured by two chiral 0-th levels, in contrast to the linearly dispersing Landau levels in classical electron gas.

Applying the same procedure to the Kane system (1.16), we end up with the following spectrum

$$\begin{aligned} E_{n,\uparrow, \text{E/H}} &= \frac{E_g}{2} \pm \sqrt{\left(\frac{E_g}{2}\right)^2 + 2\left(\frac{v}{l_B}\right)^2 \left(n - \frac{1}{2} + \frac{1}{4}\right) + (\hbar v k_z)^2} \\ E_{n,\downarrow, \text{E/H}} &= \frac{E_g}{2} \pm \sqrt{\left(\frac{E_g}{2}\right)^2 + 2\left(\frac{v}{l_B}\right)^2 \left(n - \frac{1}{2} - \frac{1}{4}\right) + (\hbar v k_z)^2} \quad \text{for } n \geq 1 \\ E_{n,\uparrow/\downarrow, \text{HH}} &= 0 \quad \text{for } n \geq 0, n \neq 1 \end{aligned} \quad (1.36)$$

with the eigenfunctions listed in refs. [25, 36]. Strictly speaking, all Landau levels have again \sqrt{B} -dependence, however they become mutually split with respect to the spin. The flat band levels are identical zero with one missing level for $n = 1$.

In the quantum regime, with well-resolved Landau levels, it is the cyclotron reso-

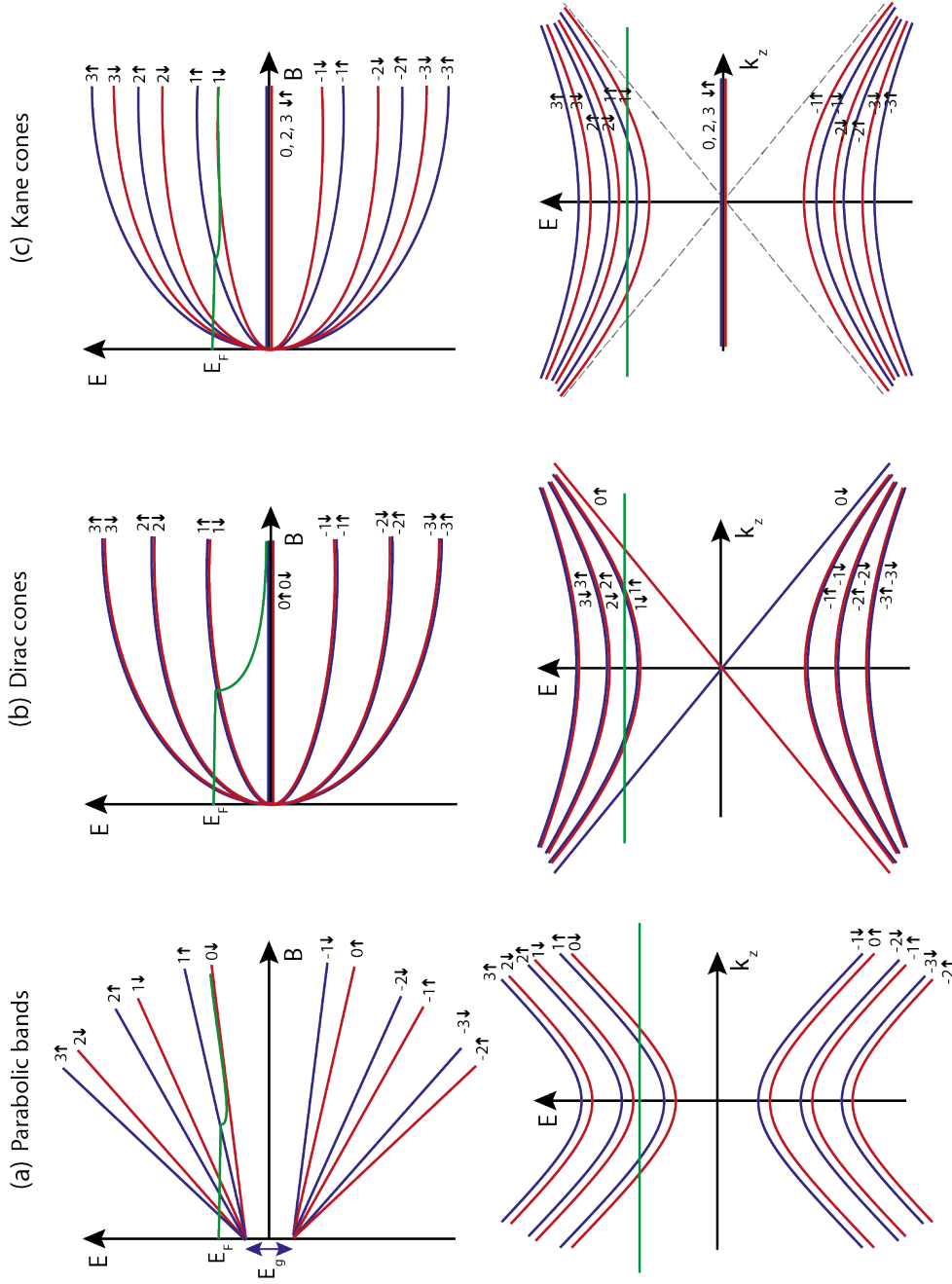


Figure 1.5: In an external magnetic field, the 3D band structure turns into a set of quantized Landau subbands, whose shapes depend on the actual band profile. For the parabolic bands ($E \sim k^2$) the LLs scales linearly $E \sim B$ with the applied magnetic field (a), whereas for the linear bands ($E \sim k$) the LLs develop as a $E \sim \sqrt{B}$ (b, c), since $k_{\pm} \rightarrow \sqrt{2\hbar e B a^{\pm}}$. The out-of-plane motion $E-k_z$ remains free. For the Schrödinger particles, the subbands constitute of the vertically shifted parabolas (bottom panel). In the case of the Dirac and Kane fermions, the asymptotic behaviour converges to the original linear dispersion. The difference in the dispersion between the Dirac and Kane model is specific by the existence of the linear 0-th modes for the former case and for the later case by the presence of the flat band that brings in an additional set of constant levels $n = 0, 2, 3, \dots$. The spin-splitting of the individual levels depends on the strength of spin-orbit interaction in the system.

nance absorption which counterparts the zero-field Drude-type (free-carrier) absorption. In isotropic system (considered above only), such absorption is possible between the adjacent Landau levels (differing in the index by one) with energy $E_{\text{CR}}(B) = E_{n+1} - E_n$. In contrast to conventional systems with equidistant spacing of Landau levels, the cyclotron energy depends on the position of the Fermi level and may have (in particular for half-filled levels and/or at $\kappa_B T$ comparable with level's spacing) multimode character. With an increasing magnetic field, and therefore, gradually rising degeneracy of levels ζ_{2D} , the cyclotron resonance absorption has a form of \sqrt{B} -dependent modes with B -dependent intensity [37].

When the magnetic field is not strong enough to induce well-resolved Landau levels, the cyclotron motions and corresponding absorption of light may be described using approaches of classical physics and the observation of the cyclotron resonance is associated with the mass

$$m_c = \frac{eB}{\omega_c} \quad (1.37)$$

that an electron feels during the motion around the orbit. The cyclotron mass can be defined in the more general form

$$m_c = \frac{\hbar^2}{2\pi} \frac{\partial A_c(k_\perp)}{\partial E_c(k_\perp)} \quad (1.38)$$

where

$$A_c = \pi k_\perp^2 \quad (1.39)$$

represents the area enclosed in the reciprocal space by a charge carrier undergoing the cyclotron motion and $E_c(k_\perp)$ is its kinetic energy at the Fermi level E_F for an arbitrary band dispersion. For a parabolic band the mass m_c corresponds to the effective electron mass m_e , but for the conical band the cyclotron mass leads to the relativistic E_F -dependent formula

$$m_c = \frac{E_F}{v^2} \quad (1.40)$$

or in a case of a small gap to $m_c = (E_F - E_g/2)/v^2$. So, the slope of the cyclotron resonance in the ω_c - B plot tells the information about the effective mass or the velocity.

Summary

In this chapter, we introduce a semimetal as a boundary between the phases with the trivial and inverted band ordering and we further discuss the conditions for an occurrence of the charge neutrality point in the band structure. We address an important consequence for the insulators with an inverted bandgap - an existence of the conductive states on crystal surface. The main objective is to simplify the description of the band structure with linear/parabolic dispersions using an analogy with the relativistic behaviour of a free particle from high energy physics. We compare three different types of band structures - Schrödinger, Dirac and Kane from the viewpoint of the optical response and their respective Landau level structures that emerge in a presence of the magnetic field. In the following chapters, we will try to explain the observed magneto-

1.7. Effect of quantization in magnetic field

optical response of cadmium arsenide and bismuth selenide systems within the provided models and we estimate the concerned parameters.

2. Experimental technique

2.1 Infrared Fourier transform spectroscopy

The primary technique used in this work for probing a material band structure is Fourier transform infrared spectroscopy (FTIR). This powerful and unique tool allows us to study excitations in a broad range of photon frequencies. It is based on a duality between the length of the optical path and photon energy. The frequency dependence of the radiation is obtained via an interference of the two electromagnetic waves phase-shifted by a difference in their optical paths. In comparison with the conventional dispersive instruments, the FTIR has a strong advantage of the high throughput that substantially increases a signal-to-noise ratio and thus compensates the weak (black-body radiation limited) brightness of thermal sources used in the infrared range, because no slits reducing the aperture are needed and the whole signal is recorded at once [38]. The effective spectral range extends over four orders of magnitude from few meV in the terahertz range up to several eV in the ultraviolet domain, completely covering the infrared and visible spectrum. Nevertheless, for these relatively short wavelengths, the dispersive spectrometers equipped with CCDs cameras become more efficient.

A typical setup of a present FTIR experiment consists of a light source, interferometer (mostly of Michelson-type), specimen kept at low temperatures and in an externally applied magnetic field. The detector represents the last element that reads the response and its arrangement differs for the optical configuration of transmission, reflection, photoluminescence respectively.

Transmission and reflectivity

A simplified optical path for transmission is sketched in Fig. 2.1. The body of the evacuated commercial spectrometer from Bruker (Vertex 80v, IFS66s/v or IF113v) includes three thermal light sources - mercury lamp, globar and tungsten lamp covering far, middle or near infrared region, respectively. The radiation emitted by the source passes through 50/50 beamsplitter¹ (Ge coated Mylar, KBr or CaF₂) where the light divides into two legs of the distinct paths. While the first path has a fixed length, the second is flexible in order to modulate a phase difference using a movable mirror stage. Then, the beam is sent into a waveguide and condensed on the probed sample using a simple reflective cone. In the transmission experiment, the outgoing beam is refocused by the second (Winston) cone placed beneath. Then, the beam hits an active element of the bolometer.

The waveguide is sealed from the top by an appropriate optical window (polyethylene, Si, ZnSe, etc.) and mounted in a cylindrical housing. The whole probe is filled up with helium gas to the pressure of 30 mbar for better heat transfer and then inserted into a bath of liquid helium. The cryostat is equipped with a superconducting coil operating up to 11 T at 4.2 K, or up to 13 T at 1.8 K respectively. The magnetic field

¹Optimized to have the best performance at a specific spectral region.

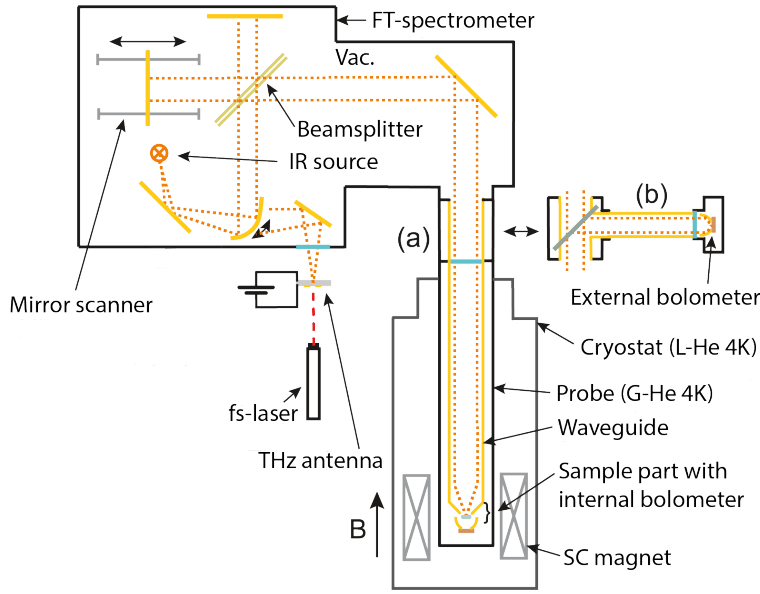


Figure 2.1: Schematics of the optical path in the experimental set-up adjusted for the transmission measurements. The light is irradiated by a source, modulated by a Michelson interferometer, then coupled to the waveguide, transmitted by a sample and finally registered by a detector. The sample is kept at liquid helium temperature and exposed to the magnetic field generated by a superconductive or resistive coil. Once the transmitted intensity is acquired within the scanning range of the mirror, the Fourier transform is performed to obtain a transmittance spectrum. The adjustments could be done to reconfigure the arrangement for the reflectance (b) by an insertion of the beamsplitter and external detector.

is oriented in parallel to the propagating wavevector (Faraday geometry).

The detection and computational part is represented by a block diagram in Fig. 2.2. The incident light is recorded for various positions of the movable mirror by a detector circuited in the series with a load resistor. The voltage across the load is preamplified and sent to the spectrometer, where the x -position is recorded simultaneously. The processing unit performs Fourier transform and returns a conjugated transmission spectrum as a function of the wavevector.

The sample compartment is equipped with a rotation stage, which allows us to measure a proper reference signal. This way, one may realize absolute transmission experiments, but also to correct for B-field induced changes in the response of the bolometer. A particular design of the sample part is adapted to each measurement configuration (Fig. 2.3a-d). In the transmission, a freestanding sample and a pinhole (or eventually a suspended sample versus the substrate) are mounted to the holder. The bolometer is attached below and kept at the same temperature. In order to eliminate the transmission function of the optical elements present in the optical path, a systematic correction of spectra needs to be carried out that also fix for a detectivity function of the bolometer. The transmittance is received as a ratio of the sample over the reference spectrum $T_S(B)/T_R(B)$ in an arbitrary magnetic field. Usually, one is interested in the effect of the relative change in the magnetic field, then the desired ratio $T_S(B)/T_S(0)$ needs to be divided by $T_R(B)/T_R(0)$ to suppress a field-dependent response of the bolometer. The absolute value of the transmittance can be measured, if the identical

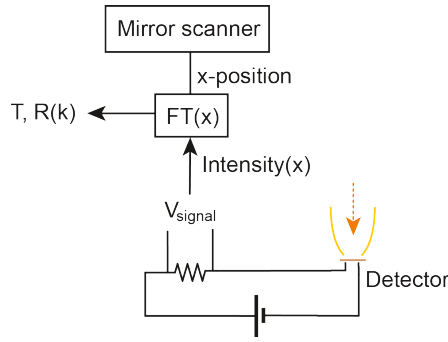


Figure 2.2: A block scheme for the realization of the Fourier transform in the configuration of the transmission/reflection. The voltage across a load resistor represents the intensity that is recorded together with the position of the moving mirror. Then, the Fourier transform of the signal is computed, which provides the conjugated quantity $T(k)$, $R(k)$ as a function of the wavenumber k .

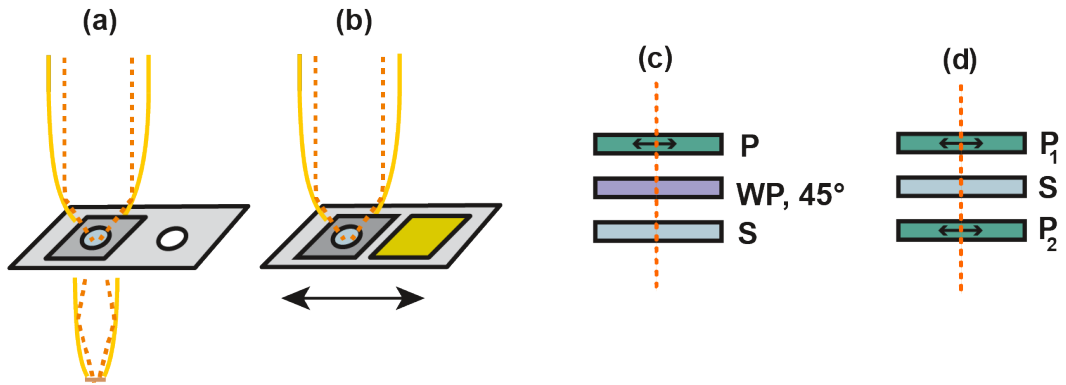


Figure 2.3: (a) A detail of the sample part for the transmission. A condensing cone at the end of the waveguide focuses the light to be passed through the specimen with a defined aperture and redirected by a refocusing insert on a bolometer element. The pinhole (or a golden mirror in the case of reflection (b)) is housed on a rotational stage and serves as a reference. (c) A transparent sandwich composed of the polarizer and quarter-waveplate was used for the selection of a single circularly polarized mode. (d) A sandwich composed of two polarizers used for the Faraday rotation.

apertures are used.

For the reflection geometry a golden mirror with the almost unitary reflectance in the infrared region is used as a reference instead. The reflected beam returns back through the waveguide and it is diverted by an additional beamsplitter outside to the external bolometer (in Fig. 2.1 the neck (a) is replaced with the insert (b)).

In many cases, the analysis of the transmission data is significantly simplified when the signal is recorded in a given circular polarization of the radiation.² Thus, for such purpose a set of a polarizer and MgF_2 quarter-waveplate were used with a mutual rotation of 45 degrees between the fast axis and an easy-pass direction of the polarizer (Fig. 2.3d). A quarter-waveplate of the zero-order was optimized for wavelengths of 4, 5, 6 μm respectively. For the measurement of the Faraday rotation a pair of two co-linear polarizers (wire-grid on KRS5) was used with a specimen sandwiched in between (Fig. 2.3e). In addition, the polarization character of any absorption lines in the transmission experiment can be determined using a pair of polarizers that are mutually tilted by 45 degrees. To enhance brightness of the spectrometer in the far infrared domain, a THz antenna could be employed instead of the classical thermal

²The thermal sources emit light with the equal presence of both polarizations.



Figure 2.4: A photograph of the high magnetic field setup. The setup is located at the experimental room, while the resistive magnet is installed below the floor level. The cryostat and probe are held in the magnet bore by a motorized lift. The spectrometer is placed aside from the undesired stray B -field.

sources (Fig. 2.1). The radiation is emitted by transient current of the photo-generated carriers in GaAs between the two deposited interlaying metallic combs biased to the external electric field [39, 40]. The antenna is pumped by a 780 nm femtosecond laser with the repetition rate of 40 MHz. The generated THz peak is positioned at 4 meV.

The transmission measurements of highly absorbing media as 3D narrow gap/gapless systems impose the minimal requirements on the lateral dimensions of specimens (ideally exceeding $100 \times 100 \mu\text{m}^2$) and also low thickness ($0.2\text{-}2 \mu\text{m}$) for the sake of an intense signal. Such samples can be grown as thin layers by molecular beam epitaxy (MBE) or by chemical vapour deposition (CVD). Another approach offers a top-down fabrication by polishing/cutting into slabs or in the case of layered materials by exfoliation of micro-flakes.

Features of high magnetic field setup

The high field setup is conceptually identical as for the low field (Fig. 2.4). The main distinction is that the magnetic field (up to 36 T) is produced by a resistive coil composed of the outer Bitter-type coils surrounding the inner co-centric helical inserts. In order to achieve such extreme fields the coil composite is supplied with high current

(over 30 kA) that generates significant Joule heating. The total power consumption of the system makes a dominant part of the financial expense for the experiment (24 MW at the maximal field). The whole installation is cooled to the room temperature by a water flow of 150 l/s circulating in a closed loop between the coil and heat exchangers.

The probe is inserted in a funnel-shaped cryostat with a long tail and the entire body is introduced into a 34 mm bore of the magnet. The cryostat is centred within the bore to maintain an air gap between the walls to avoid the transfer of any mechanical vibrations from the cooling system to the optics. The vibrations also give rise to so called bubbling effects of He at 4 K which substantially enhances its evaporation. From that reason the He bath is kept below the lambda point during the measurements. The intense and homogeneous field is possible due to the narrow bore of the magnet requiring the miniaturization of the sample stage. To avoid high losses in a long lightpipe due to the multiple reflections the inner surface is gold-plated. The spectrometer, situated out of the reach of the stray B -field, is coupled to the probe via a robust stainless steel (non-magnetic) waveguide.

Photoluminescence at low fields

In the photoluminescence (PL) configuration, the sample is excited by a 660 nm diode laser coupled to an optical fiber delivering on the sample the excitation power of ≈ 0.1 mW (Fig. 2.5). The emission is collected by a ZnSe lens providing a nearly collimated beam, which is afterwards focused at the entrance of the spectrometer, passes reversely the interferometer and is absorbed by an external detector (in our case HgCdTe). The beam is diverted towards the detector by a positionable mirror. The acquisition can run in a standard scanning mode of the spectrometer. In such a case, the PL signal is recorded along with the parasitic black-body radiation of the setup (with a maximum at the wavelength around 10 μm). Another possibility is to synchronize the detected signal in a step-scan mode by a lock-in amplifier that chops the excitation laser at a precise frequency to reduce the noise and to select the true emission. Currently, an upgraded design of the sample part is being integrated using a Cassegrain system with a strong advantages concerning the intensity of the detected signal over the solution with lens. Firstly, the reflective optical elements are not sensitive to the investigated wavelengths. Secondly, when the excitation laser propagates freely in the same lightpipe together with the outgoing emission, the both beams are auto-focused at the same spot on the sample surface.

2.2 Transport measurement

The electronic transport in the magnetic field serves as a complementary technique to magneto-optical measurements. The carrier concentration can be extracted from the Hall measurements and the Fermi surface cross-section $A(k_{\perp})$ is directly provided from the well-defined periods of Shubnikov-de Haas oscillations.

The resistivity is measured in the four-terminal scheme by a synchronous lock-in detection (Fig. 2.6). The specimen is connected in series with the load resistor of

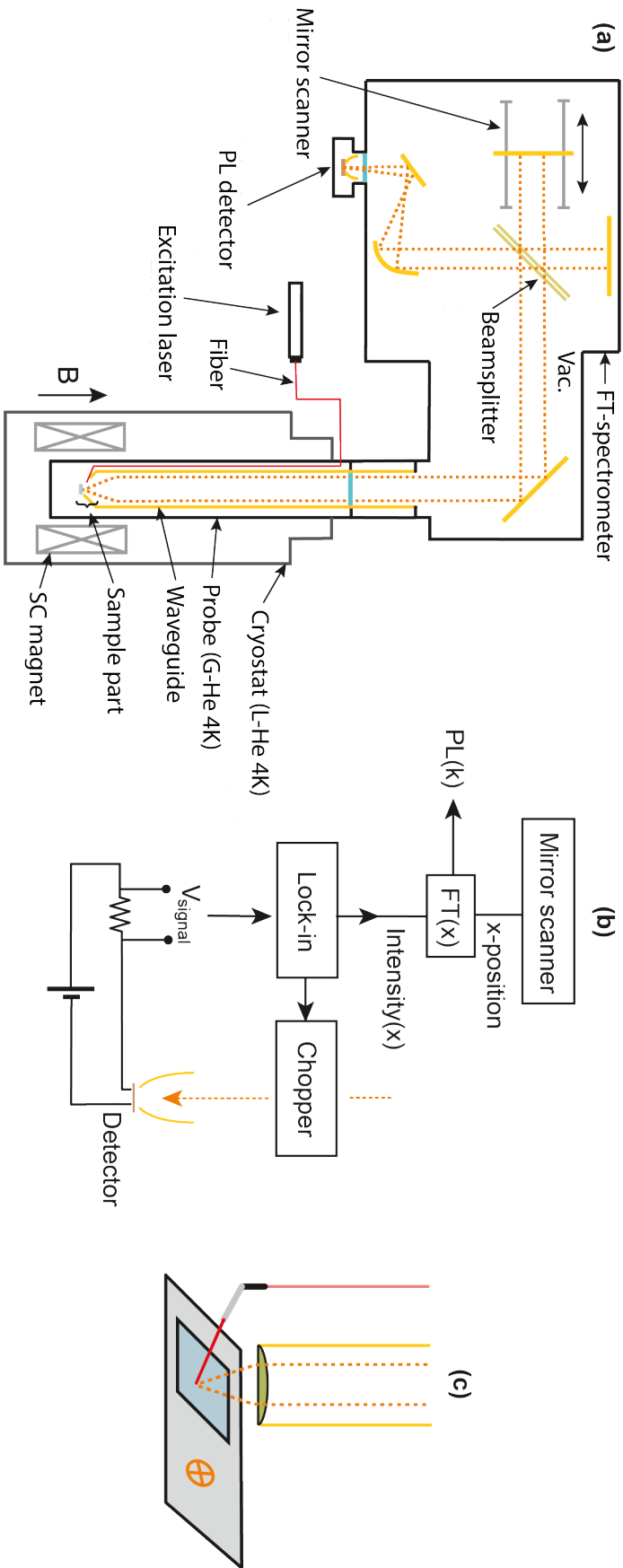


Figure 2.5: (a) The photoluminescence can be measured through the reversed beam path, when the detector is positioned after the passage in the scanner. (b) The spectrometer operates in a step-scan mode when the signal is read out by a lock-in detector at a given frequency that is synchronized with the laser excitation for each step of the mirror (compare with the diagram in Fig. 2.2). (c) A detail of the sample part adopted for PL. The excitation laser is delivered to the sample by an optical fiber. The emission is collected via a ZnSe lens placed at the focal distance to collimate the outgoing beam. A tungsten lightbulb is used as a referential point source.

2.2. Transport measurement

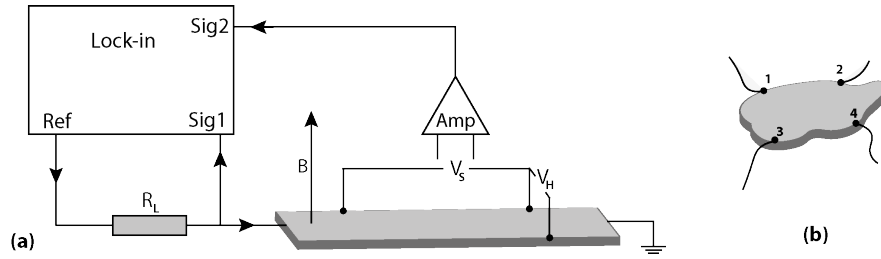


Figure 2.6: (a) A basic experimental scheme used for the transport measurements in a linear four-terminal geometry. The current is computed from the voltage drop on the load resistor. Both readings are synchronized with the reference sampling of the lock-in. The longitudinal and transversal voltages V_s, V_H are preamplified before. (b) The Van der Pauw arrangements of the contacts on an irregularly shaped sample.

(typically $100 \text{ M}\Omega$) to read precisely the carrying current (usually in orders of nA), while the voltage is set to few volts. The measured voltage is 100x preamplified before the recording and the carrier frequency is set to $\sim 10 \text{ Hz}$ to suppress the out-of-phase noise. The exit terminal of the sample is grounded. The holder is mounted in a probe filled with exchange gas and inserted into the liquid He cryostat. The magnetic field is applied in perpendicular to the top surface of the sample. A heating insert allows to continuously vary temperature between 1.8-300 K.

The four-terminal sensing is realized in either a linear arrangement (Hall bar) or in the Van der Pauw geometry for the irregularly shaped planar samples assuming the constant thickness. In most cases, nearly Ohmic point contacts are prepared using a standard silver paste. The Hall coefficient can be estimated from the transversal voltage U_H , assuming that the transport is mediated by single type of carriers, as

$$R_H = \frac{U_H}{I_c} = \frac{1}{Ne} \quad (2.1)$$

with N being the electron/hole concentration respectively.

For the Van der Pauw method the sheet resistivity R_s is obtained by a numerical solution of the equation

$$1 = \exp\left(-\pi \frac{R_{12,34}}{R_s}\right) + \exp\left(-\pi \frac{R_{23,41}}{R_s}\right), \quad (2.2)$$

where the auxiliary components of the resistivity are defined as

$$R_{12,34} = \frac{U_{34}}{I_{12}}, \quad R_{23,41} = \frac{U_{41}}{I_{23}}. \quad (2.3)$$

3. Magneto-optics of Cd_3As_2

3.1 The state of the art

Cadmium arsenide has been recently theoretically identified as a material which may host 3D Dirac cones and represent thus a 3D analogue of graphene [15]. Arguments based on symmetry and topological classification discuss the band inversion present in the material as well as the importance of a single C_4 -axis of symmetry that would protect the residing cones. The theoretical predictions led to a renewed interest in its properties being attracted by novel phenomena related to the Dirac physics in all three spatial dimensions. However, the material was already intensively studied over several decades by the means of transport and optics to understand its unusually high mobility. The quality of its technological processing advanced with the progress of growth in $\text{II}_3\text{-V}_2$ compounds. The recent investigations profited from those advances and further expanded already fairly solid knowledge about this system.

Cadmium arsenide at exact stoichiometry undergoes two phase transitions during the process of cooling [41]. The high-temperature phase $T > 900$ K crystallizes in the accurate antiferroite structure M_2X with the lattice parameter $a_0 = 6.24 \text{ \AA}$ in the space group $\text{Fm}\bar{3}\text{m}$, where $\frac{1}{4}$ deficiency of cadmium atoms is compensated by randomly distributed vacancies. In the range 750-900 K, an intermediate phase occurs with the group $\text{P4}_2/\text{nmc}$ and its tetragonal unit cell has size $\sqrt{2}a_0 \times \sqrt{2}a_0 \times 2a_0$ with vacancies stacked in the channels along the b -axis. Below 750 K a low temperature phase is formed as a supercell in the centrosymmetric group $\text{I4}_1/\text{acd}$ obtained from the previous structure but with the new dimensions $2a_0 \times 4a_0$.

For the sake of simplified description of the band structure, an analytical truncated k .p model for the vicinity of the Brillouin zone center was developed by J. Bodnar [42] approaching thus a conventional Kane model widely used for the zincblende, rocksalt and antiferroite lattices ($\text{Fm}\bar{3}\text{m}$ group). This model became easy to handle since it contains just few band parameters deduced from the transport experiments [43]. Its validity is limited to the vicinity of the Γ -point and takes into account eight spin-degenerated bands E, HH, LH, SH. Later on, P. Wallace [44] and M. Singh [45, 46] further expanded the Bodnar model including Landau quantization for the case of the magnetic field. The subsequent ab-initio studies [47, 48] suggested that the presence of Cd vacancies in the simplest antiferroite lattice causes an additional pseudopotential that gives probably rise to the inverted ordering with a small gap at the Γ -point between E and LH bands. Then, the band structure with a narrow gap resembles in a simple view the situation of the semiconductor-semimetal transition. Moreover, the system can be alloyed by substituting the one of two elements [49, 50], e.g. $\text{Cd}_{3-x}\text{Zn}_x\text{As}_2$, or $\text{Cd}_3\text{P}_x\text{As}_{2-x}$ to achieve a gapless Kane case for a certain critical compositions. In addition to the Kane approach, the Bodnar model further introduces an additional perturbative crystal field that reflects the tetragonal distortion of the cell. The perturbation primarily acts between LH and HH p-states, causes the splitting of the bands and it may potentially lead to the occurrence of the appealing small Dirac-like band

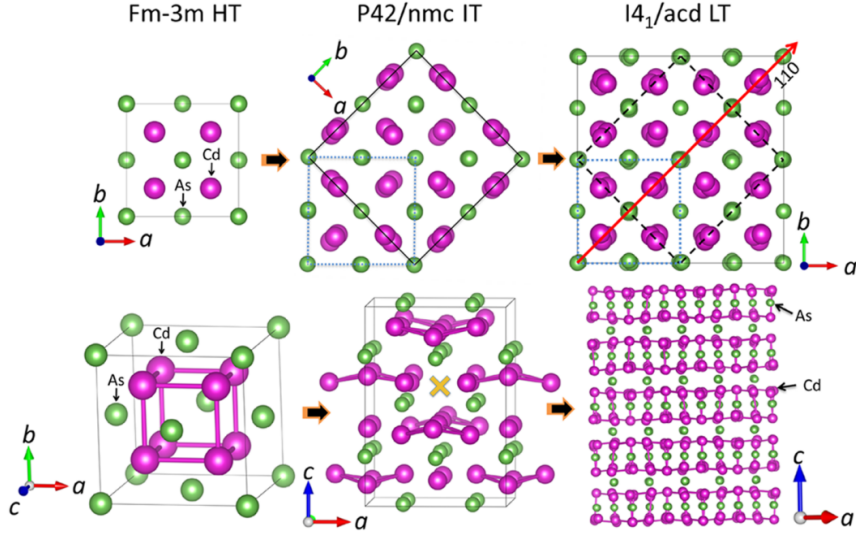


Figure 3.1: Temperature dependent polymorphism of Cd_3As_2 [41] (a) At high temperature $T > 900$ K, the atoms produce anti-fluorite arrangement M_2X normally consisting of twelve atoms. But, here just six Cd atoms are for the disposal to the each four As atoms in a cell which gives rise to two Cd vacancies that distorts the positions of Cd atoms. (b) At the medium temperatures 750-900 K, the Cd vacancies reorganise to more stable positions forming a bigger cell containing 80 atoms with a characteristic tunnel voids along the b -axis (yellow cross). (c) A complex supercell with 160 atoms is created below 750 K. The vacancies are redistributed in a helical form of 4_1 . Only this structure has an inversion symmetry.

crossing, doubled along C_4 z -axis at $\pm k_D$ points.

The recent DFT calculations [10, 51] suggested a presence of those tiny Dirac crossings at the scale of 50 meV between the top-most LH and HH bands, but therein the band inversion is supposed to be more significant in the way that the E band is shifted even below the SH band. This contrast to the Bodnar model could be explained by a general systematic error of the LDA methods in the bandgap under/over-estimations of normal/inverted shallow gap systems [52, 53]. On the other hand, the results of the latest computation [54] confirmed the Bodnar structure for the complex supercell and showed a band crossing (crystal field splitting) in the scale of 30 meV.

Motivated by the theoretical predictions, surface sensitive ARPES [55–57] were recently employed to map the band structure of Cd_3As_2 and to prove experimentally the existence of the Dirac cones. These studies found a 3D conical (needle-like) conduction band spanning over hundreds of meV and touching a much flatter band at a single point as is shown in the Fig. 3.2a,b [56]. The former figure depicts the E - k dispersion for the four topmost bands averaged over a wide range of excitation energies and thus a possible exclusion of any band due to the particular sensitivity to a photon energy is avoided. The upper extension of the cone is determined by a typical Fermi level in undoped as-grown Cd_3As_2 crystals that could be also slightly increased by deposition of potassium [57]. The related slope of the top cone provides an estimation of the velocity $\approx 1.5 \times 10^6$ m/s. But, the precise read-out of the velocity parameter may be difficult due to the projection of the bulk band into a 2D plane. The authors of the ARPES studies congruently interpreted this cone as Dirac-type.

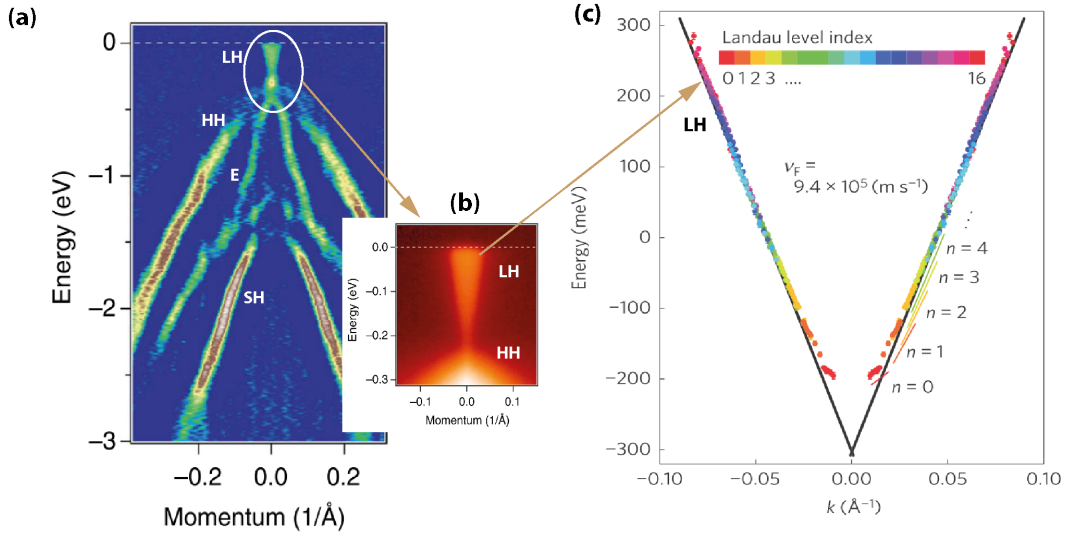


Figure 3.2: (a) A second derivative of the ARPES dispersion map [56] over a wide energy range with the labelling of the inverted bands after Bodnar [42]. (b) The inset portrays a Kane-type cone touching a flatter band. (c) The Landau levels of the conduction band measured by STM were normalized with respect to their indices and collapsed on a single dispersion line with a slope providing the value of the velocity [58].

Another important insight was brought by an STM study [58] performed on a reconstructed (112) arsenic plane in the magnetic field, where a series of spin-split Landau levels in the conduction band was observed in the dependence on the tunnelling voltage tuned over the range of 0.6 eV. The velocity parameter $v = 0.94 \times 10^6 \text{ m/s}$ was extracted from the slope of a single linear dispersion (Fig. 3.2c) with the use of the Born-Sommerfeld quantization condition, when the Landau level energies are rescaled with respect to their indexation (sec. 3.6). Fairly large values of g-factors were extracted from the splitting of the Landau levels as a function of the energy reaching 10-20 at the energy of $E = 250 \text{ meV}$ above the nodal point. Besides, the analysis of the STM quasiparticle interferences showed also an existence of another conduction band at the Γ -point, whose bottom is shifted 450 meV above the nodal point. Such an idea was proposed sooner from the results of Shubnikov de-Haas oscillations measured on a series of highly n-doped samples [59]. In contrast to the ARPES interpretations, the authors in the STM study assumed different scenario and proposed the realization of the Dirac cones as a result of the band crossing between the conduction and the first valence band with the estimated maximal size of 30 meV.

These manifestations stimulated an intensive activity in transport experiments done on samples of various forms such as needle-like bulk crystals, etched microstructures, nanoribbons or nanowires. Besides the record electronic mobility [60] with its ambipolar character close to charge neutrality point [61], a large negative longitudinal magnetoresistance [62] (in geometry $E \parallel B$ -inplane) was found together with strong spin-splitting of Landau levels [63,64]. The several studies also reported on a contribution to the total conductivity through the surface channels explained via Fermi-arc-mediated

transfer of chirality [65] and with the observation of Aharonov-Bohm interference in quasi-ballistic regime [66]. Moreover, an unconventional superconductive phase was found at the point contact between Cd_3As_2 and metal [67]. The interpretation of those studies depends directly or indirectly on the realization of the symmetry-protected 3D Dirac cones in the band structure.

Importantly, the results of STM/STS experiments are thus in a clear contradiction to above discussed conclusions of ARPES measurements, providing us with estimates of the Dirac cone extension, which differ by more than one order of magnitude. Interestingly, this crucial disagreement is barely mentioned in the current extended literature about this material and leaves the community in a surprising uncertainty about the real band structure of Cd_3As_2 . This controversy also partly represents our motivation to investigate this system using another, independent experimental technique. As it will be shown in this chapter, the infrared magneto-optical spectroscopy, supported by an appropriate theoretical model of the Cd_3As_2 band structure, may resolve this controversy.

3.2 Bodnar Hamiltonian at zero field

Assuming the Bloch wavefunctions $\psi_{n,\mathbf{k}} = u_{n,\mathbf{k}} e^{i\mathbf{k}\mathbf{r}}$ to be the solution, the Schrödinger equation for an electron reads [35, 68, 69]

$$\left(\frac{p^2}{2m_0} + V + \frac{\hbar}{m_0} \mathbf{k} \cdot \mathbf{p} + \frac{\hbar}{4m_0^2 c^2} (\nabla V \times \mathbf{p}) \cdot \boldsymbol{\sigma} + \frac{\hbar^2}{4m_0^2 c^2} (\nabla V \times \mathbf{k}) \cdot \boldsymbol{\sigma} \right) u_{n,\mathbf{k}} = \left(E_{n,\mathbf{k}} - \frac{\hbar^2 k^2}{2m_0} \right) u_{n,\mathbf{k}} \quad (3.1)$$

in a periodic potential $V(\mathbf{r}) = V_0 + V_c$, where V_0 has a cubic symmetry and V_c is a contribution caused by the tetragonal distortion that is further neglected in the spin-orbit coupling terms. The fourth term of eq. (3.1) is disregarded since the most of the spin-orbit interaction occurs in the interior of the atom, where $p \gg k$. The equation (3.1) can be expressed using energy representation of the JM-basis (1.14) sorted as $E^\uparrow, E^\downarrow, \text{HH}^\uparrow, \text{HH}^\downarrow, \text{LH}^\uparrow, \text{LH}^\downarrow, \text{SH}^\uparrow, \text{SH}^\downarrow$ in order to obtain an eigenvalue problem $\sum_n H_{mn} c_n = E c_m$. The perturbed Hamiltonian [46] then takes the form¹

$$\begin{bmatrix} E_g & 0 & P_\perp k_+ & 0 & \sqrt{\frac{2}{3}} P_\parallel k_z & \sqrt{\frac{1}{3}} P_\perp k_- & \sqrt{\frac{1}{3}} P_\parallel k_z & -\sqrt{\frac{2}{3}} P_\perp k_- \\ 0 & E_g & 0 & P_\perp k_- & -\sqrt{\frac{1}{3}} P_\perp k_+ & \sqrt{\frac{2}{3}} P_\parallel k_z & \sqrt{\frac{2}{3}} P_\perp k_+ & \sqrt{\frac{1}{3}} P_\parallel k_z \\ P_\perp k_- & 0 & 0 & 0 & 0 & 0 & 0 & 0 \\ 0 & P_\perp k_+ & 0 & 0 & 0 & 0 & 0 & 0 \\ \sqrt{\frac{2}{3}} P_\parallel k_z & -\sqrt{\frac{1}{3}} P_\perp k_- & 0 & 0 & -\frac{2}{3} \delta & 0 & -\frac{\sqrt{2}}{3} \delta & 0 \\ \sqrt{\frac{1}{3}} P_\perp k_+ & \sqrt{\frac{2}{3}} P_\parallel k_z & 0 & 0 & 0 & -\frac{2}{3} \delta & 0 & -\frac{\sqrt{2}}{3} \delta \\ \sqrt{\frac{1}{3}} P_\parallel k_z & \sqrt{\frac{2}{3}} P_\perp k_- & 0 & 0 & -\frac{\sqrt{2}}{3} \delta & 0 & -(\Delta + \frac{1}{3} \delta) & 0 \\ -\sqrt{\frac{2}{3}} P_\perp k_+ & \sqrt{\frac{1}{3}} P_\parallel k_z & 0 & 0 & 0 & -\frac{\sqrt{2}}{3} \delta & 0 & -(\Delta + \frac{1}{3} \delta) \end{bmatrix} \quad (3.2)$$

¹In this context, we redefine $k_\pm = \frac{1}{\sqrt{2}}(k_x \pm ik_y)$.

3.2. Bodnar Hamiltonian at zero field

Table 3.1: The list of the Bodnar parameters as obtained from the analysis of Shubnikov de-Haas oscillations [42, 46].

E_g [meV]	P_{\perp} [eV.Å]	P_{\parallel} [eV.Å]	Δ [meV]	δ [meV]
-95	7.43	7.21	270	85

with the anisotropic Kane matrix element taking in to account the tetragonal distortion of Cd₃As₂

$$P_{\perp} = -\frac{i\hbar}{m_0} \langle s|p_x|u_x \rangle = -\frac{i\hbar}{m_0} \langle s|p_y|u_y \rangle, \quad P_{\parallel} = -\frac{i\hbar}{m_0} \langle s|p_z|u_z \rangle \quad (3.3)$$

and with the spin-orbit splitting $\Delta = i\frac{3\hbar}{4m_0^2c^2} \langle u_x | (\nabla V_0 \times \mathbf{p})_z | u_y \rangle$ symmetrical for all combinations of components and with a crystal field anisotropy δ defined as

$$\langle u_z | V_c | u_z \rangle = \langle s | V_c | s \rangle - \frac{2}{3}\delta = \langle u_x | V_c | u_x \rangle - \delta \quad (3.4)$$

that fixes the position of zero to the top of the heavy hole band. The Kane matrix element P can be rewritten into the form of velocity parameter v or into the Kane energy E_P in the following way $v = \sqrt{\frac{2}{3}}P/\hbar$ and $E_P = 2m_0P^2/\hbar^2$. To obtain the energy spectrum $E_n(k)$ of the above Hamiltonian (3.2), we have to find the roots of the secular equation

$$\gamma(E) = f_1(E)(k_x^2 + k_y^2) + f_2(E)k_z^2, \quad (3.5)$$

expressed with the use of the auxiliary functions

$$\begin{aligned} \gamma(E) &= E(E - E_g)[E(E + \Delta) + \delta(E + \frac{2}{3}\Delta)], \\ f_1(E) &= P_{\perp}^2[E(E + \frac{2}{3}\Delta) + \delta(E + \frac{1}{3}\Delta)], \\ f_2(E) &= P_{\parallel}^2E(E + \frac{2}{3}\Delta). \end{aligned} \quad (3.6)$$

The eigenvalues are doubly degenerate with respect to the spin and may be expressed analytically (only) at the Γ -point

$$\begin{aligned} E_1 &= E_g, \quad E_2 = 0, \\ E_3 &= -\frac{1}{2}(\Delta + \delta) + \sqrt{\frac{1}{4}(\Delta - \frac{1}{3}\delta)^2 + \frac{2}{9}\delta^2}, \\ E_4 &= -\frac{1}{2}(\Delta + \delta) - \sqrt{\frac{1}{4}(\Delta - \frac{1}{3}\delta)^2 + \frac{2}{9}\delta^2}, \end{aligned} \quad (3.7)$$

with the assignment to bands $E_E, E_{HH}, E_{LH}, E_{SH}$ that depends on the ratio between E_g, δ (Fig. 3.3). With the use of the parameters extracted from the Shubnikov de-Haas oscillations, Bodnar concluded the band structure as is depicted in the Fig. 3.4. The plot reveals the existence of two Dirac points lying on the k_z -axis at $k_D = \pm\sqrt{|E_g|\delta} P_{\parallel}^2$ as an outcome of the intersection between the heavy hole and inverted light hole band (for $\delta > 0$). The Bodnar Hamiltonian reduces to the classical Kane model for a vanishing anisotropy $P_{\perp} = P_{\parallel} = P$ and the crystal field $\delta = 0$. Further, for the gapless case $E_g = 0$ the pure Kane conical structure is received. If the spin-orbit interaction is additionally

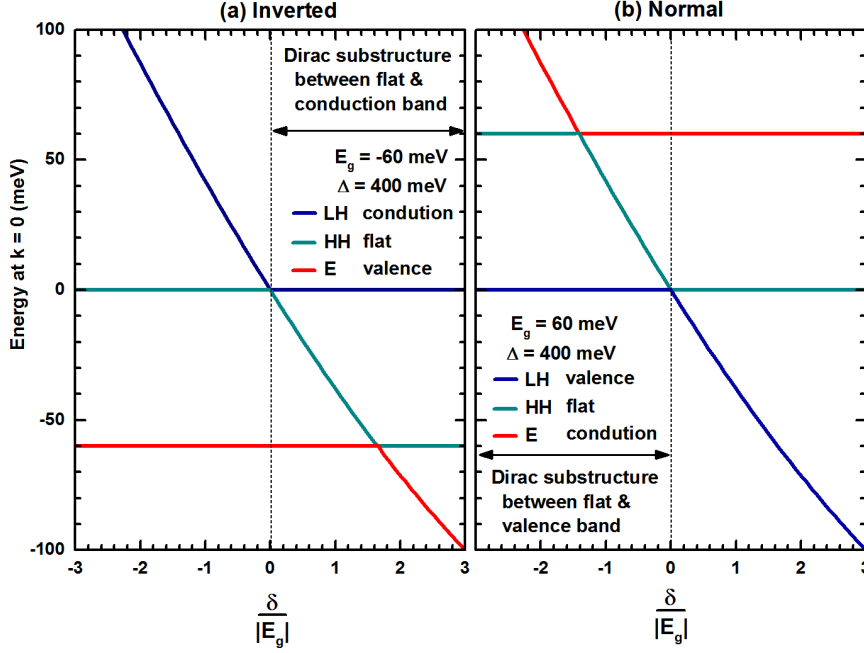


Figure 3.3: The crossing of the light hole and heavy hole bands is formed under the condition of $\delta > 0$ for the inverted ($E_g < 0$) and $\delta < 0$ for the normal ($E_g > 0$) band ordering respectively. For the fixed bandgap, the roots (3.7) of the zero-field Bodnar model at the Γ -point are associated individually with the electron, heavy hole and light hole band in the dependence on the crystal splitting δ to maintain the band ordering. The parameters were taken from the Tab. 3.3.

suppressed $\Delta = 0$, the HH and SH band coincide and induce four-fold degeneracy of the flat band, while the E and LH cones gain the velocity $v = P/\hbar$. Oppositely, when $\Delta \rightarrow \infty$ the SH band becomes decoupled from the rest of the bands and the model truncates to eq. (1.16) (i.e., $\frac{1}{\sqrt{3}}$ - T_3 -like problem) with the velocity $v = \sqrt{\frac{2}{3}}\hbar P$.

3.3 Landau level spectrum for Bodnar model in (001)-orientation

The energy spectrum of the Bodnar Hamiltonian has quasi-analytical solution for the magnetic field oriented along the direction $(001)^\top$. The distinct directions modify the profiles of LLs and thus could serve as a tool to probe an anisotropy of the material. However, their solution needs to be treated numerically. For our purpose we are specifically interested in the direction $\frac{1}{\sqrt{3}}(111)^\top$ which corresponds to the natural (perpendicular) cleavage plane of Cd_3As_2 . Further in the text, the direction $[111]$ in $\text{Fm}\bar{3}\text{m}$ is interchanged with a formally equivalent $[112]$ direction of the $I4_1/acd$ space group.

We transform the Hamiltonian (3.2) to the LS-basis sorted as

$$s^\uparrow, u_{-1}^\uparrow, u_{+1}^\uparrow, u_0^\downarrow, s^\downarrow, u_{+1}^\downarrow, u_{-1}^\downarrow, u_0^\uparrow$$

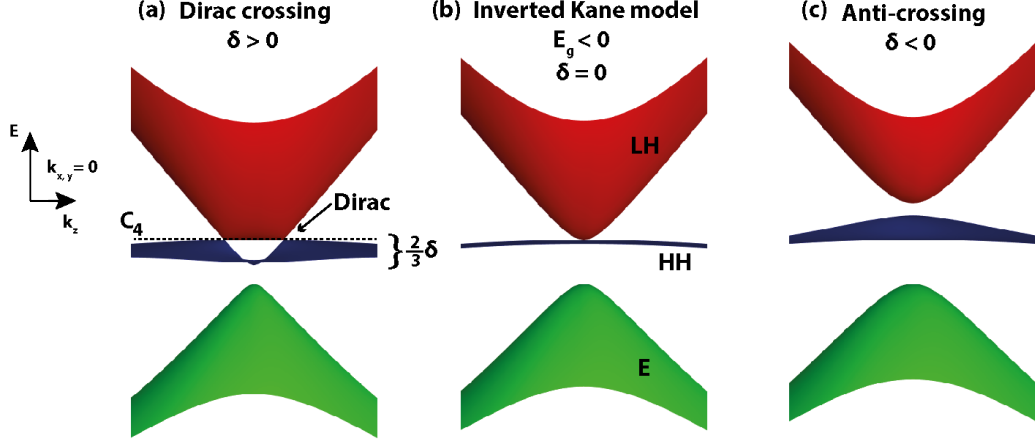


Figure 3.4: A distortion from the cubic symmetry to the tetragonal for the case of the inverted band ordering (b) brings about to an additional crystal field splitting δ that lifts the degeneracy between the LH and HH bands at $k = 0$ and for $\delta > 0$ it necessary leads to the band crossing (a) and thus to an occurrence of two Dirac points located on the remaining longitudinal C_4 z -axis with highly tilted cones. The opposite sign of the deformation causes anti-crossing and opens a small gap instead (c).

to obtain a simpler form for the blocks with spin up and down [70, 71]

$$\begin{bmatrix} E_g & P_{\perp}k_{+} & P_{\perp}k_{-} & 0 & 0 & 0 & 0 & P_{\parallel}k_z \\ P_{\perp}k_{-} & 0 & 0 & 0 & 0 & 0 & 0 & 0 \\ P_{\perp}k_{+} & 0 & -\frac{2}{3}\Delta & \frac{\sqrt{2}}{3}\Delta & 0 & 0 & 0 & 0 \\ 0 & 0 & \frac{\sqrt{2}}{3}\Delta & -(\delta + \frac{\Delta}{3}) & P_{\parallel}k_z & 0 & 0 & 0 \\ 0 & 0 & 0 & P_{\parallel}k_z & E_g & P_{\perp}k_{-} & -P_{\perp}k_{+} & 0 \\ 0 & 0 & 0 & 0 & P_{\perp}k_{+} & 0 & 0 & 0 \\ 0 & 0 & 0 & 0 & -P_{\perp}k_{-} & 0 & -\frac{2}{3}\Delta & \frac{\sqrt{2}}{3}\Delta \\ P_{\parallel}k_z & 0 & 0 & 0 & 0 & 0 & \frac{\sqrt{2}}{3}\Delta & -(\delta + \frac{\Delta}{3}) \end{bmatrix}. \quad (3.8)$$

The quantization is introduced to the system via Peierls substitution. Assuming $k_z = 0$, the 4×4 spin blocks of the Hamiltonian become decoupled. The ansatz for the wavefunction for $n \geq 2$ can be searched in the form $\psi_{n,\downarrow} = (a_5|n\rangle, a_6|n+1\rangle, a_7|n-1\rangle, a_8|n-1\rangle)^T$ for the spin up block

$$\begin{bmatrix} E_g & \frac{P_{\perp}}{l_B}\sqrt{n-1} & \frac{P_{\perp}}{l_B}\sqrt{n} & 0 \\ \frac{P_{\perp}}{l_B}\sqrt{n-1} & 0 & 0 & 0 \\ \frac{P_{\perp}}{l_B}\sqrt{n} & 0 & -\frac{2}{3}\Delta & \frac{\sqrt{2}}{3}\Delta \\ 0 & 0 & \frac{\sqrt{2}}{3}\Delta & -(\delta + \frac{\Delta}{3}) \end{bmatrix} \quad (3.9)$$

and analogically for the spin down $\psi_{n,\downarrow} = (a_1|n\rangle, a_2|n-1\rangle, a_3|n+1\rangle, a_4|n+1\rangle)^\top$

$$\begin{bmatrix} E_g & \frac{P_\perp}{l_B}\sqrt{n} & -\frac{P_\perp}{l_B}\sqrt{n-1} & 0 \\ \frac{P_\perp}{l_B}\sqrt{n} & 0 & 0 & 0 \\ -\frac{P_\perp}{l_B}\sqrt{n-1} & 0 & -\frac{2}{3}\Delta & \frac{\sqrt{2}}{3}\Delta \\ 0 & 0 & \frac{\sqrt{2}}{3}\Delta & -(\delta + \frac{\Delta}{3}) \end{bmatrix}. \quad (3.10)$$

The cases of $n = 0$ and $n = 1$ need to be treated specially. For $n = 0$ the wavefunctions read $\psi_{0,\uparrow} = (0, 0, a_3|0\rangle, a_4|0\rangle)^\top$ and $\psi_{0,\downarrow} = (0, a_6|0\rangle, 0, 0)^\top$ with the corresponding energies

$$E_{0,\uparrow} = 0, \quad E_{0,\downarrow} = -\frac{1}{2}(\Delta + \delta) \pm \sqrt{\frac{1}{4}(\Delta + \frac{\delta}{3})^2 + \frac{2}{9}\delta^2} \quad (3.11)$$

for the LH, HH, SH bands respectively. Similarly for $n = 1$, we assume the solution in the form $\psi_{1,\downarrow} = (a_1|0\rangle, 0, a_3|1\rangle, a_4|1\rangle)^\top$ to get the associated eigenenergies for $LH^\downarrow, E^\downarrow$

$$E_{1,\downarrow} = -\frac{E_g}{2} \pm \sqrt{\left(\frac{E_g}{2}\right)^2 + \left(\frac{P_\perp}{l_B}\right)^2}. \quad (3.12)$$

The related Landau level fan of the E, HH, LH bands is depicted in the Fig. 3.5a for the parameters similar to those implied by the original Bodnar's work (Tab. 3.1). The tendency of levels at high energies $|E| \gg |E_g|$ is fairly similar to the gapless Kane model with just a slight deformation of the levels for the inverted E band due to the proximity of the SH band for an intermediate value of SOC ($\Delta \approx 0.4$ eV). Besides, the small perturbation δ affects only low energies $|E| \sim |E_g|$. The impact of anisotropic P was not taken into account as we assumed $k_z = 0$. Firstly, the bands LH and HH are gapped by factor $\frac{2}{3}\delta$ with the constant 0^\uparrow level pinned to the LH band, whereas the level 1^\downarrow is pinned to HH and disperses upwards. This behaviour, characteristic to all systems with the inverted band structure and also observed in other compounds [72, 73], unavoidably leads to the crossing at the critical field $B_c \approx 1-2$ T (Fig. 3.5a). Since the free-electron term in eq. (3.1) was neglected, the field-dependence of the Landau levels originating in the HH band is related to the non-zero parameter δ . In the Kane model, with $\delta = 0$, the HH levels do not show any evolution with B . In the Bodnar model for fixed $B < B_c$, the levels $0^\uparrow, 1^\downarrow$ intersect for certain momenta $k_z \approx \pm k_D$ and play the role of k_z -dispersing zeroth modes in 3D Dirac semimetals with highly tilted cones.

3.4 Sample preparation

For the reflectivity measurement the bulk crystal samples were used with either naturally-grown shiny (112) planes or polished (001)-oriented planes.² The crystals with typical volume of 2-10 mm³ were grown by sublimation of polycrystalline powder in a closed quartz capsule with a cold end routed outside the furnace [74]. For the transmission

²We remind here that (112) plane of the real structure is assumed to be identical with (111) in the Bodnar model.

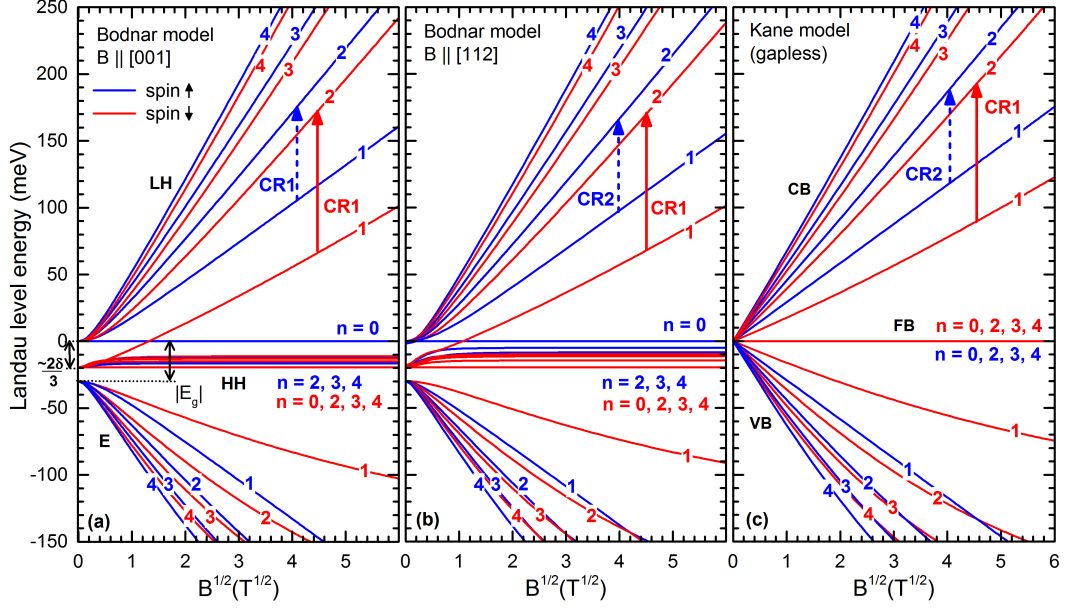


Figure 3.5: Comparison of LL fan charts for the Bodnar and Kane model for parameters $E_g = -30$ meV, $\delta = 30$ meV, $\Delta = 0.4$ eV and $P = 7.5$ eV.Å. The crystal field splits the flat band into a quasi-continuum of levels with breadth of $\frac{1}{3}\delta$ that is slightly dependent on the crystal orientation (b). An irregularity appears for levels 0^\uparrow and 1^\downarrow that are pinned to the LH and HH bands respectively and create a crossing at the low field (≈ 2 T), which can be viewed as an intersection of 0-th modes in the Dirac model (Fig. 1.5). The behaviour at large energies $E > 100$ meV is fairly well isotropic and close to the parental Kane gapless model in the limit of small E_g . The vertical arrows denoted by CR represent two fundamental cyclotron resonances for the spin up/down in the quantum limit of the system.

measurement, the slabs polished from bulk pieces or as-grown thin plates were used. The self-standing plates with typical dimensions $2.5 \times 1.5 \times 0.05$ - 0.1 mm³ were produced by downstream deposition from a stoichiometric melt in a tubular furnace purged by argon held at 900 K [49, 75, 76]. The material was grown at the Institute of Applied Physics in Chisinau by E. Arushanov et al., at the Institute of Physics in Taipei by R. Sankar or in the Department of Chemistry at the Princeton University by R. J. Cava et al.

For most of the samples the crystallographic orientation of the optical facets was determined from the x-ray diffraction using either symmetric scan or Laue method (Fig. 3.6). Typically, bulk samples were composed of a few grains of size in order of 0.1 mm that are mutually misoriented by approximately 0.1-0.2 deg. Such low angle mosaicity makes distinguishing between (100), (001)-facets complicated with an absolute guarantee. Since the diffraction maxima (008), (0016) from (100) and (001) planes are misaligned only by ~ 0.3 deg. In contrast, the plate samples have a tendency for twinning and consist of several domains mutually rotated by 120 deg in the horizontal plane.

To realize transmission experiments on Cd₃As₂, which is a (nearly) gapless material and therefore strongly absorbing (due to both intra and interband excitations), samples with strongly reduced thickness had to be prepared. The controlled chemical etching

Table 3.2: A list of Cd_3As_2 specimens used in our magneto-optical study. The bulk samples were used for reflectivity measurements and thin samples for transmission (p - plate, s - polished slab, b - bulk piece, T - transmission, R - reflectivity). The samples are denoted according to the grower and morphology. The natural crystallographic orientation of facets is (112). The Fermi level was estimated either from the zero-field optical conductivity, SdH oscillations or from the onset of the interband absorption with accuracy of 20 meV. The plasma edge was determined from reflectivity, splitting in the magnetic field or from the onset of the free-carrier absorption with precision of 5-10 meV. The values correspond to the temperature of 2-10 K.

Label	Type	Grower	Method	E_F [meV]	$\hbar\omega_p$ [meV]	Orientation
A-p	p	E. Arushanov	T	180	55	(112)
A-s	s	E. Arushanov	T	180	55	(112)
A-b	b	E. Arushanov	R	100	32	(112)
S-b	b	R. Sankar	R	250	68	(112)
C-b	b	R. J. Cava	R	200	55	(001)

in 5% Br-methanol solution for 1 min was tentatively tested [77, 78] on bulk pieces but with the negative result of pronounced damage and crumbling of the material. In contrast, a standard mechanical polishing allowed us to thin down bulk crystals down to the thickness of 50-100 μm , which appeared sufficient for transmission measurements in the spectral window limited, as explained in detail below, by the plasma energy (lower bound) and Fermi energy (upper bound). The samples were suspended on intrinsic Si substrates. The Al_2O_3 -based abrasive suspension with the grain size 3-6 μm was used together with a glass grinding disc. Plate-like samples were too fragile for any further mechanical processing. The final thickness was determined by an interferometric tomograph.

In general, the studied samples were found thermodynamically stable at ambient conditions. Nevertheless, a certain variation, most often, of the electron density (as grown Cd_3As_2 crystals typically show n-type conductivity) was observed upon thermal cycling between room and cryogenic temperatures. The instability is attributed to diffusion of Cd vacancies in a large cell (Fig. 3.1) leading probably to the formation of charged-depleted puddles in the surface layer that affects the observed optical response [50]. The phenomenon is dependent on the surface treatment (etching, polishing) and on the thermal annealing below 500 K which can eventually decrease the Fermi level from 250 meV to 120 meV as was documented in [76]. Such a decrease of carrier concentration is best visible on the redshift of the plasma edge in reflectivity experiments (Fig. 3.8). A detailed information about the samples used for our optical study is provided in Tab. 3.2.

3.5 Optical response at zero magnetic field

Reflectivity

The reflectance experiment (Fig. 3.7a) at zero field was performed with the use of standard Fourier transform spectroscopy. The reflectivity was measured in the energy

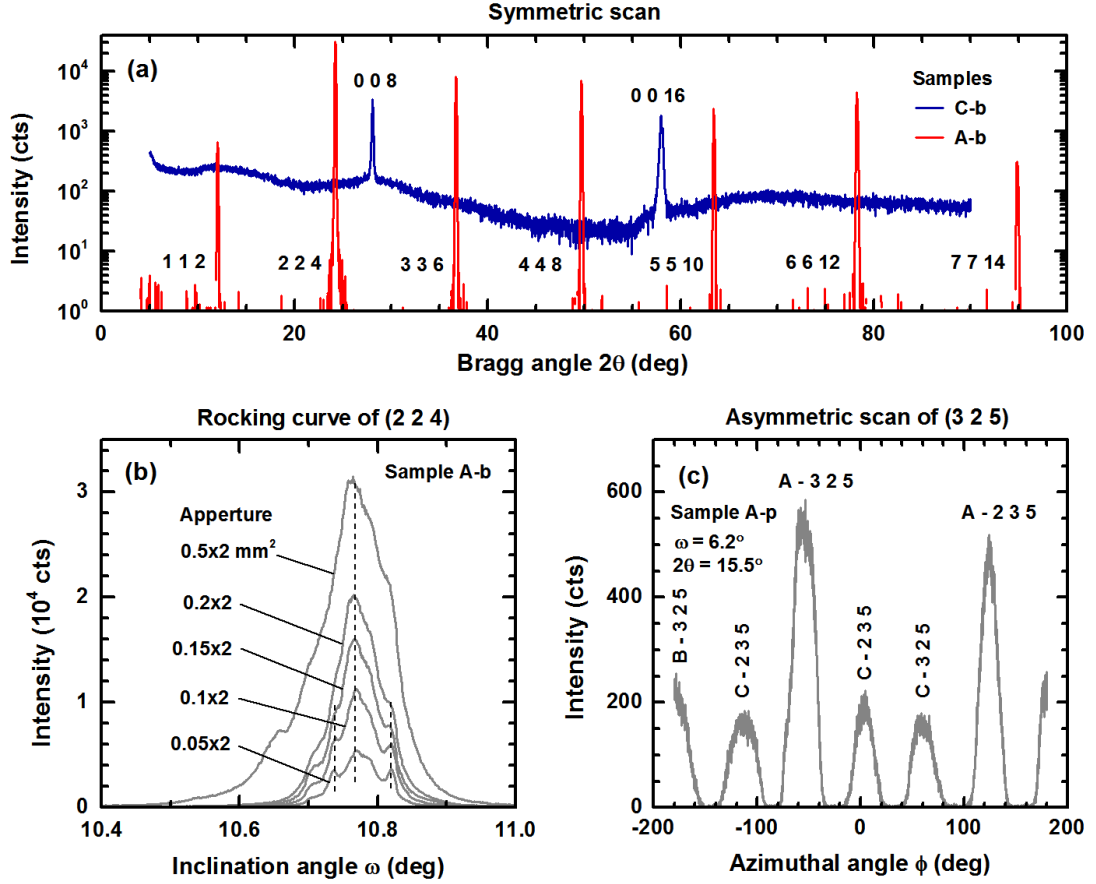


Figure 3.6: (a) A symmetric x-ray diffraction scan of the optical facets of the bulk crystal samples C-b and A-b. The diffraction peaks were assigned according to the space group $I4_1/acd$ and correspond to the higher harmonics of (001) and (112) poles respectively. (b) An omega-scan of the A-b sample for various apertures. The n -fold structure of the (224) pole reveals low-angle mosaicity of the crystal that actually constitutes of multiple grains vertically misaligned by 0.1-0.2 deg. The smallest diagram shows the presence of ≈ 5 -10 grains whose dimensions are typically in order of 0.1 mm. The polycrystalline nature of samples complicates the determination between the crystallographic (001) and (100) facets, since the supercell has dimensions very close to the integer a_0 -multiples of $Fm\bar{3}m$ group. (c) A phi-scan of the plate sample A-p in the coplanar geometry reveals a twinning into the three domains A, B, C mutually rotated by 120 deg. Ideally, the equivalent poles (325) and (235) should occur only twice in the interval of 180 deg.

range of 0.003-3 eV using an in-situ gold overcoating technique at 10 K. All reflectivity curves are dominated by a broad plasma edge. Its position moves for a different Fermi level and its breadth correlates with the variation of the electronic concentration in the explored samples. At low energies (5-30 meV) a series of relatively sharp phonon resonances is seen, with the strongest mode located at 18.5 meV.

Let us also note that the plasma edge reflectivity profiles exhibit in Cd_3As_2 some fine structure, well seen, e.g., for the sample A-p in (Fig. 3.7a) or in ref. [50]. Its origin is still not yet completely clarified, but most likely its appearance correlates with non-homogeneous distribution of electrons in the studied sample. This distribution may be either realized as a charge depleted layer on the surface and the plasma edge can be then simulated by a stacking of the layer on a more conductive half-space of a

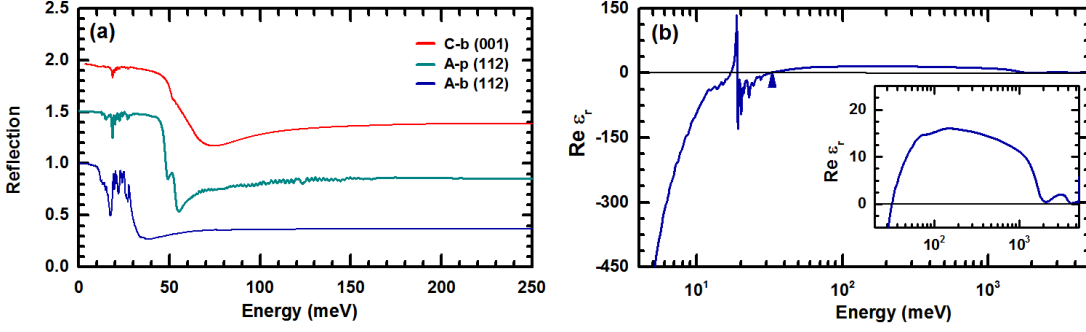


Figure 3.7: (a) Typical reflectance measured on Cd_3As_2 at zero-field with the dominating plasma edge and numerous phonon modes at low energies. The spectra are vertically displaced for clarity by factor 0.5. The plasma edge is shifted according to the actual carrier concentration and its breadth and splitting is mainly determined by the sharpness of the Fermi level and the presence of the depleted surface layer. (d) The dielectric function computed from the reflectivity using Kramers-Kronig relations diverges at low energies as it is typical for the Drude model. The intersection with $\text{Re } \varepsilon_r = 0$ defines the position of the plasma edge. At energies 0.1-1 eV the behaviour is less dramatic and can be described roughly by a stationary background value $\varepsilon_r^\infty = 14-15$.

bulk crystal [79]. Optionally, the observed behaviour can be explained assuming lateral variation of the carrier concentration in misaligned grains and the total response is obtained as an average from the multiple, slightly distinct, interfaces.

To receive a dielectric function and optical conductivity (Fig. 3.7b), the standard Kramers-Kronig analysis was employed using suitable extrapolations for the reflectance in the limit $\omega \rightarrow 0, \infty$. The high frequency phase was anchored using ellipsometric data [80]. The zero modes of the dielectric function $\text{Re } \varepsilon(\omega_p) = 0$, calculated as a conjugated quantity to the optical conductivity, defines a plasma frequency for a given carrier concentration more precisely than the broad minimum in the reflectivity (Fig. 3.7d).

Implications for a single 3D conical band on the overall optical response of the studied material may be shown on the mutual relation between the onset of the interband absorption (at E_F) and the position of the plasma edge in the reflectivity [81]

$$\omega_p = \sqrt{\alpha_s} \left(\frac{1}{(2\pi)^2} \frac{2}{3} \right)^{\frac{1}{3}} \left(\frac{32\pi}{3} \right)^{\frac{1}{6}} (\zeta_s \zeta_v)^{\frac{1}{2}} E_F, \quad (3.13)$$

where the fine-structure constant is introduced as $\alpha_s = e^2 / (4\pi \varepsilon_r^\infty \varepsilon_0 \hbar v)$ with a screening background dielectric constant ε_r^∞ and spin and valley degeneracy ζ_s, ζ_v , respectively. So, in a 3D conical structure the plasma frequency is directly proportional to the Fermi level $\hbar \omega_p = \gamma E_F$, unlike in a system with the parabolic bands where

$$\omega_p = \left(\frac{1}{(2\pi)^3} \frac{4\pi}{3} \frac{e^2}{\varepsilon_r^\infty \varepsilon_0 m_e} \right)^{\frac{1}{2}} (\zeta_s \zeta_v)^{\frac{1}{2}} \left(\frac{2m_e E_F}{\hbar^2} \right)^{\frac{3}{4}}. \quad (3.14)$$

The use of the expression (3.13) is dependent on the scenario of the band structure assumed for Cd_3As_2 . In the case of the Dirac model, the valley degeneracy is two (for the two Dirac cones localized at $\pm k_D$), whereas for the Kane-Bodnar model (with the negligible crystal field splitting $\delta \rightarrow 0$) the cone is just one at the Γ -point. The

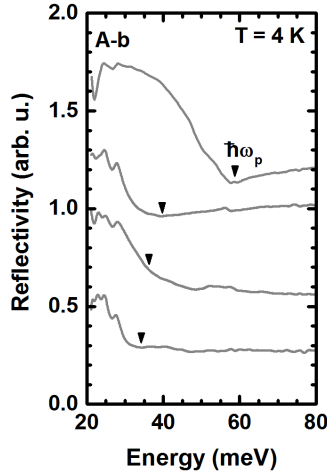


Figure 3.8: An illustration of the evolution of the plasma edge during several cooling cycles on the sample A-b. The effective carrier concentration dropped and consequently the plasma edge has shifted towards the low energies and became mixed with the phonon band. The reflectivity spectra (plotted with incrementing offset of 0.3) are not absolutely normalized due the different size of the sample vs. reference aperture.

background permittivity was chosen appropriately $\varepsilon_r^\infty \approx 15$ from the region remote enough from the position of the Fermi level ($E_F \approx 100 - 400$ meV) but before the onset of the transitions from the higher bands. The velocity parameter $v = 0.94 \times 10^6$ m/s is adopted from STM experiment [58] assuming roughly isotropic bands. Then, the scaling factor γ^{-1} from eq. (3.13) theoretically yields 2.8 for the Dirac and 4 for the Kane model respectively. These values will be later on put into the context with the deduced Fermi levels for the studied samples.

Transmission

Infrared experiments in the transmission configuration represent another possible and finally realized option in exploring of the magneto-optical response in Cd_3As_2 . In general, the analysis and interpretation of (magneto-)transmission data is more straightforward (for instance in the read-out of excitation energies) as compared to reflectivity measurements. On the other hand, transmission experiments may be only realized on transparent samples. The most convenient approach would be to perform the measurements on few microns thick epitaxial layers grown on a transparent substrate [82]. For bulk opaque crystals, one feasible option is to shine by an intense laser through a thin slab with a fixed energy above E_F , while the magnetic field is swept in order to tune the interband transitions, and to repeat this procedure for a series of samples with various doping [83] (or eventually to vary the laser energy for a single sample).

Another way is to profit from the transparency window which may be found in samples with intermediate thicknesses of tens of microns. Characteristically, such samples become transparent in the spectral region whose upper limit scales with the Fermi energy ($2E_F$ for an ideal Dirac cone or E_F for a Kane cone). At low energies, samples are transparent nearly down to the corresponding plasma energy $\hbar\omega_p$. The transmission and the reflectivity of a 80 μm -thick free-standing slab at $B = 0$ is depicted in the Fig. 3.9a. The small interference from the Fabry-Perot oscillations are visible between 100-160 meV for the index of refraction $n = 4$ that agrees with the dielectric function from the Fig. 3.7b.

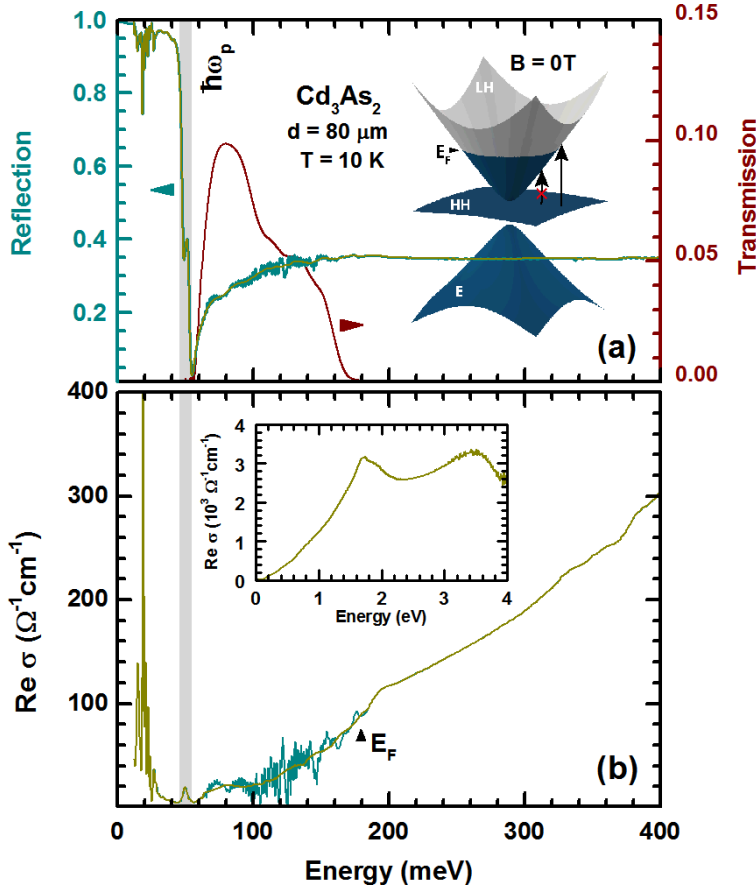


Figure 3.9: (a) Reflectivity and transmission at zero field of a thin self-standing plate with noticeable Fabry-Perot oscillations from 100-130 meV arising from the finite thickness. The plasma edge exhibits a fine structure in the absence of the field due to the spatial variations in the carrier density. (b) The optical conductivity smoothed from the Fabry-Perot oscillations reveals a gradual absorption in the transparent window, instead of a sharp steep onset due to the Pauli-blocking [84].

Optical conductivity

Optical conductivity, was calculated from the absolute reflectivity (Fig. 3.7) measured on the samples A-b, A-p, C-b (Fig. 3.10 and 3.9b). In the wide energy range from 3 meV to 5 eV several phenomena contribute to the total response of the dynamic conductivity. At low energies, it is the Drude peak whose magnitude depends on the carrier density and which defines the position of the plasma edge. Between 3-30 meV the optical conductivity is dominated by a rich spectrum of phonon modes. For heavily doped samples the tail of the Drude peak can extend into the phonon domain (as for the sample C-b). In the intermediate region of 50-500 meV, the response from the interband transitions to the conduction conical band appear. At high energies the transitions between the remote bands (higher or lower) become an important contribution. In general, we may conclude that the observed spectral dependence of the optical conductivity is in very good agreement with previously published data by Neubauer et al. [85]. Let us also note that the sum rules for the optical weight (= integrated optical conductivity), which are often applied in the analysis of the optical response of various solids, natu-

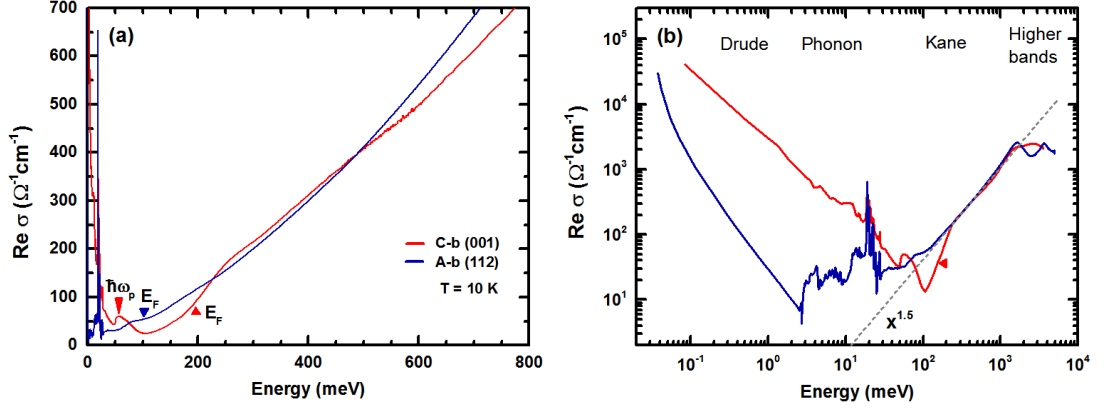


Figure 3.10: (a) A real part of the optical conductivity computed from the reflectivity using Kramers-Kronig relations depicts approximately a characteristic linear trend that can be locally fitted by a straight line. Marks help to indicate positions of the Fermi level (for the case of the Kane model) and the plasma edge. Data were acquired on the samples with two different crystal orientations revealing a weak anisotropy. The flat-to-cone excitations below the Fermi level are blocked in a system with homogeneous electron density. Strong spikes at low energies are caused by phonon modes. (b) Besides the interband (Kane-like) excitations within the cones and the flat band respectively, other contributions add to the total absorption at higher energies. At larger scale of 0.1-1.5 eV, the specific dependency deviates from the linear tendency by an upturn following approximately $E^{1.5}$ -law [70].

rally remain valid for the here studied material. They imply that the optical weight associated with the interband excitation (Pauli) blocked by the occupation effect is transferred to the optical weight due to free carrier absorption σ_D . Quantitatively, this may be expressed as

$$\int_0^\infty \sigma_D d\omega = \int_{\text{blocked}} \sigma_{\text{inter}} d\omega = \frac{\omega_p^2}{8\varepsilon_0\varepsilon_r^\infty}. \quad (3.15)$$

The plot in the Fig. 3.10b focuses on the intermediate range of energies and depicts three main characteristics. Firstly, the conductivity is in the region 200-600 meV fairly well linear in the energy which is the feature of the interband absorption that includes conical bands. Secondly, we may notice an onset of the absorption at 100 and 200 meV for the sample A-b and C-b respectively, below which the optical transitions are Pauli-blocked. Thirdly, the curves for the both samples overlap within 200-500 meV which signifies an approximate isotropy of the concerned bands. The onset of the absorption can be either attributed to $E_{\text{MB}} = 2E_F$ for the case of the Dirac structure with purely cone-to-cone transitions or to E_F for the Kane-like structure with flat-to-cone type dominant transitions, or eventually to $E_{\text{MB}} = E_F + |E_g|$ for the case of a small gap between the flat band and the upper cone. The fine structure visible at the plasma edge (observed in the reflectivity spectra) gives rise to a small tip-like feature in the optical conductivity at energy $\hbar\omega_p$ (red arrow).

In real systems, the Pauli blocking hardly corresponds to the theoretical Heaviside function $\theta(E - E_{\text{MB}})$ due to the strong disorder and charge carrier inhomogeneity. The related residual absorption around E_{MB} (in particular, apparent in the Fig. 3.9) may extend deeply toward low energies. The actual position of the Moss-Burstein edge can

be tentatively read out as an inflexion point of a relatively wide onset of 40 meV. One possibility to conveniently model the gradual rise of the absorption edge associated with the Pauli blocking and a way to replace the sharp Heavyside function offers a smooth function $\frac{1}{2} + \frac{1}{\pi} \text{atan}(E - E_F)/\Gamma$, where Γ accounts for broadening [85]. The broad Moss-Burstein edge makes the signature of Pauli-blocking hardly visible in the reflectivity curves, unlike in the optical conductivity, in a contrast to the earlier measurements of Jenkins [86], where the presence of E_{MB} was noticeable.

By analysing the optical conductivity due to interband excitations (specifically between 0.3-1.2 eV) in a greater detail, we find that it follows not exactly a linear, but instead superlinear, dependence, described by a power law $\text{Re} \sigma(E) \propto E^\alpha$ with the exponent $\alpha = 1.5$. This is in good agreement with conclusion of Neubauer et al. [85], implying only a slightly bigger value ($\alpha \approx 1.65$), probably due to the presence of the feature at 4 eV. To test the robustness of the applied Kramers-Kronig analysis [85], the reflectivity data was replaced by a free-electron term ω^{-4} for energies above 2 eV (removing the peak at 4 eV [48, 87, 88]) and the index dropped to $\alpha = 1.2$.

It is worth to note that for the doubled Dirac cone structure, there needs to exist a point when the both cones merge together and extend further as a single band (towards positive/negative higher energies). The distance between those two saddle points is referred as a Lifshitz gap E_{LG} . The related resonance excitation over the Lifshitz gap $\hbar\omega = E_{LG}$ can be observed only under the condition when the Fermi level lies between the both saddle points, i.e. $|E_F| < E_{LG}$ (assuming a full electron-hole symmetry) [86]. Our data does not evidence any feature that could resemble such a response for the given Fermi levels, except the maximum around 1.8 eV which was attributed according to the ref. [54] to the transitions at the M-point at the border of the BZ.

The slope of the quasi-linear interband absorption provides us with an estimate of the velocity parameter. As it was mentioned earlier, a pure 3D Dirac system only with cone-to-cone transitions has a dispersion $\text{Re} \sigma(E) = \frac{\zeta_v e^2 E}{4\pi v \hbar} \frac{1}{12}$ [12]. The straight-line fit within 200-600 meV gives a (unrealistically low) value of the velocity 0.05×10^6 m/s. For a gapless 3D Kane system, including cone-to-cone and flat-cone excitations, the dispersion reads $\text{Re} \sigma(E) = \frac{e^2 E}{4\pi v \hbar} (1 + \frac{1}{12})$. The absorption in the Kane system needs to be qualitatively stronger than for the Dirac model since it includes additional flat band that gives rise to the considerable density of states. The velocity extracted from the slope using the Kane formula is 0.3×10^6 m/s. However, in both cases the obtained value is significantly underestimated in respect to the result of STM [58] or parameters proposed by Bodnar [42]. In order to correct the discrepancy for the Kane model, we propose here to take into account the presence of the small gap between E and LH bands and the effect of the LH band flattening for large momenta due the influence from the SH band. The discrepancy for the alternative Dirac model is discussed in detail in the ref. [85] within the picture of self-energy correction.

The optical conductivity of an intrinsic system for the eight band Kane model

($E_g < 0$) can be expressed in the following manner [25, 70]

$$\text{Re } \sigma(E) = \frac{e^2}{4\pi\hbar v} \left[\left(1 - \frac{E_g}{2E}\right) \sqrt{E^2 - EE_g} + \theta(E - |E_g|) \frac{1}{16} \left(1 - \frac{E_g^2}{E^2}\right) \sqrt{E^2 - E_g^2} + \theta(E - \Delta) E \left(1 - \frac{\Delta}{E}\right)^2 \right]. \quad (3.16)$$

The first term describes the contribution of excitations between HH and LH bands. The second term, by order of magnitude weaker as compared to the first one, reflects optically-active transitions between E and LH bands. The third term includes excitations from the spin-split band (SH) to the conduction band. In an extrinsic system, a part of transitions from HH to LH in an energy range $E < E_F$ and from E to LH for $E < E_g + 2E_F$ are Pauli blocked which can be included in eq. (3.16) by an additional offset in Heaviside functions $\theta(x)$.

In contrast to gapless HgCdTe (another Kane-like system studied previously, see refs. [4, 20, 25]), the spin-orbit coupling is in Cd₃As₂ significantly weaker (0.4 eV versus 1 eV) and the presence of the SH band becomes relevant also for the optical response in the (middle) infrared spectral range. The close presence of the SH band causes significant flattening of the inverted E band that increases the joint density of states and upturns the conductivity. The whole situation of the E-SH band anti-crossing can be viewed in a simplified manner as an intersection of the deeply extending \tilde{E} band with the much flatter $\tilde{S}H$ band, if we assume that \tilde{E} consists of the E-branch for small k and SH-branch for large k , and in the similar way for the $\tilde{S}H$ band being constituted by the SH-branch for small k and E-branch for large k [70] (c.f. Fig. 3.2).

Let us note, however, that the limited validity of the formula (3.16) does not allow us to use it for more than a semi-quantitative description of the zero-field optical conductivity. This is because it neglects all the effects due to the tetragonal distortion of the Cd₃As₂ lattice, and even more importantly, it does not include interband absorption into the higher lying conduction band (present according to the STM/STM experiments already at energies close to 0.5 eV above the HH band).

3.6 Transport measurement

Magneto-transport measurements were used as an experimental method complementary to our magneto-optics. Such experiments provides us with information about electronic states in the immediate vicinity of the Fermi energy and thus may be directly compared to the results of cyclotron resonance absorption (discussed in the next sections). In the transport data, we primarily focused on effects due to the Shubnikov-de Hass oscillations, which appear as a direct consequence of emerging Landau level quantization, which yield the Fermi surface area A_F , and which, when followed as a function of temperature, also may give us very good estimate of the effective (cyclotron) mass.

The application of an external magnetic fields induces the quantization of electronic states into Landau levels with the corresponding area A_n , and consequently a profound

modulation of the density of states. At the semi-classical level, such quantization may be understood/expressed in terms of the Born-Sommerfeld quantization rule

$$A_n = \frac{2\pi e}{\hbar}(n + \xi)B, \quad (3.17)$$

where the phase factor ξ varies between 0 and $\frac{1}{2}$ in the dependence on a type of the dispersion [89]. As a consequence, a modulation of the dc-conductivity occurs periodically with the inverse value of the magnetic field

$$\delta \frac{1}{B} = \left(\frac{1}{B_n} - \frac{1}{B_{n+1}} \right) = B_f^{-1}, \quad (3.18)$$

when the extrema in the density of states crosses the Fermi level $A_F = A_n(B)$. The corresponding frequency (expressed in the units of Tesla) then directly tells us the area of the Fermi surface A_F .

The transport measurement was carried out on the sample C-b using the four-point method with B applied perpendicular to the polished facet of a rather irregular shape. The experiments carried out on the low-doped A-b sample did not bring conclusive results since the SdH signal revealed multiple frequencies corresponding to distinct carrier densities attributed to the charge inhomogeneity. The graph in Fig. 3.11a shows the large positive linear magneto-resistance R_{xx} with the superimposed SdH oscillations. When the background is subtracted, a clear SdH signal ΔR_{xx} is extracted with oscillations clearly visible above 2 T. The sequence (3.18) can be depicted with the use of the formula (3.17) as a linear line in a plot $\frac{1}{B_n}$ vs n

$$\frac{1}{B_n} = \frac{2\pi e}{\hbar A_F}(n + \xi) \quad (3.19)$$

or its frequency B_f can be directly extracted using Fourier transform of the SdH signal giving a single peak at $B_f = 37$ T (Fig. 3.11b).

The amplitude of SdH oscillations is a complex function of temperature, the separation of Landau levels and disorder (level broadening) present in the system. To describe the damping of oscillations with increasing temperature (when the thermal energy $\kappa_B T$ becomes comparable with LL spacing), the Lifshitz-Kosevich formula is often applied

$$\frac{\Delta\sigma_{xx}(B)}{\sigma_{xx}(0)} = \left(\frac{\hbar\omega_c}{2E_F} \right)^{\frac{1}{2}} \frac{\lambda}{\sinh \lambda} e^{-\lambda_D} \cos(l_B^2 A_F + \xi), \quad (3.20)$$

where $\lambda = 2\pi^2\kappa_B T/\hbar\omega_c$ and $\lambda_D = 2\pi^2\kappa_B T_D/\hbar\omega_c$ with the Dingle temperature $T_D = \hbar/2\pi\kappa_B\tau_Q$, quantum lifetime τ_Q and Boltzmann constant κ_B [60]. When the temperature is varied at a fixed field, the cyclotron mass can be extracted from the term $\lambda/\sinh \lambda$. This was done at $B = 6.6$ T yielding the mass $m_c = 0.036m_0$ (Fig. 3.11c).

The extracted cross section of the Fermi surface $A_F = \pi k_F^2$ from the eq. (3.19) $A_F(k_F) = 0.035 \text{ nm}^{-2}$ together with the cyclotron mass can provide a simple estimate of the velocity. Assuming that the probed band is conical (a fact consistent with the zero-field optics but also with results of other experimental techniques), for any carrier

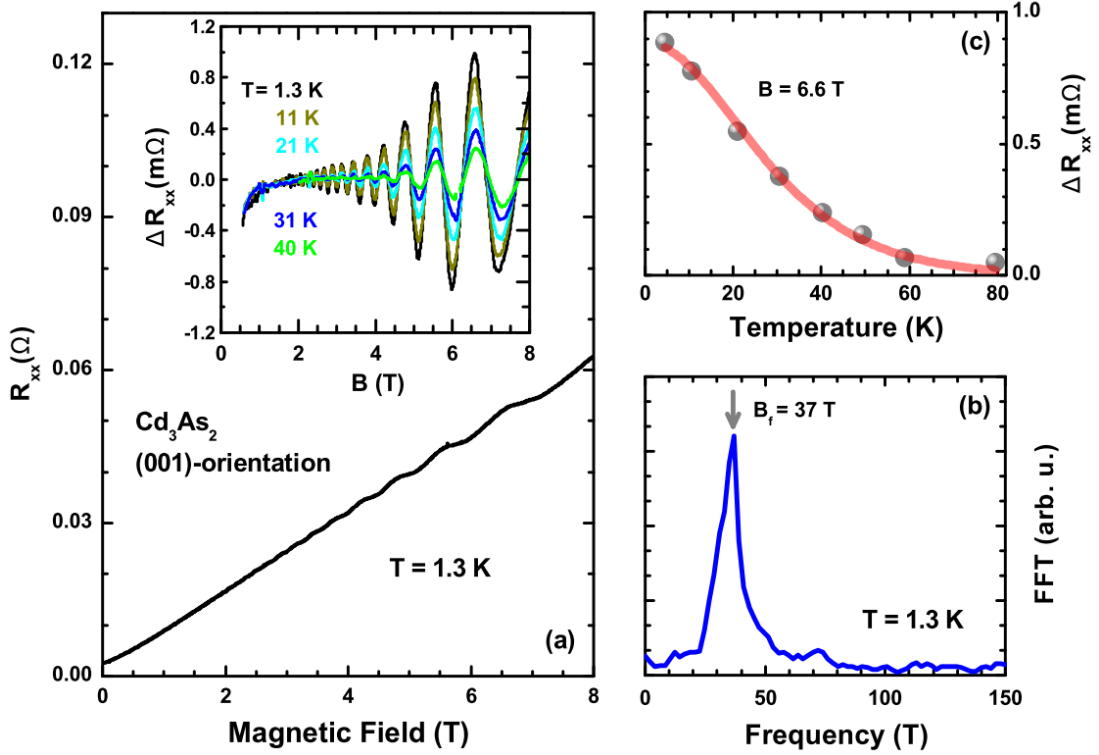


Figure 3.11: (a) Positive longitudinal magneto-resistance R_{xx} with the Shubnikov-de Haas oscillation measured on the sample C-b. To obtain a pure signal ΔR_{xx} , a nearly linear background needs to be subtracted (inset). (b) The fast Fourier transform of the signal reveals one dominant frequency peaked at $B_f = 37$ T. (c) The temperature dependence of ΔR_{xx} was measured in a maximum at $B = 6.6$ T and implies the electron effective mass $0.036m_0$ for a given E_F [70].

occupation represented by a certain Fermi level, the dispersion $E_F = \hbar v k_F$ is obeyed. The Fermi energy can be expressed also using the cyclotron mass as $E_F = m_c v^2$. When the both relations are combined, we arrive to an equation

$$v = \frac{\hbar}{m_c} \sqrt{\frac{A_F}{\pi}} \quad (3.21)$$

yielding the velocity $v = 10^6$ m/s that is close to the value from the STM study [58] or from the Bodnar's work [42]. Importantly, this rough estimate is also fairly close to the (more precise) value, $v = 0.94 \times 10^6$ m/s, which is later on deduced from our detail analysis of the CR response. With the knowledge of the velocity we can also estimate the Fermi level for the sample C-b as $E_F^{tr} \approx 235$ meV.

By fitting the suppression of SdH oscillations using eq. (3.20), the Dingle temperature can approximately determined as $T_D = 14$ K which provides a value of the quantum lifetime $\tau_Q = 10^{-13}$ s. In contrast, at zero field (or in classical regime at low magnetic fields) the scattering is described by a transport lifetime τ_{tr} contained in the electron mobility $\mu = e\tau_{tr}/m_e$. Its value can be obtained with the knowledge of the dc conductivity $\sigma_{xx}(0)$ and carrier density N_e as $\mu = \sigma/N_e e$ as $\tau_{tr} \sim 3 \times 10^{-12}$ s. The scattering rate τ_{tr} determines the boundary between the classical and quantum regime.

In low fields, an orbital motion of an electron is often interrupted by a scattering on an impurity or defect. If an electron undergoes such an event, its orbit is disconnected and the quantization is partially perturbed, however in a statistical average the trajectory resembles a classical circular motion. This situation is conditioned as $\omega_c \tau_{tr} < 1$ or in terms of mobility it can be formulated as $\mu B < 1$. The magnetic field necessary to reverse the inequality gives rise to a fully quantized regime when a period of the orbital motion is much smaller than the scattering rate.

In a broader context, Cd₃As₂ also crystallizes in a shape of needles with the direction $[1\bar{1}0]$ and exhibits exceptionally high mobility of orders of $10^6 \text{ cm}^2/\text{V}\cdot\text{s}$ together with the transport lifetimes $\tau_{tr} = 10^{-10} \text{ s}$, which are only comparable with the values on pure Bi, graphite or 2D electron gas in GaAs/AlGaAs. In comparison, the ordinary (multi-facet) bulky samples have typically $100\times$ lower mobility. One possible explanation suggests that the electron transport is realized through the channel voids $[1\bar{1}0]$ that appears specifically for P42/nmc [41]. Then, the scattering due to the lattice disorder does not greatly affects the forward drift velocity³. In addition, the quantum lifetime was found to be $\tau_Q = 10^{-13}\text{-}10^{-14} \text{ s}$ that gives an exceptional ratio $\tau_{tr}/\tau_Q \approx 10^4$ in comparison to the ≈ 10 for bulky samples.

Besides, the scattering rate can be also estimated from the width of the Drude peak Γ_D in the optical conductivity using a relation $\Gamma_D \tau_D = \hbar$ that returns for the case our sample C-b ($\Gamma_D \approx 1 \text{ meV}$) $\tau_D \approx 10^{-13} \text{ s}$ and a mean free path of $v\tau_D \approx 0.5 - 1 \mu\text{m}$.⁴

3.7 Magneto-optics in a classical regime

Splitting of the plasma edge

The presence of free charge carriers in a three-dimensional solid is typically manifested by an appearance of a plasma edge in the reflectance spectrum. When the magnetic field is applied and electrons undergo a periodic, cyclotron motion (with the classically defined cyclotron energy $\omega_c = eB/m_c$), the magneto-optical response of the system starts to differ when probed with radiation of the opposite circular polarizations. The corresponding dielectric function, using $\varepsilon = 1 + \frac{i\sigma}{\varepsilon_0\omega}$ for the Drude-type response (1.21), then reads [90]

$$\varepsilon_{\pm}(\omega) = \varepsilon_r^{\infty} \left(1 - \frac{\omega_p^2}{\omega(\omega \pm \omega_c) + i\frac{\Gamma}{\hbar}} \right). \quad (3.22)$$

For the cyclotron resonance active (CRA) mode of light, which shares the same sense of rotation with electrons, the position of the plasma edge increases with B and vice versa for the cyclotron resonance inactive (CRI) component. The dielectric function in a geometry of $B \parallel k$ needs to be treated separately.

In the lossless medium ($\Gamma \rightarrow 0$), the functions ε_{\pm} become purely real and the plasma edge is sharpened (Fig. 3.12a). The corners of the plasma edge with values 1, 1, 0 in

³In this regard, the Klein tunnelling is not considered.

⁴Under the assumption that the width of a Drude peak is not significantly sensitive to the carrier concentration.

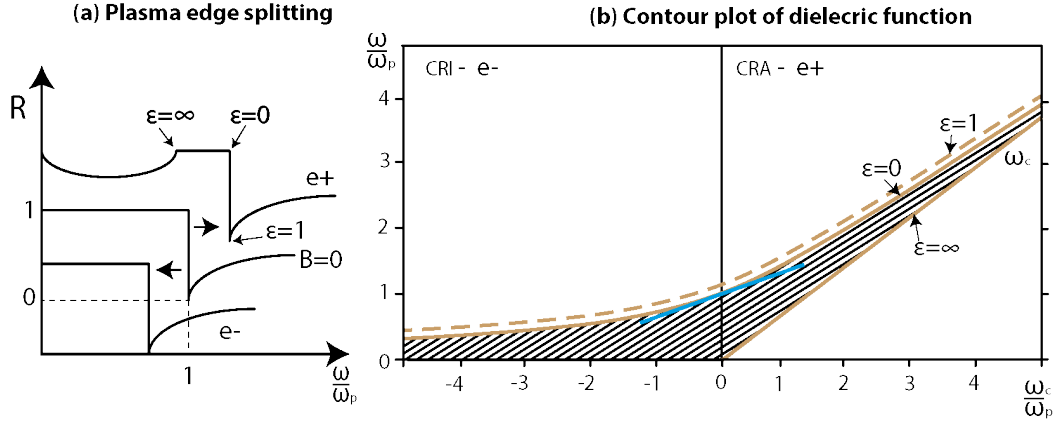


Figure 3.12: (a) Free carriers give rise to the plasma edge reflecting all incident light with the photon energies below. The edge splits into two components for the distinct polarization modes in the presence of the magnetic field. In the limit of the infinitely sharp edge, the reflectance can be effectively described by three principal points with characteristic values of the dielectric function. (b) The contour plot of ε_r provides an overview of the development of the both reflectivity components, where \mathbf{e}_+ (CRA) follows the cyclotron resonance and \mathbf{e}_- (CRI) converges to zero. The splitting is linear in the limit of $B \rightarrow 0$ (blue tangent).

a reflectivity curve correspond to the specific values ∞ , 1, 0 of the dielectric function, since the refraction index is $n = \sqrt{\varepsilon}$ and for the normal incidence of light the reflectivity is given as $R = |n - 1|^2 / |n + 1|^2$. The splitting of the plasma edge at the point $\varepsilon_{\pm} = 0$ is expressed as

$$\omega_{\pm} \approx \omega_p \pm \omega_c/2 + o(\omega_c^2) \text{ for } \omega_p \gg \omega_c. \quad (3.23)$$

From the observed splitting of the plasma edge, it is possible to deduce a cyclotron mass for a given plasma frequency on samples with various doping (our results and also those taken from literature, see Fig. 3.13a,b). For example, the samples C-b, A-b showed the splitting of 3 and 5 meV/T respectively, with corresponding cyclotron masses of 0.04 and $0.02m_0$. Notably, these our results are in very good agreement with those published previously by Gelten et al. [50] for the sample G-b AS57-2, see Fig. 3.13a,d. Knowing the velocity (e.g. from the transport measurements, STM, original Bodnar parameters), the energy-mass formula returns the Fermi levels 200 and 100 meV [70] (Fig. 3.13). The independent findings of the Fermi levels give us an indication that favours the realization of the Kane band structure rather than the Dirac. Firstly, they are fully consistent with the onsets of the absorption in the optical conductivity (Fig. 3.10) when $E_{MB} = E_F$ and secondly the factor γ^{-1} in the Das Sarma formula (3.13) returns a reasonable value of E_F for the plasma frequency of the C-b sample (For sample A-b both model gives comparable errors). Anyway, a conclusive evidence that we indeed deal with a Kane-like conical band and not with the Dirac cones will come from the high-field CR experiments discussed later on.

To get a better insight into the field-dependence of the plasma edge corresponding to CRA and CRI modes it is beneficial to represent ε_{\pm} in a contour plot for the important values in the frame of the reduced units of ω_c/ω_p and ω/ω_p (Fig. 3.12b). The CRA edge

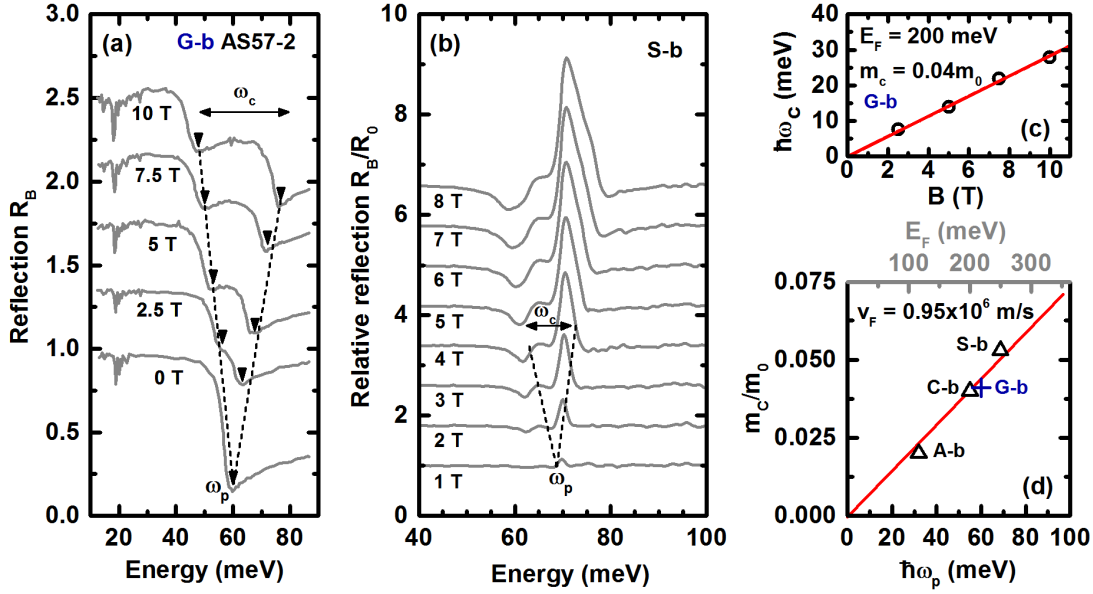


Figure 3.13: A strong splitting of the plasma edge was observed in the absolute reflectivity (a) on the sample G-b AS57-2 after [50] as well as in the relative reflectivity (b) on the sample S-b. The splitting $\hbar\omega_c$ is linear in small fields (eq. 3.23) and it could be read out as a distance between the minima (R_B) or from the inflexion points (R_B/R_0) respectively (c). The cyclotron mass, extracted from the splitting, is proportional to the cyclotron resonance and hence also proportional to the Fermi level through the parameter v , under the assumption of a conical conduction band (d).

asymptotically approaches the cyclotron resonance, while gradually varying its nature from the plasma edge to the dielectric resonance, or alternatively in the terms of the conductivity from the Drude peak to a Lorentzian function. At the same time the CRI component gradually approaches to the zero energy in the limit of high magnetic fields. The drop in the reflectivity at low photon energies for the σ_+ polarization allows a transversal helicon wave to propagate, when the rotating vector \mathbf{E} of the driving electric field is perpendicular to the magnetic field B , and the resulting electron current follows a circular trajectory [90]. The effect is sometimes called a dynamic manifestation of the classical Hall effect. In an experiment with unpolarized light (Fig. 3.14), where the both components \mathbf{e}_+ , \mathbf{e}_- are present at equal intensities, one can clearly observe the receding tendency of the CRA and CRI edges in the low magnetic field of the classical regime.

Free carrier Faraday rotation

Another configuration, in which we may probe the magneto-optical response of Cd_3As_2 , is the Faraday rotation experiment. The Faraday angle Θ_F is proportional to the sample thickness and to the difference of refraction indices n_{\pm} for the opposite circular polarizations of light and in a single passage approximation it reads

$$\Theta_F = \frac{\omega d}{2c_0}(n_+ - n_-), \quad (3.24)$$

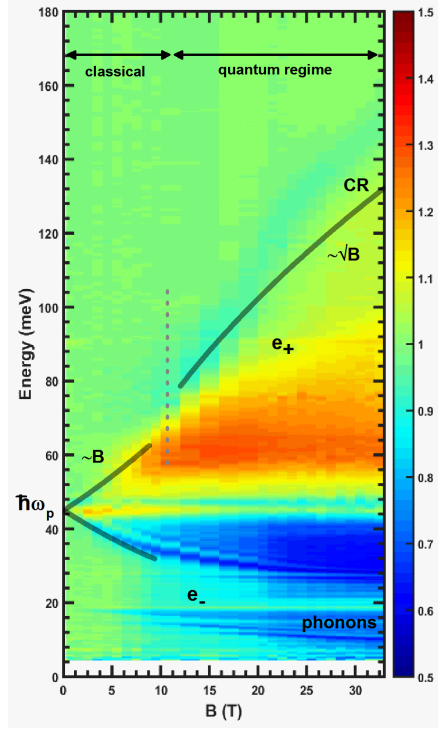


Figure 3.14: A false-colour map of the relative reflectivity R_B/R_0 shows the crossover from the classical to the quantum regime. In the low magnetic field the splitting of the plasma edge is linear in B . In the limit of high magnetic fields, the e_+ (CRA) mode develops into a cyclotron resonance in the quantum regime, i.e., into an excitation between well-resolved Landau levels with a characteristic \sqrt{B} -dependence, typical of all relativistic-like massless particles. The second e_- (CRI) approaches zero and become mixed with the phonon modes at low energies.

where d denotes the slab thickness. Focusing only on the contribution originating in the free charge response, the corresponding refraction indices may be calculated using eq. (3.22). In a high energy region ($\hbar\omega \gg \hbar\omega_c, \hbar\omega_p$), this implies the Faraday angle [90]

$$\Theta_F(\omega) = 2\pi e\hbar^3 \alpha_0 \frac{N_e}{m_e^2} \frac{Bd}{n_\omega} \frac{1}{(\hbar\omega)^2} \quad (3.25)$$

where N_e is electron concentration, m_e is effective electron mass, n_ω is refraction index at $B = 0$ at the probed photon energy $\hbar\omega$. The Faraday angle is linearly increasing in the magnetic field, scaling with the thickness and falling in frequency as quickly as $1/(\hbar\omega)^2$. When the effective mass is expressed using the well-know relativistic formula $E = m_e v^2$ and the carrier density is expressed via the corresponding Fermi energy in a conical band characterized by the velocity parameter v , we arrive at the formula with the absence of any effective mass

$$\Theta_F(\omega) = \frac{e\hbar^3 \alpha_0}{3\pi} E_F v \frac{Bd}{n_\omega} \frac{1}{(\hbar\omega)^2}. \quad (3.26)$$

The Verdet constant is received, when Θ_F is normalized per 1 T.cm, as it is plotted in Fig. 3.15 for the transparent window of the plate A-p assuming $E_F \approx 200$ meV and $v = 0.95 \times 10^6$ m/s.

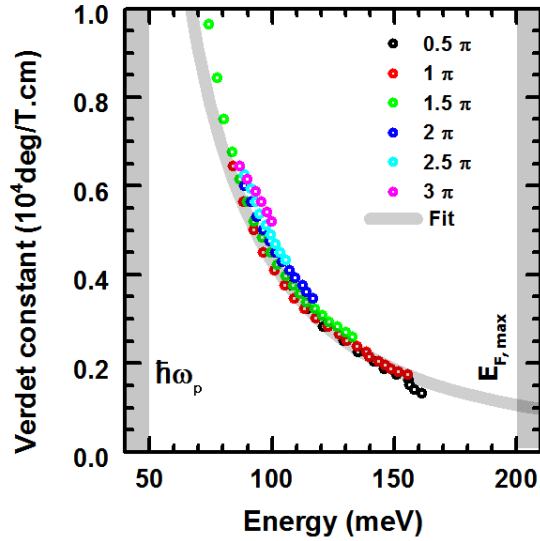


Figure 3.15: The Verdet constant was reconstructed in the discrete values from the Faraday angle inside a semi-transparent window enclosed by the plasma frequency and Fermi level. The fitting curve represents a free-carrier rotation with the use of $E_F = m_c v^2$.

3.8 Cyclotron resonance in a quantum regime

The crossover from the quasi-classical regime ($\mu B \leq 1$ or alternatively $\omega_c \tau_{tr} \leq 1$) to the quantum regime ($\mu B \gg 1$ and $\omega_c \tau_{tr} \gg 1$) with well-resolved Landau levels, manifested in the magneto-transport data by the appearance of pronounced SdH oscillations, may be also traced in the magneto-optical response of the system. At low magnetic fields, the cyclotron motion of electrons implies the splitting of the plasma edge that is equal to the classically defined cyclotron energy $\hbar\omega_c = \hbar eB/m$. Notably, this energy is always linear in B and the nature of charge carriers (massive or massless) is reflected only in the energy dependence of the cyclotron mass (Fig. 3.13d). When the magnetic field is increased, the quantum regime is approached and Landau levels start to form. The optical response, namely the CRA/CRI active modes of the split plasma edge, may be viewed as coupled modes of a single-particle (cyclotron resonance) excitation (between adjacent Landau levels and across the Fermi energy) with the collective (plasmonic) excitation in the classical plasma. In the limit of high magnetic fields, when $\omega_c \gg \omega_p$, the response becomes dominated by the pronounced CRA mode, which can be associated with a pure single-particle cyclotron resonance excitation. The energy and characteristic field dependence of this mode may provide us with a useful insight into the electronic band structure of the explored system. This is the way, we could have found decisive arguments which favour the Kane/Bodnar model over the widely accepted Dirac-like description.

The magneto-optical response, namely magneto-reflectivity, was probed in a broad range of magnetic fields, from the quasi-classical regime up to the quantum limit on samples C-b and A-b. The relative magneto-reflectivity spectra taken at high fields were dominated by a single cyclotron resonance mode (Fig. 3.16), having nearly the same position for the both samples (with the different crystallographic orientations) and thus pointing towards fairly high isotropy of electronic bands in Cd_3As_2 . The position of these cyclotron resonance modes (read-out as corresponding inflection points in the reflectivity spectra) follow a well-defined \sqrt{B} -dependence, which clearly indicate the

presence of massless electrons.

The CR mode of the A-b sample emerges below 10 T and remains present up to the highest magnetic field applied, 33 T. In any system of either Dirac or Kane massless electrons, this is only possible when the quantum limit is approached and electrons are excited from the lowest LL in the conduction band. This is because the fundamental level cannot be, in contrast to higher LLs, depopulated with the increasing B .

To test, whether 3D Dirac electrons may be at the origin of the observed (isotropic) CR response, let us consider their LL spectrum,

$$E_{\text{Dirac}} = \pm v \sqrt{2e\hbar B n + \hbar^2 k^2}. \quad (3.27)$$

It comprises specific $n = 0$ LLs dispersing linearly with the momentum k along the magnetic field. Each CR mode between adjacent LLs with $n \geq 1$ is characterized by a singularity in the joint density of states due to the band extrema at $k = 0$, and therefore, by a strict \sqrt{B} -dependence (Fig. 1.5b). For the fundamental CR mode, which is the only active mode in the quantum limit and corresponds to excitations from the $n = 0^{\uparrow, \downarrow}$ levels, such a singularity is missing because of the linear dispersion in k (Fig. 3.17c). Its only characteristic spectral feature is the low-energy absorption edge at

$$L_{0 \rightarrow 1} = \sqrt{v^2 2e\hbar B + E_F^2} - E_F. \quad (3.28)$$

Importantly, this low-energy edge does not follow the \sqrt{B} -dependence, and, moreover, its position depends on E_F . This is in clear disagreement with our experimental findings, where the fundamental CR lines show a nearly perfect \sqrt{B} -dependence and have almost the same position for the both studied samples (despite significantly different E_F). The picture of 3D Dirac electrons thus does not match our data. We illustrate this in the Fig. 3.16 by plotting the $L_{0 \rightarrow 1}$ energy for the two selected zero-field Fermi levels $E_{F0} = 100$ and 200 meV. The field dependence of E_F was calculated supposing a 3D Dirac LL spectrum. The plotted $L_{0 \rightarrow 1}$ curves clearly deviate from the \sqrt{B} -dependence and thus cannot be used for fitting by any variation of the velocity parameter (fixed at 10^6 m/s in the plot).

In contrast, the $n = 0$ Landau levels dispersing linearly in k are absent in systems with Kane electrons,

$$E_{\text{Kane}} = \kappa v \sqrt{e\hbar B (2n - 1 + \sigma) + \hbar^2 k^2}, \quad (3.29)$$

where $\kappa = -1, 0, 1$ and $\sigma = \pm \frac{1}{2}$. As a result, all CR modes of Landau-quantized massless Kane electrons, including the fundamental one, follow a \sqrt{B} -dependence. Notably, in an electron-doped system, the Fermi energy never drops below the $n = 1^{\downarrow}$ level and the fundamental mode thus corresponds to $1^{\downarrow} \rightarrow 2^{\downarrow}$ (Fig. 3.18) with energy

$$L_{1^{\downarrow} \rightarrow 2^{\downarrow}} = v \left(\sqrt{\frac{5}{2} e\hbar B + (\hbar k_B)^2} - \sqrt{\frac{1}{2} e\hbar B + (\hbar k_B)^2} \right), \quad (3.30)$$

where k_B is an out-of-plane momentum in the direction of the magnetic field.

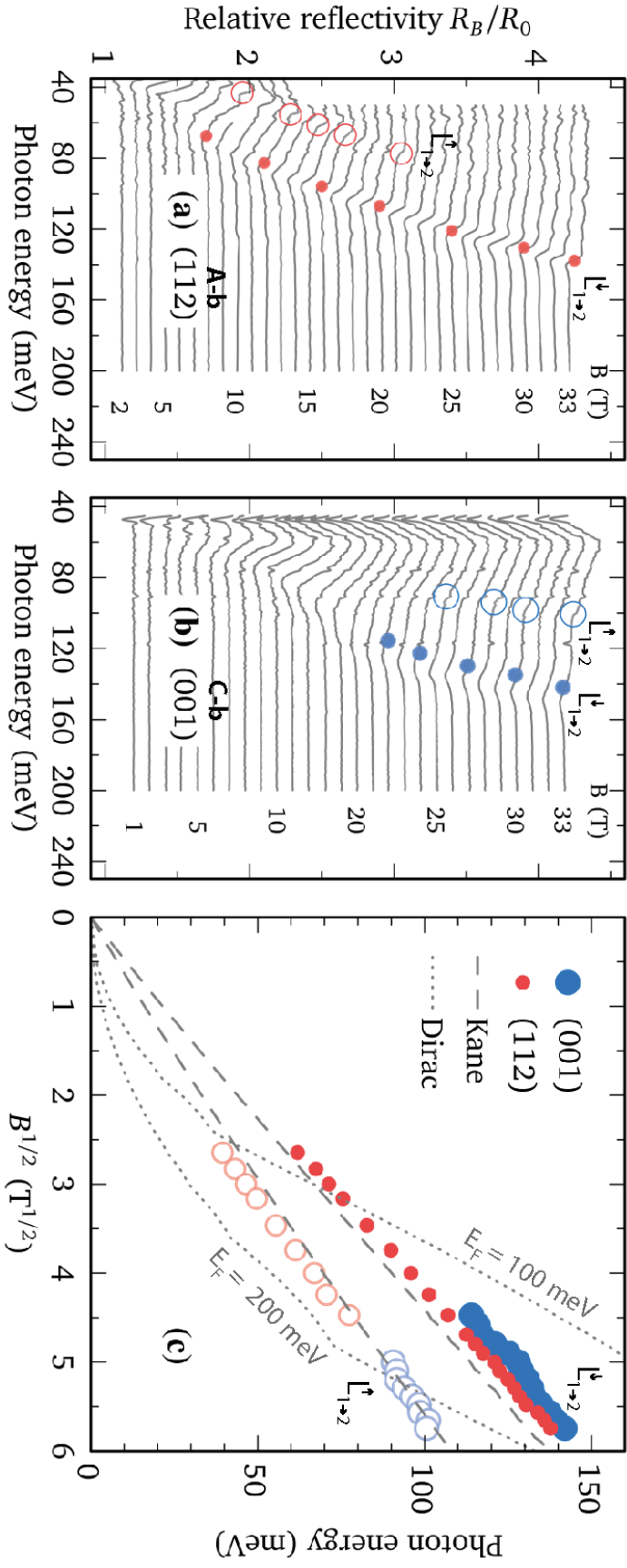


Figure 3.16: Relative reflectance was measured at $T = 1.8$ K in the magnetic field for (112) and (001)-oriented samples respectively (a), (b). The strong CR was assigned as a transition $L_{0 \rightarrow 1}^{\downarrow}$ in an isotropic Kane model. The weak satellite at low energies is an intraband resonance $L_{0 \rightarrow 1}^{\uparrow}$ that precedes the quantum regime which was reached for the sample A-b with $E_F \approx 100$ meV, but not yet for C-b with $E_F = 200$ meV. The \sqrt{B} -dependence of the both CR modes is shown in the part (c), together with the theoretical curves based on the Dirac (dotted) and gapless Kane (dashed) models. The former curves were calculated for the velocity 10^6 m/s and the zero-field Fermi energies $E_{F0} = 100$ and 200 meV. The kinks appear due to field dependence of E_F [70].

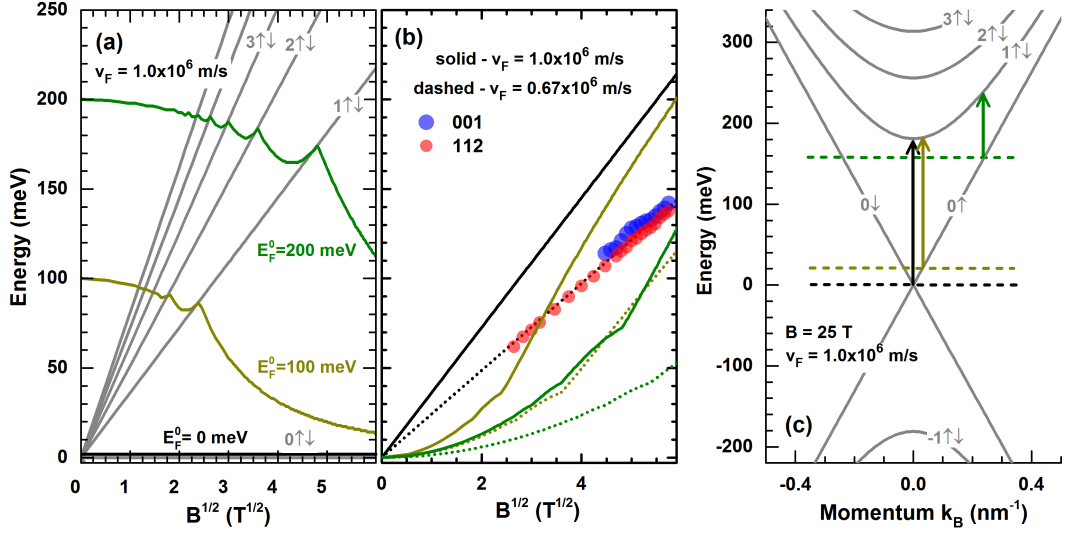


Figure 3.17: (a) The development of the Fermi energy in the magnetic field for a Dirac system and initial values $E_{F0} = 0, 100, 200$ meV. Approximately, the Fermi level decreases linearly until the first level is emptied then E_F falls as $\sim B^{-1}$. (b) The velocity was adjusted as $v = 0.67 \times 10^6$ m/s in order to make $L_{0 \rightarrow 1}$ transition matching the datapoints and to 1×10^6 m/s in order to agree with the older experiments [42, 58]. It is assumed that A-b sample already reached the quantum limit and its CR disperses genuinely as \sqrt{B} . (c) For the case of the sample C-b with $E_{F0} = 200$ meV, the k_z -term of the out-of-plane dispersion effectively lowers the CR energy that takes place at $k_z \neq 0$, as for example at the fixed field of 25 T. But, there we have arrived to the contradiction with \sqrt{B} -dependence observed for that sample which makes the Dirac model improbable to be realized [70].

After these qualitative arguments, we now proceed with the quantitative analysis of our data, using the simplest gapless Kane model. This model implies only two material parameters, v and Δ . The velocity parameter was taken after Bodnar [42] and STM/STS measurements [58] determined for a single conical band at the Γ -point. The strength of the spin-orbit coupling was set to $\Delta = 400$ meV, the value known for InAs. This choice is justified by the simple fact that the strength of the spin-orbit interaction in most semiconductors is predominantly governed by the anion atom, which in this case is arsenic. Lower values might also be considered (e.g., $\Delta = 270$ meV [42]), at the expense of a slightly increased electron-hole asymmetry in the model. How the choice of the Δ -parameter influences the fit is illustrated in the Fig. 3.19.

Apart the main resonance mode, another less pronounced feature could be noticed in the data at lower energies (open circles in Fig 3.16). Its positions in spectra were systematically reproduced and hence identified as a second lowest intraband LL transition $L_{1 \rightarrow 2}^\uparrow$ (Fig. 3.18) with energy

$$L_{1 \rightarrow 2}^\uparrow = v \left(\sqrt{\frac{7}{2} e \hbar B + (\hbar k_B)^2} - \sqrt{\frac{3}{2} e \hbar B + (\hbar k_B)^2} \right). \quad (3.31)$$

Its form is less pronounced for the C-b sample, that was measured with a smaller aperture, and therefore more affected by the background reflection disturbing the contrast. The theoretical positions of the two CR modes $L_{1 \rightarrow 2}^\uparrow$ and $L_{1 \rightarrow 2}^\downarrow$, expected to be active in the vicinity of the quantum limit of massless Kane electrons, are plotted along the

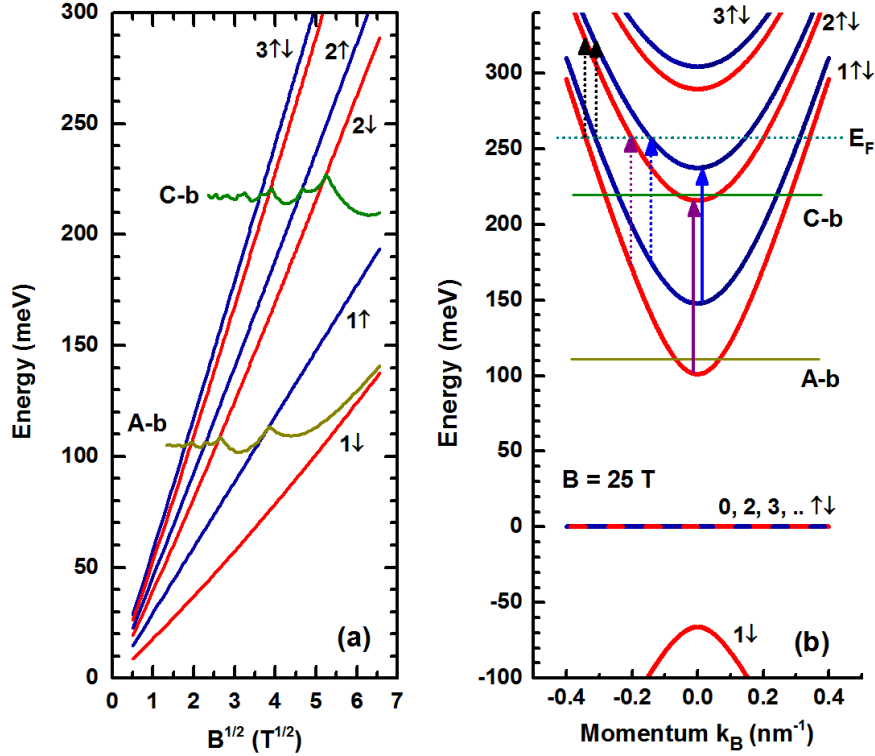


Figure 3.18: (a) A simulation of the Fermi level evolution due to the increasing LL degeneracy caused by the magnetic field. Samples A-b and C-b have the initial levels 100 and 200 meV respectively. (b) The out-of-plane dispersion of the Landau levels for the fixed magnetic field of $B = 25$ T. For a high Fermi level E_F , the position of the cyclotron resonance modes $1^\uparrow \rightarrow 2^\uparrow$ and $1^\downarrow \rightarrow 2^\downarrow$ depends on the occupation of the final level. The transitions take place away from $k_B = 0$ due to the Pauli blocking and are dispersed within the high and low energy tails (dotted arrows). Once the levels $2^{\downarrow,\uparrow}$ become depleted, the transitions are mainly localized to $k_B = 0$, where the density of states has a singularity.

data.

Kane model fits well the experimental points for the dominant CR line as well as for the weaker satellite, using only the above estimates for v and Δ , introducing no additional fitting parameters. Consistently with this picture, the satellite line is gradually suppressed with B in the lower-doped C-b sample, when the system enters the quantum limit. Although the Kane model explains our data fairly well, due to the tetragonal nature of Cd_3As_2 this model cannot be valid down to arbitrarily low energies. The Bodnar model (including small gap E_g and splitting δ) gives principally similar behaviour as the Kane for high energies. Its usability and parameter estimation will be the discussed in the next section.

The last remark will be devoted to an anisotropy of the velocity between (001) and (112)-orientations of the conduction band. The Kane model model assumes a general isotropic velocity parameter (or interband matrix element P). In contrast, the Bodnar model takes into account the anisotropy at higher energies through parallel and perpendicular velocities ($v_\perp \neq v_\parallel$) in respect to the z -axis (eq. (3.3)). However, it will turn out that in-plane and out-of-plane values must be similar within 10% on the basis of the CR analysis.

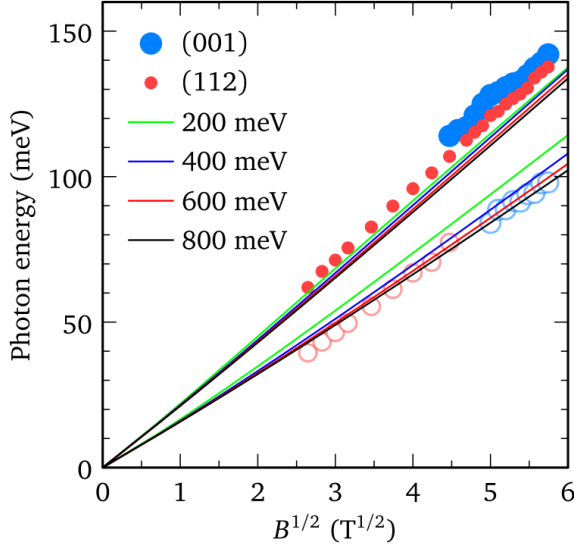


Figure 3.19: The effect of various strengths of the spin-orbit coupling Δ on the CR position according to the Kane model and its comparison with magneto-reflectivity data [70].

For an uniaxially anisotropic material an electron in the magnetic field orbits along an ellipsis with the main axes r_α, r_β in the coordinate space and with p_α, p_β in the momentum space that follow the proportion $\frac{p_\alpha}{p_\beta} = \frac{v_\alpha}{v_\beta}$. The product of momenta $\pi k_\alpha k_\beta$ defines the area of the ellipsis in the reciprocal space. Using the Bohr-Sommerfeld rule (3.17), we find the energies of Landau levels within an anisotropic conical band as $E = \sqrt{v_\alpha v_\beta 2\hbar e B (n + \zeta) + v_\gamma (\hbar k_\gamma)^2}$. In the limit of $k_\gamma = 0$, the cyclotron resonance is proportional to the factor $\sqrt{v_\alpha v_\beta}$. When the vector B points in $(001)^\top$ for the (001)-orientation the product of velocities $\sqrt{v_\alpha v_\beta}$ gives trivially v_\perp respecting the principal axes x_\perp, x_\parallel of the rotational ellipsoid of anisotropy. Let us now denote an arbitrarily revolved coordinate system as $x_\alpha, x_\beta, x_\gamma$. Then, the second case of the (112)-orientation with $\frac{1}{\sqrt{3}}(111)^\top$ along x_γ direction has the main axes $v_\alpha = v_\perp, v_\beta = \sqrt{(v_\perp^2 + 2v_\parallel^2)}/3$. From the ratio $\alpha = \omega_c^{(001)}/\omega_c^{(112)}$ of the experimentally obtained CR lines $L_{1 \rightarrow 2}^\downarrow$, one can express the ratio of the principal velocities as

$$\frac{v_\perp}{v_\parallel} = \sqrt{\frac{3 - \alpha^4}{2\alpha^4}} \approx 0.9. \quad (3.32)$$

3.9 Interband transitions in a quantum regime

As explained in the former section 3.7, it is possible to observe inter-Landau level transitions in the transmission configuration in the semi-transparent window, defined by occupation effects (Pauli blocking), due to the Fermi level broadening and related charge carrier inhomogeneities observed on the plate sample A-p. In this window, we have observed a series of excitations, which follow a nearly perfect \sqrt{B} -dependence (Fig. 3.20a).

A simple analysis based on the use of the Bohr-Sommerfeld quantization condition

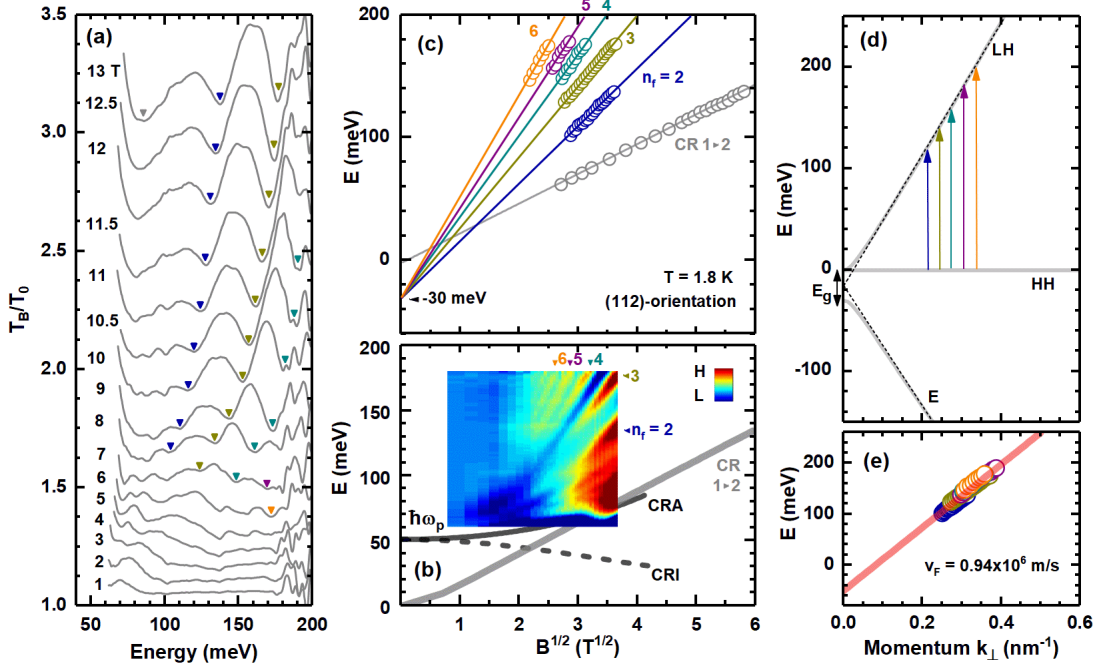


Figure 3.20: (a) Relative magneto-transmission spectra reveal in the semi-transparent window three pronounced Landau level transitions and two weaker lines at higher energies that are able to be traced from 3 T (orange, purple). (b) At low energies an onset of the cyclotron resonance CR begins to be visible in the absorption false-colour map as it is being formed from the active component (CRA) of the split plasma edge. (c) The positions of the interband transitions obey a \sqrt{B} -dependency, in the same fashion as was measured earlier in the reflectivity for the CR at the high magnetic field [70], and thus confirm the conical nature of the conduction band, while a (potential) bandgap needs to stay relatively small. (d) If the crystal field splitting is neglected in the Bodnar model, the directions (001) and (112) of the momentum become equivalent and the extrapolation of the transitions to the zero field gives an intercept identified as an inverted halfgap ≈ -30 meV, since the heavy hole band is ideally flat. (e) Inter-Landau level transitions collapse on a single line that can be calibrated in the momentum space using the Bohr-Sommerfeld relation. The line coincides with a conical energy dispersion $E = v\hbar k_{\perp}$ calculated using the velocity 0.94×10^6 m/s.

(3.17) (similar to one used for quantum oscillations in an STM study [58] or for magneto-optical oscillations in the ref. [83]) allows us to perform an elementary line assignment and determine/limit the band parameters. The procedure can be applied in a rough approximative picture for the Kane as well as for the Dirac model. By concluding the realization of the Kane massless electrons in Cd_3As_2 from the CR behaviour observed in magneto-reflectivity to be suitable for our description (and thus more probable than the Dirac), we further assume its validity.

In addition, we also assume the nature of the interband excitations to take place within the HH and LH bands, since their absorption weight prevails over the excitations between the E and LH bands.

Both conditions will be a-posteriori confirmed by the sake of a reasonable value of the velocity parameter consistent with our previous optical experiments. The optical transitions between the initial Landau levels $n_f \pm 1$ of an ideally flat HH band to the final level n_f in the conical conduction LH band can be understood as the excitations between the electron orbits $A_n = \frac{2\pi eB}{\hbar}(n + \frac{1}{2})$, whose area is in the reciprocal space

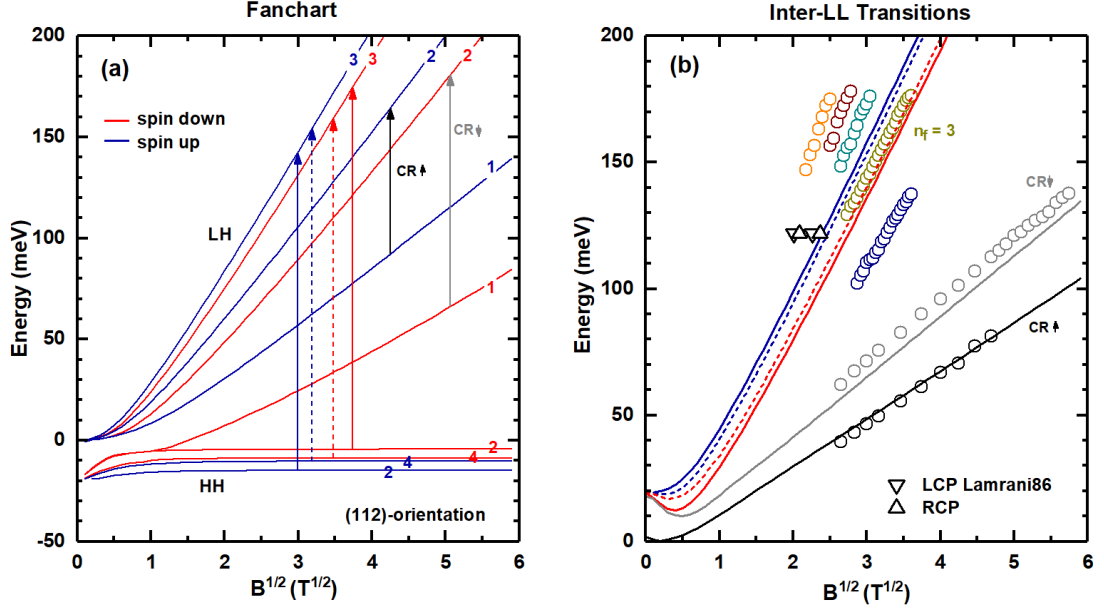


Figure 3.21: In the Bodnar model, a crystal field splitting leads in the flat band to the small dispersion of the Landau levels that forms a quasi-continuum of Landau levels in comparison to the Kane model, where all the heavy hole levels were degenerated and identically zero. So, the degeneracy of the paired transitions $2^\uparrow \rightarrow 3^\uparrow$, $4^\uparrow \rightarrow 3^\uparrow$ or $2^\downarrow \rightarrow 3^\downarrow$, $4^\downarrow \rightarrow 3^\downarrow$ respectively can be explained, when the splitting is small and the both transitions overlap due to the final linewidth (a). In the rough approximation the spin splitting between 3^\uparrow , 3^\downarrow can be also neglected and the both spin sets can be viewed as degenerated for the higher Landau indices in the conduction band, where the LH fanchart becomes dense. In this picture, all the concerned transitions to the final Landau level $n_f = 3$ merge together within the experimental error of the datapoints (b). The same arguments hold for the other interband transitions $n > 3$. However, the procedure does not apply for the cyclotron resonance modes observed in reflectivity [70], where the spin splitting remains considerable and needs to be taken into account. In this simulation, the gap was set to -60 meV and CF as 30 meV.

represented as $A_n = \pi k_{\perp, n}^2$ (Fig. 3.20d). By relating the later expressions, the photon energy $E_{\hbar\omega}$ and momentum k_{\perp, n_f} can be associated together giving a single $E_{\hbar\omega}-k_{\perp}$ dispersion (in limit of $B \rightarrow 0$) when normalized with respect to n_f (Fig. 3.20e). The proper choice of n_f ensures collapse of all excitations on a single line whose slope is attributed to the velocity ($E = v\hbar k_{\perp, n_f}$). The obtained velocity, $v \approx 0.94 \times 10^6$ m/s, is in full agreement with the previous results. In contrary, if the observed excitations were identified as inter-cone transitions, the velocity would be a half of this value (assuming full electron-hole symmetry).

In this regard, we suppose that the interband transitions follow the selection rules $n \pm 1 \rightarrow n$ valid for a gapless Kane model in a dipole approximation. They all appear theoretically at the comparable relative intensities as explained in more detail in the appendix 7. The ansatz for the line identification was obtained under an assumption that the transitions for the fixed final Landau level n_f are two-fold degenerate (in lower fields) with respect to the initial level $n_f \pm 1$ and in addition two-fold degenerate due to the spin (Fig. 3.21a). The supporting argument is provided by the magneto-optical data from the ref. [83] measured with circularly polarized light for a fixed laser line with energy 120 meV. A narrow splitting was observed between the transitions $n_f = 3^\uparrow$

and $n_f = 3^\downarrow$ (or $n_f = 4^\uparrow$ and $n_f = 4^\downarrow$ respectively, as they were ascribed) for the two distinct polarizations σ^+ and σ^- (Fig. 3.21b). This can be explained by two scenarios. Either a half of transitions is suppressed for each polarization with a realization of just one selection rule $\Delta n = 1$ or $\Delta n = -1$. The second possibility is that the transition $L_{n-1 \rightarrow n}^\uparrow$ overlaps with $L_{n-1 \rightarrow n}^\downarrow$ (and analogically for the situation of $\Delta n = -1$). In this simplified picture, the Zeeman splitting of LLs in the conduction band is neglected and an average position is taken instead. The plausibility of such an approach becomes more clear for higher LL indices, when the LL spacing can be compared with a finite linewidth of the transition.

We may also notice that the observed lines, besides the property of genuine \sqrt{B} -dependence, extrapolate to a common negative intercept ($q \approx -(30-40)$ meV) for B approaching to zero (regardless the line assignment). Such behaviour is another indication that we probe Kane-like conical band and not a pair of Dirac cones. In the latter case, such a well-defined negative intercept could be only present for the velocity parameter $v(k)$ increasing (unrealistically) with the momentum. In contrast, within the standard Kane model, this intercept is explained due to small negative gap present in the system (similarly to HgTe).

The flat-to-cone transition $L_{n\pm 1 \rightarrow n}^\sigma$, with $\sigma = \uparrow, \downarrow$ denoting the spin set, is directly equal to the energy of an appropriate Landau level of the conduction band, i.e. $L_{n\pm 1 \rightarrow n}^\sigma = E_n^\sigma$, defined by the formula [25]

$$E_n^\sigma = \frac{E_g}{2} + \sqrt{\frac{E_g^2}{4} + \frac{\hbar^2 v^2}{l_B^2} (2n - 1 + \sigma) + (\hbar v k_B)^2}. \quad (3.33)$$

The flat band is considered to be constant and pinned to zero energy. In the limit of high magnetic fields the term $\frac{E_g^2}{4}$ can be neglected as well as the term $(\hbar v k_B)^2$ (a pure \sqrt{B} -dependence observed signifying $k_B = 0$). Then, the extrapolation to zero field points to the common intersection $q = \frac{E_g}{2}$ regardless of the final LL index n_f . This implies that the gap has approximately a value of $-(60-80)$ meV (Fig. 3.22). Vice versa, a positive intercept would imply a positive gap. Additionally, a \sqrt{B} -dependence of the cyclotron resonance $L_{1 \rightarrow 2}^\downarrow$ in a wide range of field tells us that the negative E_g needs to be significantly smaller as compared to the energy scale of the observed excitations (i.e. less than 100 meV) to keep the LH and E bands nearly conical [84].

The analysis can be extended toward the Bodnar model (i.e. taking into account the crystal field splitting). Then, the band structure is no longer isotropic, which is best manifested by the corrugation of the (originally completely flat) HH band. This is illustrated in Fig. 3.23a,c, where the LH, HH and E bands have been plotted for two crystallographic directions, which are perpendicular to the magnetic field (applied along the [112] direction) and also to each other. These directions have been chosen as extremal to visualize the full width of the flat band induced by non-zero δ . For relatively small δ , the corrugation of the flat band remains relatively weak, but the flat band shifts by the average value of $\delta/3$. This implies an approximate offset of flat-to-cone inter-LL excitations: $E_g/2 + \delta/3$. In addition, the presence of the crystal field splitting lifts the flat band degeneracy (and thus the degeneracy among initial

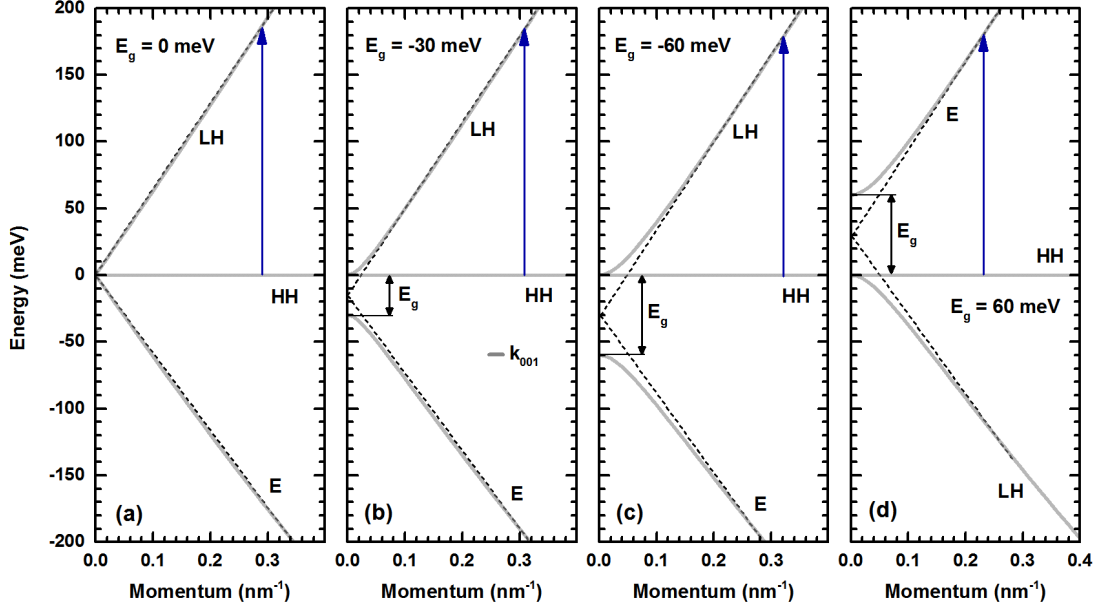


Figure 3.22: In the Kane model with the inverted band gap ($E_g < 0$) the electron band is exchanged with the light-hole band. The opening of the gap affects mainly low energies ($E = \frac{E_g}{2} + \sqrt{\frac{E_g^2}{4} + (\hbar vk)^2}$), while the behaviour at high energies remains asymptotically linear ($E \approx v\hbar k$). The extrapolation for the isotropic case ($\delta = 0$) of the flat-to-cone transitions to zero gives an analytical intercept $q = E_g/2$. The gap also determines the sign of the intercept.

levels for the interband excitations) which could cause a splitting of the transitions. But within the experimental linewidth such behaviour was not observed. Hence, the mentioned aspects lead us to the conclusion that δ needs to be limited in the absolute value to $|\delta| \leq 30$ meV. Such result is in agreement with the latest ab-initio calculation proposing $\delta \approx +30$ meV [54].

The low magnetic field measurements, carried out on the sample A-p, were further completed with high magnetic field data. Nevertheless, the sample was found in a slightly modified condition (lower E_F) and thus for the sake of clarity we present these results separately (Fig. 3.24a). In particular, the feature at 140 meV, evident in the magneto-transmission spectra, became more pronounced and hindered the higher interband transitions observed at the lower field before. Above 15 T, the cyclotron resonance $1^\downarrow \rightarrow 2^\downarrow$ is clearly visible within the experimental window (until 30 T), whilst a shoulder of the second CR mode $1^\uparrow \rightarrow 2^\uparrow$ is formed at low energies following the same behaviour as for the sample C-b measured in the reflectivity configuration (Fig. 3.16). Another weaker transition, marked by green arrows in the Fig. 3.24a, was tentatively attributed as an irregular intraband resonance $1^\uparrow \rightarrow 3^\uparrow$ that appears probably for the orientations deviated from the directions of the principal axes. The related fanchart summarizes all LL transitions measured in the high magnetic field in the reflectivity and transmission configuration (Fig. 3.24b). The fanchart was fitted with the Bodnar model for (112)-orientation using the perturbation method (appendix 6) with the maximum number of level $N_{\max} = 10$ yielding the optimal parameters listed in the Tab. 3.3, to be consistent with the previous observations.

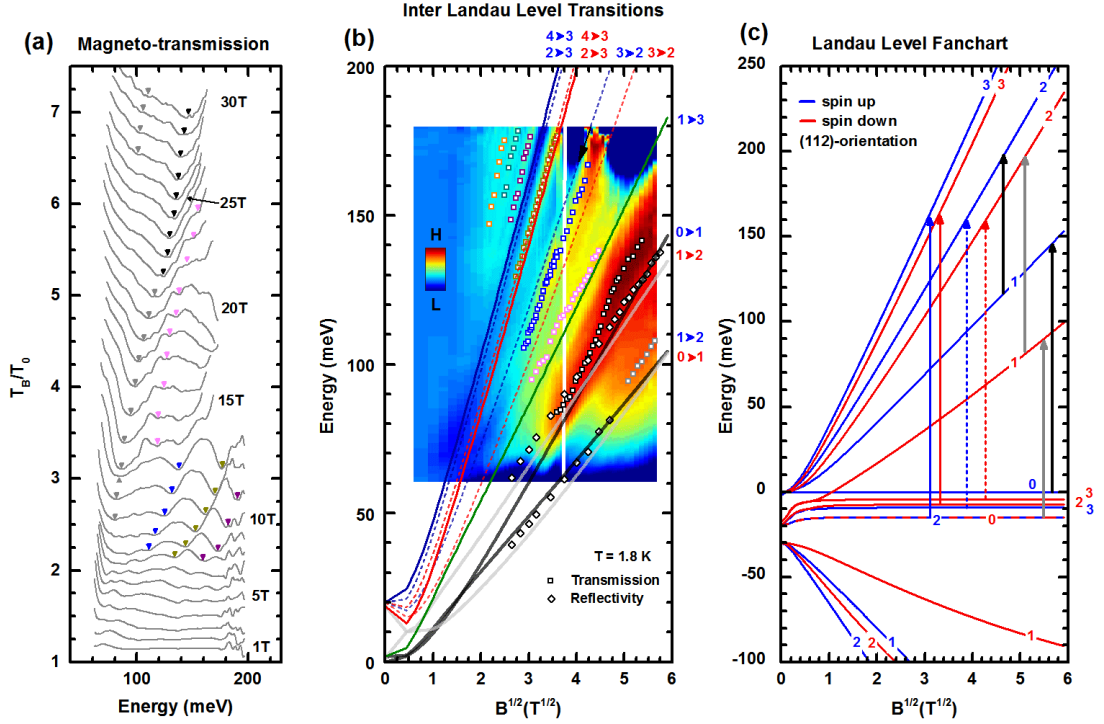


Figure 3.24: (a) The relative magneto-transmission data measured on the sample A-p in the high magnetic field displaying a strong cyclotron resonance between 15-30 T (black arrow). (b) The transition fanchart layered over a false-coloured absorbance map. The lines were fitted by the Bodnar model for the parameters from Tab. 3.3 and their designations are elucidated in the scheme (c).

Table 3.3: List of the Bodnar parameters concluded from the magneto-optical measurements. The anisotropy of the momentum matrix element is estimated as $\left| \frac{P_{\perp}}{P_{\parallel}} - 1 \right| \sim 10\%$

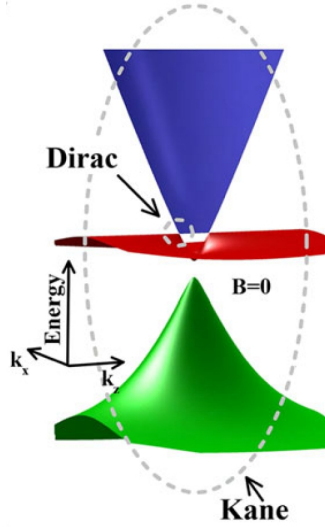
E_g [meV]	P_{\perp} [eV.Å]	P_{\parallel} [eV.Å]	Δ [meV]	δ [meV]
-(60-80)	7.5	7.5	400-600	$ \delta < 30$

It is worth to note that the precision in the determination of the parameters is limited, among other factors, by the fact that all present samples in this work as well as in the previous studies were strong intrinsic n-types with typical $E_F = 100$ -300 meV far above the expected LH-HH band crossing, causing that the impact of the remote bands E, SH is in the analysis less significant (and thus less decisive). The promising fabrication of p-type (or ideally intrinsic) samples is challenging, since it usually requires an increase of the carrier-concentration compensating element in the amount of few percent which consequently affects the studied band structure.

3.10 Summary

In summary, we have studied bulk Cd_3As_2 by means of optical magneto-spectroscopy, unambiguously showing the presence of 3D massless particles. We conclude that within

Figure 3.25: An illustration of the band structure of Cd_3As_2 including Dirac and Kane-type cones at two different energy scale. The small Dirac cones emerge as the result of the light hole and heavy hole band crossing. The main energy scale is dominated by 3D massless Kane electrons.



the investigated range of frequencies and magnetic fields, the observed response is due to massless Kane electrons [25] and not due to the Dirac electrons. For such a statement we present several arguments. Firstly, the zero field optical conductivity indicates a quasi-linear dependence characteristic for a 3D system with the linear E - k dispersion (Fig. 3.10). A specific relation (3.13) between the plasma frequency and Fermi level was found to be approximately valid. Secondly, we verified a linear relationship $E_F = m_c v^2$ between the cyclotron mass and Fermi level from the splitting of the plasma edge at low magnetic fields (Fig. 3.13). The Shubnikov de-Haas oscillations measured in transport (Fig. 3.11) gave us an estimation about the velocity parameter $v = 10^6$ m/s that is in agreement with the previous works [42, 58]. Thirdly, the fundamental CR mode was observed in magneto-reflectivity in the quantum regime with a clear \sqrt{B} -dependence that is independent of the initial Fermi level (Fig. 3.16). Such response can not be explained within the spectrum of Landau levels of the 3D Dirac system (due to the presence of 0-th LLs), but it can be simply interpreted using an isotropic Kane model that well matches in the quantum limit with the observed data. This interpretation is fully consistent with the Bodnar model elaborated for this material in the past (when δ is set to zero). Lastly, we observed interband Landau level excitations in the magneto-transmission, which could be only ascribed as flat-to-cone type optical transitions (Fig. 3.20). Their extrapolation to the zero field helped us to specify the size of an inverted bandgap $-(70 \pm 10)$ meV (a small departure from the gapless case of the Kane model) and the line assignment limits the value of the crystal field splitting $|\delta| < 30$ meV (a crossover to the Bodnar model). Furthermore, we propose a scenario where the 3D Dirac and Kane systems are able to coexist at two different energy scales (Fig. 3.25) under the condition of a positive crystal field splitting. The small, highly tilted Dirac cones are caused by a tetragonal distortion along the z -axis and they are created as a consequence of the LH and HH band crossing. Their presence is protected by the C_4 -axis of the rotational symmetry. On the other hand, the nodal point of the gapless Kane system is a result of the six-fold accidental degeneracy which can be lifted under the action of a small perturbation (for instance, by the change of temperature).

However, the current technology of the growth of bulk crystals does not allow to verify this proposition due to the high Fermi level, typically 100-300 meV, which is far above the expected Lifshitz point and the potential excitations within a small Dirac cone are Pauli-blocked. Nevertheless, we noticed that this situation is not inherent to Cd₃As₂ but it can be artificially achieved by a compressive strain between a thin layer and an appropriate substrate due to the lattice mismatch (appendix 8).

Our findings contradict the conclusions of ARPES studies, but we suggest an alternative band assignment for their experimental data, as labelled in the Fig. 3.2a, using the eight-band Kane/Bodnar model. The corresponding band parameters can be approximately read out as $E_g \approx \pm(50-100)$ meV, $\Delta \approx 0.6-0.8$ eV and $\delta \approx 0$ meV at $k_z = 0$.

4. Magneto-optics of bulk Bi_2Se_3

4.1 The state of the art

Bismuth selenide recently became probably the best known member of the broad family of topological insulators. Its bands are inverted, surface states are clearly separated from the bulk band structure and protected by time-reversal symmetry. The material is also technologically matured and relatively stable under ambient conditions. From the crystallographic viewpoint, the compound is built by stacking of the elementary, weakly coupled, quintuple layers with thickness $d_{\text{QL}} = 1 \text{ nm}$ [91] (Fig. 4.1a). An each quintuple layer is composed of five alternating monoatomic sheets of Bi and Se. The atoms within a sheet are arranged in a triangular lattice. The sheets are mutually stacked in an order -ABCAB-C... A conventional cell is created from three quintuple layers but the actual primitive cell consists of just five atoms and it is defined by the lattice vectors $\mathbf{t}_1, \mathbf{t}_2, \mathbf{t}_3$. The cell belongs to the rhombohedral space group $R\bar{3}m$ and has a three-fold axis in the z -direction together with a centre of the inversion [28].

The nature (direct, indirect) and the size of the bandgap in this system remained a subject of disputes. The interpretation of ARPES experiments implies a camel-back structure for the valence band and a parabolic conduction band with an indirect bandgap exceeding 300 meV [32, 92–94] (Fig. 4.2a). It was also shown that ARPES technique seems to be nearly ideal technique to visualize the surface states of topological insulators, which are rarely seen in transport or optical experiments. For Bi_2Se_3 the surface states have a form of a single conical band extending over the bandgap with reliable estimation of the velocity parameter $0.46 \times 10^6 \text{ m/s}$ extracted from their slope (including weak parabolic corrections). However, the observation of the individual bands strongly depends on the utilized photon energy. The STM experiments [95, 96] independently verified the relativistic-like nature of the surface states by the identical analysis of the quantum oscillations introduced earlier in the section 3.6 or in the ref. [58] (Fig. 4.2b). The modulation of the (local) density of states due to the quantization into Landau levels was only observed for the upper cone.

To put the value of the bandgap into the context of ab-initio computations, we mention a study [91] with the result of 0.23 meV that was carried out far before the renewed interest on Bi_2Se_3 due to its topological properties. In contrast, a widely referred paper [97], which compares the bulk band structure and the surface states also with the similar materials Bi_2Te_3 and Sb_2Te_3 , gives a rather large value of 0.56 eV. The more recent work [98] taking into account more rigorously the 2D quantum confinement of a finite slab provides again a significantly lower value 0.25 eV. Another computation using a GW-approximation [99] concluded a bandgap of 0.2 eV.

The optical experiments performed in the past on series of doped samples [100] as well as recent studies [73, 101, 102], including those summarized in this thesis, conclude a narrow direct gap $E_g = 0.20\text{-}0.22 \text{ eV}$. Recent magneto-optical investigations of topological insulators are primarily motivated by a lack of the experimental evidence of surface states in these materials and notably, by a number of theoretical predictions

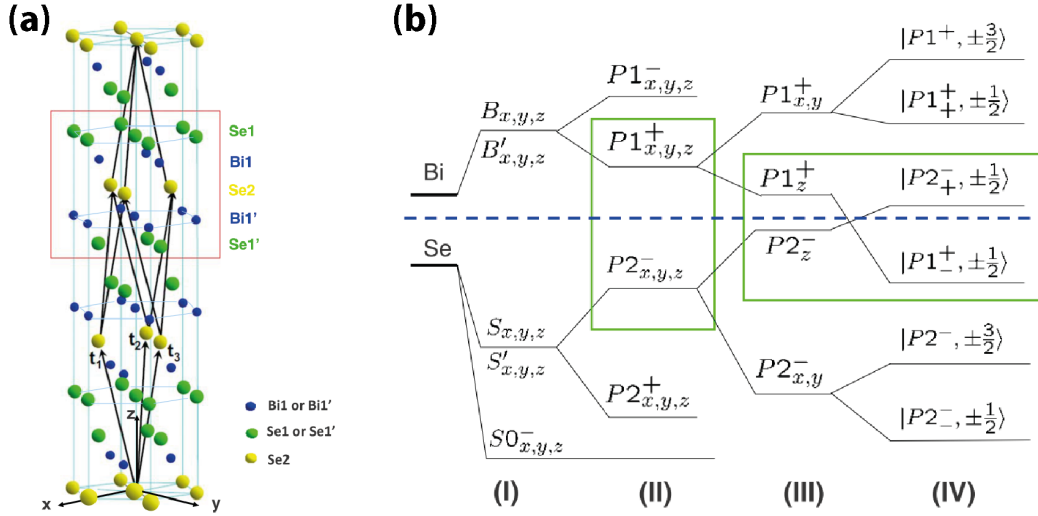


Figure 4.1: (a) Crystal structure of Bi_2Se_3 depicted as a layered medium of quintuple layers composed of five alternating Bi and Se sheets. The primitive cell is represented as a rhombohedral unit defined by the lattice vectors t_i (adopted from [28]). (b) A scheme of the band formation begins from the atomic orbitals of Bi and Se, followed by hybridization I, shaping of the bonding and anti-bonding molecular states II due to the inversion symmetry, crystal field splitting II and finished by adding the spin-orbit interaction IV that results into an inversion of the last occupied state with respect to the vacuum [28].

about the magneto-optical phenomena due to the surface physics of TIs [103].

Magneto-optical experiments [104, 105] performed recently (infrared as well as Raman studies) on graphene well document fairly rich physics related to the magneto-optical response of 2D systems with conical bands, in particular when quantized into Landau levels. Further theoretical predictions specifically for TIs are awaiting their experimental verification. The main question is whether a TI can be naively viewed as a stack of two semimetallic surface sheets which are separated by the inner bulk layer, which exhibit mutually opposite chiral behaviour and whose response are decoupled from each other and from the bulk. Interestingly, the quantized Faraday rotation from the relativistic-like surface states can be understood as an optical analog of the quantum Hall effect [106, 107] and it is promising to be detected in the THz range as was recently reported in the very first experimental studies [108–110].

4.2 Band structure from the BHZ-hamiltonian

It turned out that the approach of Bernevig, Hughes and Zhang [29] well describes the electronic band in the vicinity of the Fermi energy and also reasonably covers topological surface states. The analysis of the orbital functions including the spin-orbit interaction yields the p-state $|\text{Bi}^+, \pm\frac{1}{2}\rangle$ to be the last occupied and inverted with the p-state $|\text{Se}^-, \pm\frac{1}{2}\rangle$ of the opposite parity (Fig. 4.1b). These states form a basis for the effective four-band BHZ-Hamiltonian that describes low energy behaviour. Its essential form is identical with the 3D Dirac Hamiltonian for massive charge carriers expanded

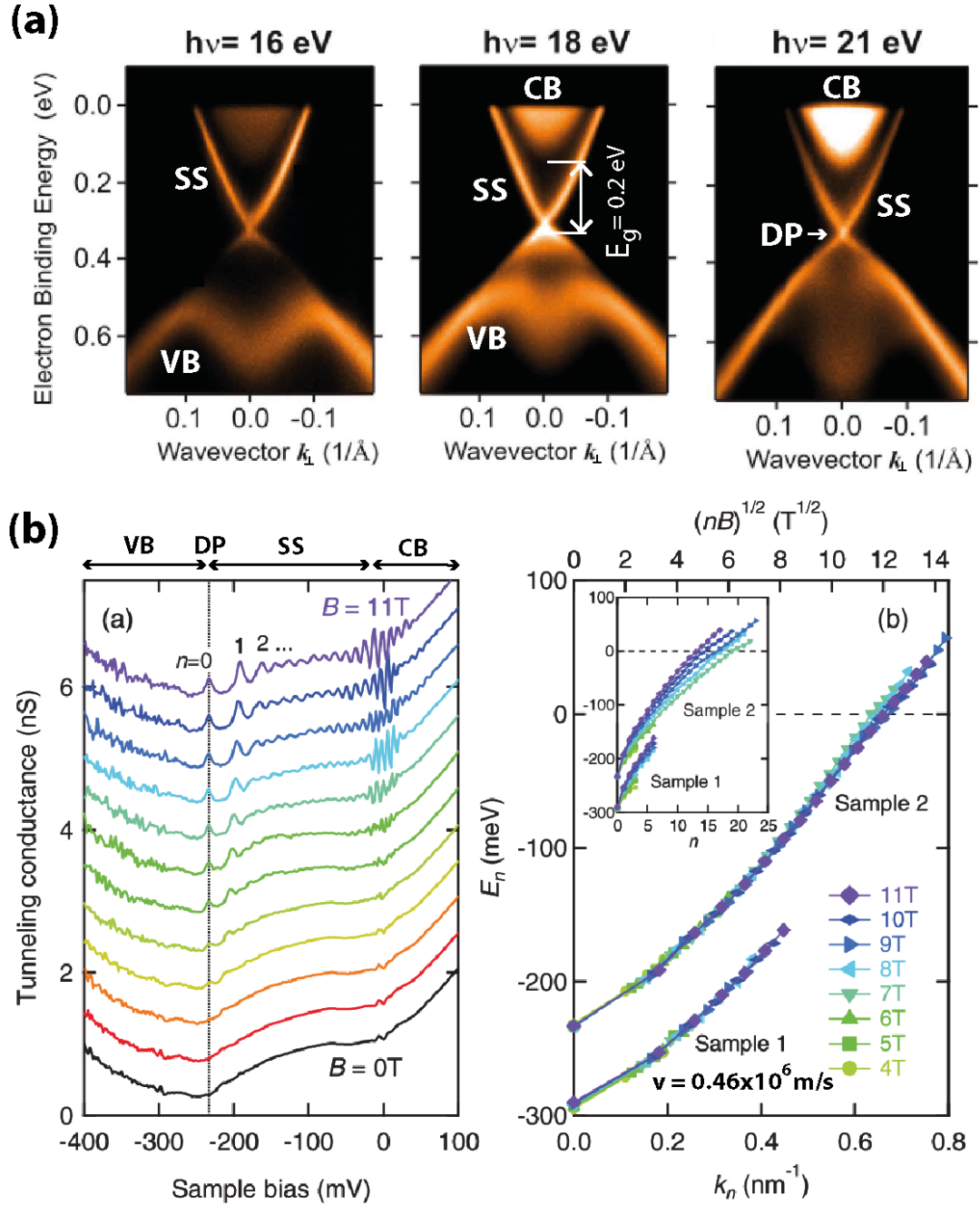


Figure 4.2: (a) A bands structure of Bi_2Se_3 measured by ARPES reveals Dirac-like surface states spanning between the bulk conduction and valence bands [94]. However, the sensitivity for the individual bands depends on the selected photon energy. The camelback shape of the valence band is pronounced for $h\nu = 16$ eV and evokes a gap of $E_g = 0.4$ eV but the actual bulk gap is twice smaller and the top of the valence band coincides with the Dirac point. (b) An STM Landau level study shows Shubnikov-de Haas oscillations whose analysis yields a linear E - k dispersion of the top Dirac cone of the surface states [95]. The slope of the line provides a value of the velocity from the BHZ-model. The oscillations were observed only in the voltage range 0-0.25 V from the total tunable interval of 0.5 V. But, such a span coincides with the value of the E_g received from the optics.

to include an uniaxial anisotropy (in the z -direction) and electron-hole asymmetry [97]. The general form of H_{BHZ} has a complex structure $H_{\text{BHZ}} = \epsilon(\mathbf{k})I + \sum_i d_i(\mathbf{k})\Gamma_i + \sum_{ij} d_{ij}(\mathbf{k})\Gamma_{ij}$ with the Dirac matrices Γ_{1-5} satisfying $\{\Gamma_i, \Gamma_j\} = 2\delta_{ij}$ and their ten commutators $\gamma_{ij} = \frac{1}{2i}[\Gamma_i, \Gamma_j]$. The functions $\epsilon(\mathbf{k})$, $d_i(\mathbf{k})$, $d_{ij}(\mathbf{k})$ can be expanded in a power of the momentum \mathbf{k} . To capture just the essential properties, we adopt the minimal Hamiltonian (1.19)

$$H_{\text{BHZ}} = \begin{pmatrix} \frac{E_g}{2} + (C+M)k^2 & \hbar v_{\perp} k_+ & 0 & -\hbar v_{\parallel} k_z \\ \hbar v_{\perp} k_- & -\frac{E_g}{2} - (M-C)k^2 & \hbar v_{\parallel} k_z & 0 \\ 0 & \hbar v_{\parallel} k_z & \frac{E_g}{2} + (M+C)k^2 & \hbar v_{\perp} k_- \\ -\hbar v_{\parallel} k_z & 0 & \hbar v_{\perp} k_+ & -\frac{E_g}{2} - (M-C)k^2 \end{pmatrix} \quad (4.1)$$

that is completed with a free-electron term Ck^2 originating in $\epsilon(\mathbf{k})$ and causing a departure from the electron-hole symmetry [73].

The uniaxial anisotropy of the material in the z -direction is expressed by difference of the in-plane and out-of plane velocity parameters. The effect of higher bands are partially included in C , M parameters. A hexagonal warping and other higher terms were neglected at low energies being insignificant for the explanation of main effects observed in the optical experiments. Let us also note the BHZ-Hamiltonian, deduced from the symmetry arguments is equivalent (in the first order of momentum) to the (truncated) k.p approach elaborated in the ref. [28]. When we restrict ourself to the purely in-plane case with $k_z = 0$, then the Hamiltonian (4.1) becomes block-diagonal and the band dispersion simply reads

$$E(k) = Ck_{\perp}^2 \pm \sqrt{\left(\frac{E_g}{2} + Mk_{\perp}^2\right)^2 + (v_{\perp}\hbar k_{\perp})^2}. \quad (4.2)$$

On the basis of the cyclotron resonance and the interband transitions linearly developing in B ([73] and appendix 9), the energy dispersion needs to be necessary close to parabolic as argued in the sec. 1.7 for nonzero v . In order to turn the rather complex dispersion relation (4.2) into the parabolic, an additional condition has to be fulfilled, which interconnects the strengths of the inversion with the velocity parameter and the bandgap

$$(\hbar v_{\perp})^2 = -2ME_g. \quad (4.3)$$

This condition reduces the number of free parameters in the BHZ-Hamiltonian down to two (when the anisotropy of the system is neglected). Notably, the condition can be also only fulfilled in systems with non-trivial ordering of the electronic bands ($M.E_g < 0$, under the convention of $E_g > 0$, $M < 0$, $v_{\parallel, \perp} > 0$). Thus, the dispersion simplifies to the form that is practically identical with a wide-gap semiconductor

$$E(k_{\perp}) = \begin{cases} +E_g/2 + (C-M)k_{\perp}^2 \\ -E_g/2 + (C+M)k_{\perp}^2 \end{cases}. \quad (4.4)$$

The effective electron and hole masses can be defined from the kinetic terms of the

4.3. Determination of the bandgap

Table 4.1: The list of the band parameters in the BHZ-model obtained from the preceding Landau level study [73].

E_g [eV]	v_{\parallel} [m/s]	M [eV.Å ²]	C [eV.Å ²]
0.2	0.48×10^6	$-(22.5 \pm 1.0)$	(3 ± 0.5)

eq. (4.4) as

$$\begin{aligned} m_e &= \frac{\hbar^2}{2(C-M)} = \frac{2\hbar^2}{\frac{\hbar^2}{m_D} + 4C} \\ m_h &= \frac{\hbar^2}{2(C+M)} = \frac{2\hbar^2}{\frac{\hbar^2}{m_D} - 4C} \end{aligned} \quad (4.5)$$

where we introduced a Dirac mass $m_D = -\frac{\hbar^2}{4M}$, which among others plays the role of the reduced mass since $\frac{1}{m_D} = \frac{1}{m_e} + \frac{1}{m_h}$. The Dirac mass allows us to reformulate the condition (4.3) into the Einstein relation

$$\Delta = m_D v_{\perp}^2 \quad (4.6)$$

with $\Delta = \frac{E_g}{2}$. In the approximation of $|M| \gg C \approx 0$, the conduction and valence bands become nearly symmetric ($m_e \approx m_h$) and the energy dispersion simply reads

$$E(k_{\perp}) = \begin{cases} +\Delta + \frac{\hbar^2 k_{\perp}^2}{2m_e} \\ -\Delta - \frac{\hbar^2 k_{\perp}^2}{2m_e} \end{cases}.$$

In contrast to the eq. (1.2), a halfgap Δ cannot be directly associated with the restmass term $m_0 c^2$, since the kinetic term contains the effective electron mass instead of the Dirac mass. When the BHZ-Hamiltonian is subjected to the boundary condition, the chiral massless states with the energy dispersion $E_{ss} = Ck_{\perp}^2 \pm \hbar v k_{\perp}$ closely resemble 2D Dirac particles [28, 95]. The summary of the band structure parameters deduced from the magneto-optics is listed in the Tab. 4.1.

4.3 Determination of the bandgap

The bandgap was investigated intensively by ARPES technique on bulk and deposited layers, while a rigorous (magneto-)optical study concerning the bandgap was done only on epilayers, where the result can be effected by the residual strain from the lattice mismatch. For our experiments, the bulk crystals of Bi₂Se₃ were grown at the Institute of Electronic Materials Technology in Warsaw and at the Faculty of Chemical Technology of the Pardubice University using the modified Bridgman method, where a stoichiometric mixture of high purity Bi and Se elements was vacuum sealed in a quartz tube, heated up to the melting point and cooled down to the room temperature with the rate of 0.1 K/min under the temperature gradient of about 10 K/cm along the

tube length in a box furnace. As-grown crystals showed a strong n-type doping (close to $\sim 10^{19} \text{ cm}^{-3}$) due to selenium vacancies, which was reduced (down to $\sim 10^{18} \text{ cm}^{-3}$) by the after-growth annealing in selenium vapours.

For the transmission experiments, the ingot with a diameter of 1 cm was sliced using microtome machine perpendicular to the c -axis into slabs with the thickness ranging from 10-200 μm of various carrier densities due to inhomogeneity of the crystal. Thinner 2-5 μm self-standing layers were exfoliated with smaller lateral dimensions due to the layered character of the material, but in the expense of a reduced diameter of the aperture ($\sim 0.5 \text{ mm}$).

The most straightforward method to get estimate about the size of the direct gap is by measuring emission from the electron-hole recombination between the top of the valence band and bottom of the conduction band upon the excitation from the laser with $E > E_g$ (Fig. 4.3a). The low-energy onset of the photoluminescence peak (inflexion point) is fixed and assign as the bandgap $E_g = (220 \pm 5) \text{ meV}$. The centre and the width of the PL line depend on the hole occupancy close to the top of the valence band that is given by the laser power and excitation efficiency. We have not observed any exciton-like character of the recombination due to the screening from degenerated electron gas. However, as it is common for semiconductors with strong disorder and impurities, other recombination radiative channels can be realized from the defect levels located in the gap. This would give rise to the sub-bandgap emission, which can not be in principal excluded and then the extracted gap E_g from the data would be the lower bound for the real direct gap. A recent ab-initio calculation [111] investigated resonant levels in Bi_2Se_3 arising from Se vacancies (which are the prevailing intrinsic type of defect with the largest contribution to the unintentional doping). The study showed that the emerged level is rather shallow or even hybridized with bottom of the conduction band and if the photoluminescent transition is realized through the defect level, the estimated value of the bandgap should not be significantly altered.

The transmission of thin slabs is restricted at low energies by the free-carrier response that forms a plasma edge in the reflectivity. At high energies, the absorption is caused by interband transitions with a shifted onset

$$E_g^{opt} = E_g + \Delta E_{\text{MB}} \quad (4.7)$$

for the doped samples in a dependence on the Fermi level as

$$\Delta E_{\text{MB}} = \left(1 + \frac{m_e}{m_h}\right) E_F \quad (4.8)$$

that could be approximated in the case of bands with a high e-h symmetry as $\Delta E_{\text{MB}} = 2E_F$ (Fig. 4.3b). An approximate read-out of E_g^{opt} is possible, when the transmission is plotted as an absorbance $a(E)$ and normalized by the sample thickness d (insets of 4.3b). When the optical band gap is approached, the absorbance becomes dominantly governed by absorption $a(E) \approx -\ln(T(E))/d$, which increases rapidly due to the non-negligible in-gap absorption for thicker samples that has a character of an Urbach edge/tail in real disordered systems. The inflexion point of the absorption edge

would ideally serve as an indication of E_g^{opt} but its position is hardly visible due to the rapid suppression of the intensity. Thus, the optical bandgap may then be associated with the photon energy at which the absorption coefficient α approaches 10^4 cm^{-1} , a value typical for the interband absorption in direct-band-gap semiconductors, as it is documented on a 6.5 and 10 μm -thick n-doped samples giving $E_g^{opt} \approx (250 \pm 10)$ and $E_g^{opt} \approx (260 \pm 10)$ meV, respectively.

From the Shubnikov-de Haas oscillations observed in low-temperature transport measurements on the same sample within 4-14 T, we can extract using the equation (3.19) a characteristic frequency of the magnetic field $B_f = \frac{m_e E_F}{e\hbar} \approx (22.0 \pm 0.5)$ T from the Onsager relation (3.17) assuming equal LL spacing in a parabolic band $E = \frac{\hbar^2 k^2}{2m_e}$. Then, the Moss-Burstein (MB) shift (4.8) can be rewritten as $\Delta E_{\text{MB}} = \frac{e\hbar B_f}{\mu}$ using the reduced mass $\mu = \frac{m_e m_h}{m_e + m_h}$.¹

Relatively rich literature about Bi_2Se_3 provides us with a fairly wide interval of estimates of the electron and hole effective masses, but the reduced mass appears to be a robust quantity $\mu = 0.08m_0$ to the particular deviations (Tab. 4.2). For instance, the analysis of SdH oscillations and their temperature dependence provides us with the electron mass [112–114] that is roughly comparable to the values obtained directly from the cyclotron resonance [73, 115]. The optical studies performed in the past analysed reflectivity curves for the different carrier concentrations and on the basis of the plasma edge shift [100] or on the Fermi level [116], the electron mass was deduced as $0.125m_0$ and $0.18m_0$ respectively. The knowledge of the reduced mass provides us with a MB shift of 30 meV, which with the use of the formula (4.7) gives the bandgap $E_g = (0.22 \pm 0.01)$ eV that is in perfect agreement with the PL measurement. The transmission of

m_{D}^{\perp}	0.08 [25]
m_e^{\perp}	0.13 [112, 114], 0.14 [25, 117, 118], 0.16 [115]
m_h^{\perp}	0.19 [25], 0.25 [119]
m_e^{\parallel}	0.16 [118], 0.2 [112, 120]
g_e^{\perp}	25 [25], 27.5 [121], 32 [120]
g_e^{\parallel}	19.5 [121]
g_h^{\perp}	25 [25], 30 [121]
g_h^{\parallel}	19 [121]

Table 4.2: Effective masses (in units of m_0) and g-factors extracted from the NMR, ESR, optical and transport studies.

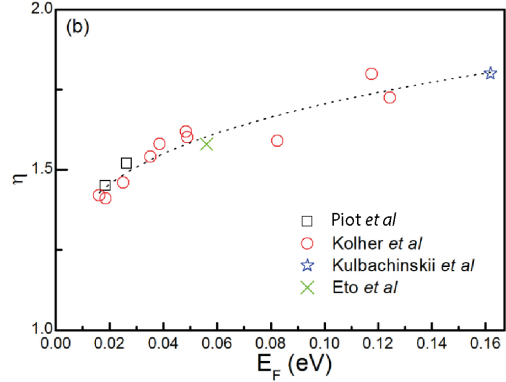


Figure 4.4: Anisotropy of the frequency of the Shubnikov-de Haas oscillations $\eta = B_f^{\parallel} / B_f^{\perp}$ in the dependence on the Fermi level collected from the earlier works on n-type samples [120].

the thin slabs strongly depends on the selected thickness (Fig. 4.5a). The thinnest layers of 1-3 μm are the most appropriate for studying the absorption edge and gap.

On the other hand, from an intermediate thickness 10 μm the refractive index N

¹In the context of the BHZ-theory, the reduced mass μ and the Dirac mass m_{D} are the identical quantities in the bismuth selenide.

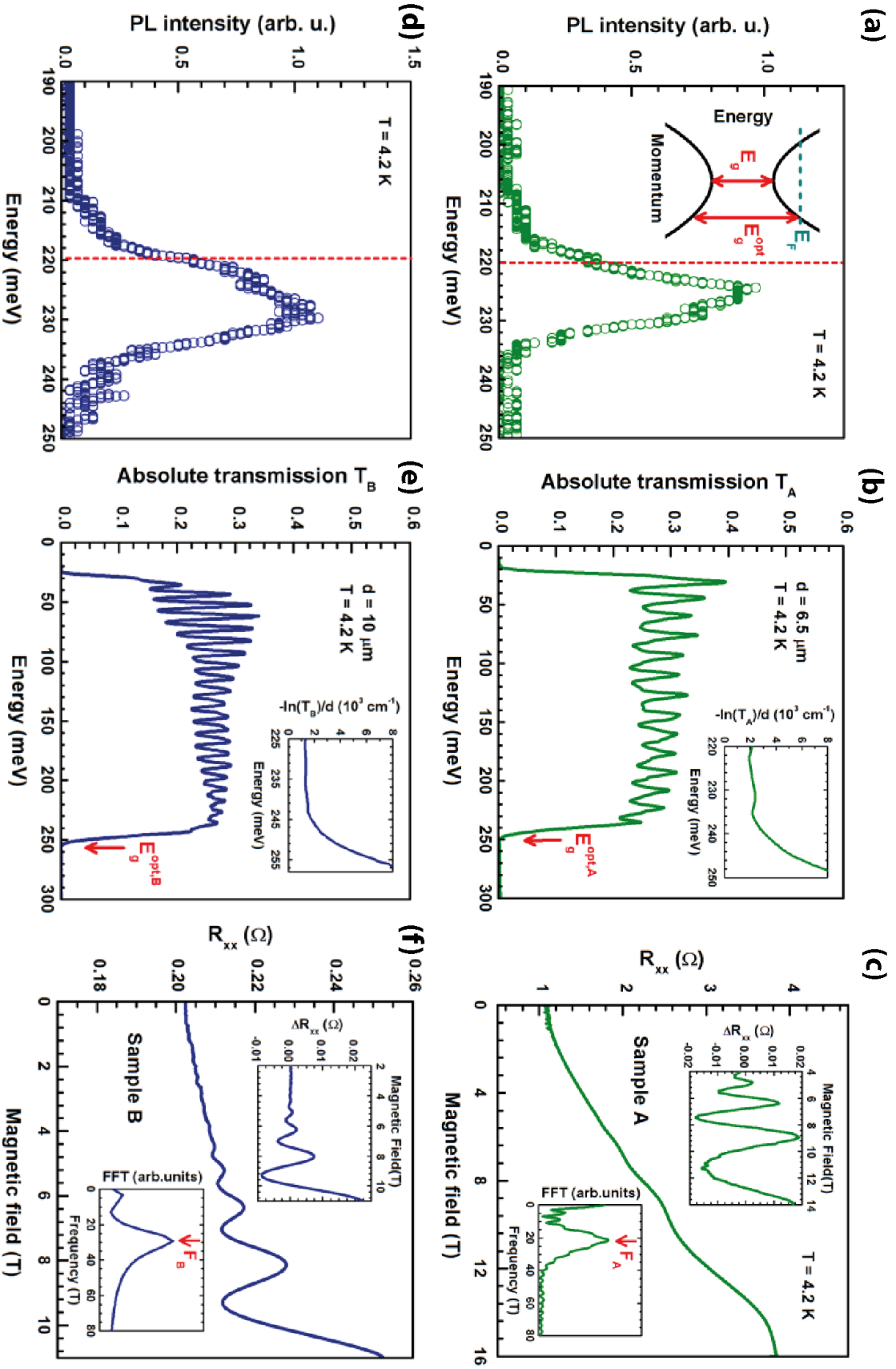


Figure 4.3: (a) Low temperature photoluminescence shows a clear peak of the direct-band recombination. The red line signifies the value of the bandgap. (b) Transmission of a slab is limited at low energies by a plasma edge at ≈ 15 meV and by the interband absorption E_g^{opt} that is shifted due to the finite Fermi level (inset of (a)). The absorption coefficient shows a rapid onset at 250 meV (inset). (c) After the subtraction of the background the magneto-resistance R_{xx} of the same sample reveals Shubnikov-de Haas oscillations with a characteristic frequency F .

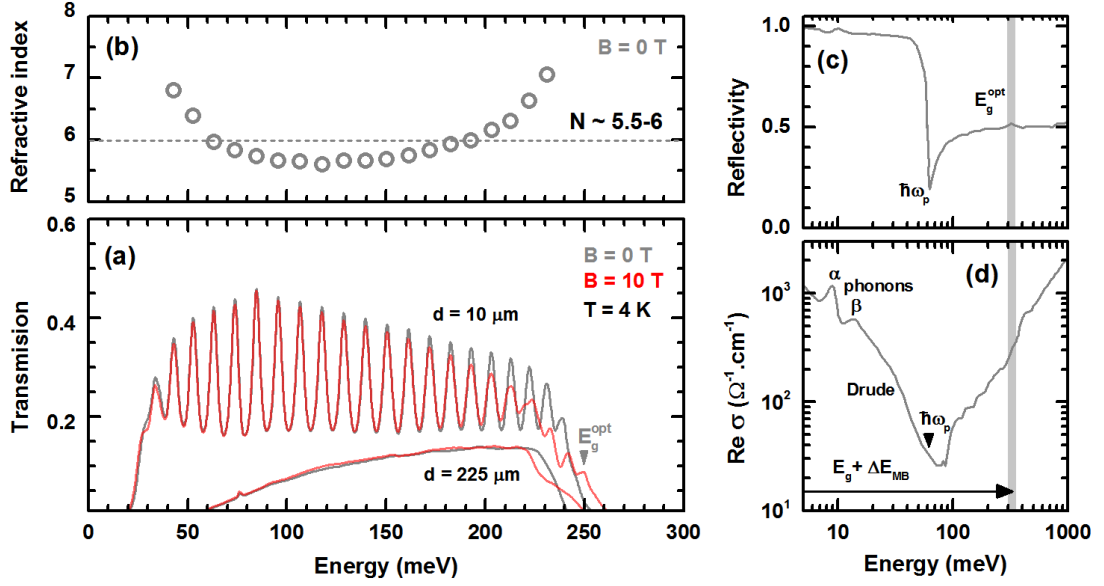


Figure 4.5: (a) A transmission of thin self-standing layers strongly depends on the thickness. A thin slab is characteristic by pronounced Fabry-Perot modulations that provides an information about the refractive index as a function of the energy. A thicker sample is less transparent due to the residual absorption within the gap but the absorption edge is not obscured by the oscillation pattern. This allows to observe the splitting of the edge in the magnetic field which causes interband magneto-dichroism. (c) A typical reflectivity of an n-doped sample with the Fermi level of 50 meV. The signature of the interband absorption onset E_g^{opt} is marked in the curve by a grey strip (adopted after [122]). (d) An associated optical conductivity shows a Drude peak at low energies and interband absorption at high energies ($E > E_g^{opt}$). Besides, a gradual absorption develops in a window restricted by $\hbar\omega_p$ and E_g^{opt} reducing the transparency, see a transmission curve for the thickness of 225 μm in (a).

as a function of energy can be easily calculated from the extrema positions of the pronounced Fabry-Perot modulations as

$$N = \frac{1}{2d} \frac{\lambda_n \lambda_{n+1}}{\lambda_n - \lambda_{n+1}} \quad (4.9)$$

at the given wavelengths λ_n , λ_{n+1} . The refraction index turned out to be approximately constant 5.5-6 for the in-gap excitations and independent on the carrier concentration in agreement with ref. [116]. Finally, the samples with highest thickness of ≈ 100 -200 μm are ideal for the measurement of the Faraday rotation as will be shown in next sections.

The plasma edge and the Fermi level are interconnected by the equation (3.14) for the 3D electron gas in parabolic band. Recovering the reflectivity data from the ref. [122], the optical gap was observed at 330 meV for the sample with a plasma frequency at 60 meV (Fig. 4.5c). The associated conductivity presents a Drude peak at low energies and a gradual onset at high energies with a soft step at E_g^{opt} . Such a residual absorption in the interval $\hbar\omega_p$ and E_g^{opt} causes the in-gap opacity as it was documented on the transmittance for different sample widths. Besides, the two phonon modes α , β appear in the optical response at energies 7.5 meV and 16.5 meV, respectively.

The interband optical transitions from the preceding Landau level spectroscopic

study linearly extrapolate to the value of the bandgap 0.2 eV (Fig. 9.2c in the appendix 9) that is smaller by 20 meV than the result from the analysis of the bulk crystals. The discrepancy is attributed to the remanent stress from the lattice mismatch between the substrate (InP) and layer (Bi_2Se_3), which is more pronounced for the thinner layers [73].

One scenario how to resolve the disparity with ARPES conclusions about the band structure suggests a following explanation. Let us consider the Dirac-like surface states to be asymmetrically positioned with respect to the bulk bands in the way that the charge neutrality point coincides with the top of the valence band. Then, the upper cone of the surface states spans over the bandgap, while the bottom cone forms an envelope for the valence band. This compensates the factor of two in the gap discrepancy which is achieved for the case when the Dirac point is placed symmetrically in the middle of the gap. The observed camelback structure of the valence band could arise from two causes. Either due to the stacking of the Z -point over the Γ -point in the vertical projection of BZ. Then, the in-plane dispersion could have a character of an indirect valley in Z -point that is superimposed over a parabolic dispersion at the Γ -point [53]. Another explanation is based on a 2D quantization (emerged from the finite size of the a real crystal) which modifies the 3D bulk valence band into a set of 2D subbands. The ARPES technique would be more sensitive to such a situation due to the limited penetration depth [98]. Interestingly, a band bending could also play an important role on the formation of such a finer structure.

4.4 Magneto-circular dichroism

The interest in magneto-circular dichroism in bismuth selenide is driven by an effort to observe Faraday and Kerr rotation from the surface states. But for such experiments it is necessary to firstly fully investigate the bulk response which may hinder the identification of the surface contribution. In the next section, we will focus on the interband bulk contribution to the magneto-dichroism and we will try to describe it using the simple classical model for the band structure introduced earlier.

The bulk interband magneto-dichroic behaviour purely originates in changes of the band occupation and is further fostered by an equality between the valence and conduction g-factors $|g_e| \approx |g_h|$. Such charge redistribution leads to the spin polarization of (in our case, conduction band) electrons in the magnetic field that is usually referred in the literature as the Pauli paramagnetism [123]. The Zeeman field affects the Pauli-blocking and defines the onsets of the transitions $\mathbf{e}_+ : |v^\downarrow\rangle \rightarrow |c^\uparrow\rangle$ and $\mathbf{e}_- : |v^\uparrow\rangle \rightarrow |c^\downarrow\rangle$ responsible for the interband absorption.² The detailed treatment of the Landau levels in bismuth selenide was elaborated in the paper [73]. In the appendix 9, we briefly review the quantization procedure for the completeness. The bands $|v^\uparrow\rangle, |c^\downarrow\rangle$ constitute the Landau set A and $|v^\downarrow\rangle, |c^\uparrow\rangle$ belong to the set B. Without the magnetic field, the both transitions are degenerate and equal to E_g^{opt} (Fig. 4.6), while in the presence of the field the bottom of the band $|c^\uparrow\rangle$ shifts up by $g_e\mu_B B s^\uparrow$ and $|c^\downarrow\rangle$ moves down by $-g_e\mu_B B s^\downarrow$.

²In this shortened notation, the bismuth valence states is denoted as $|v\rangle$ and the selenium conduction states as $|c\rangle$.

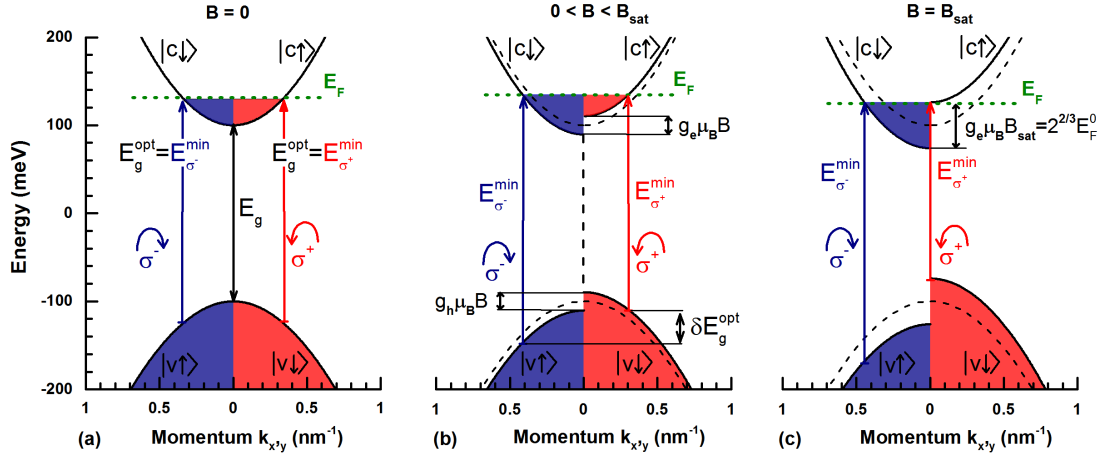


Figure 4.6: The three successive stages of an evolution of the magneto-circular dichroism described within the classical regime. (a) The electronic bands of the n-type sample at zero field. The vertical arrows indicate the lowest allowed interband excitations that are Pauli-blocked due to the occupation effect. (b) The magnetic field induces splitting of the conduction and valence band in the same magnitude and the onset is affected only by redistribution of the carriers to equilibrate the Fermi level. (c) If the situation arrives to the point when the $|c^{\uparrow}\rangle$ band becomes completely depopulated, the splitting between the minimal transitions saturates.

The spin projection s is identical $s^{\uparrow,\downarrow} = \pm \frac{1}{2}$ for selenium as well as for bismuth bands (Fig. 4.1), so the total splitting between the conduction bands for the spin up and down reads simply $E_s = g_e \mu_B B$.

The energy of the transition onset can be written as

$$E_+^{\min} = E_g^{\text{opt}} - \frac{\delta E_g^{\text{opt}}}{2} = E_g + \frac{\hbar^2 k_+^2}{2m_e} + \frac{\hbar^2 k_{\pm}^2}{2m_h},$$

$$E_-^{\min} = E_g^{\text{opt}} + \frac{\delta E_g^{\text{opt}}}{2} = E_g + \frac{\hbar^2 k_-^2}{2m_e} + \frac{\hbar^2 k_{\pm}^2}{2m_h}$$

or using the reduced Dirac mass as $E_{\pm}^{\min} = E_g + \frac{\hbar^2 k_{\pm}^2}{2m_D}$. From the geometry of the conduction band, we obtain a difference of the kinetic terms as

$$\frac{\hbar k_+^2}{2m_e} - \frac{\hbar k_-^2}{2m_e} = g_e \mu_B B, \quad (4.10)$$

which helps us to express the splitting of the absorption edge

$$\delta E_g^{\text{opt}} = E_-^{\min} - E_+^{\min} = \left(g_e \frac{m_e}{m_h} + g_h \right) \mu_B B \approx 2E_s = 2g_e \mu_B B, \quad (4.11)$$

which can be directly observed in the magneto-transmission spectra (Fig. 4.5).

The Fermi level is balanced in the conduction band for both spins, therefore $|c^{\uparrow}\rangle$ becomes more and more populated with the field increment in the expense of emptying of the $|c^{\downarrow}\rangle$ band. This proceeds until the critical field B_{sat} is reached, when all $|c^{\uparrow}\rangle$ states end up completely charge depleted and a further increase of the field does not change the minimal transitions $E_+^{\min} = E_g$ and $E_-^{\min} \approx E_g + 2E_s^{\text{sat}}$. However, the total

number of extrinsic carriers $N_e = N_e^\uparrow + N_e^\downarrow$ in the system is conserved regardless on the field as described

$$N_e = 2 \int_0^{E_{F0}} D_c(E) dE = \int_0^{E_{F,B}} D_c(E) dE + \int_0^{E_{F,B}+E_s} D_c(E) dE. \quad (4.12)$$

using the density of states of the 3D electron gas with a parabolic dispersion

$$D_c(E) = \frac{1}{(2\pi)^3} 4\pi \left(\frac{2\mu}{\hbar^2}\right)^{\frac{3}{2}} \frac{\sqrt{E}}{2}. \quad (4.13)$$

The expression (4.13) allows us to determine the spin-splitting $E_s^{sat} = g_e \mu_B B_{sat}$, when the Fermi level energy drops to the bottom of $|c^\uparrow\rangle$ as

$$E_s^{sat} = 2^{\frac{2}{3}} E_{F0}. \quad (4.14)$$

So, the saturation field

$$B_{sat} = \frac{2^{\frac{2}{3}} E_{F0}}{g_e \mu_B} \quad (4.15)$$

depends only on the initial Fermi level E_{F0} and on a given electronic g-factor.

The experimental value of the splitting of the thin slab $d \approx 10 \mu\text{m}$ with $E_F = 15 \text{ meV}$ was found to be 2.3 meV/T from the development of the absorption edges in the magnetic field (Fig. 4.7). The saturation of the splitting comes around 19 T that matches with the value from the expression (4.15). The circularly polarized transmission on the thicker sample $d = 225 \mu\text{m}$ with $E_F = 15 \text{ meV}$ showed consistently a splitting of 20 meV at 10 T that is independent of the carrier density. A similar value of the splitting 2.6 meV/T can be obtained using the parameters from the Landau level study [73] (Tab. 4.1). Alternatively, the slope can be also calculated from the formula (4.11) with the use of known g-factors from the table (4.2) yielding $\approx 2.7 \text{ meV/T}$.

The opposite doping principally leads to the same dichroic behaviour but it takes place in the valence band and the analogical saturation phenomenon is expected to happen in high magnetic fields. The p-type doping can be achieved by alloying $\text{Bi}_{2-x}\text{M}_x\text{Se}_3$ with the substituent $\text{M}=\text{Cu}, \text{Ca}$ in the units of percent [119]. However, an extensive disorder associated with a variation of the composition deteriorates the quality of the material, broadens the absorption edge and obscures its splitting.

In analogy to the transmittance, the saturation effect naturally also occurs in the case of the photoluminescence where the direct-gap emission is quenched with the rise of the field from two reasons (Fig. 4.8a,b). Firstly, the photo-generated hole pocket is thermalized to the top of the upward dispersing $|v^\uparrow\rangle$ branch and the radiative channel persists only for \mathbf{e}_+ , while the band $|v^\uparrow\rangle$ remains totally occupied and thus blocked for the radiative recombination processes. Secondly, the conduction band $|c^\uparrow\rangle$ is being depleted resulting in a suppression of the PL intensity. This is documented on the tendency of the integrated PL signal (Fig. 4.8c).

The situation can be alternatively described via considerations of the electron occupation in the quantum formalism of the Landau levels. With the total number of

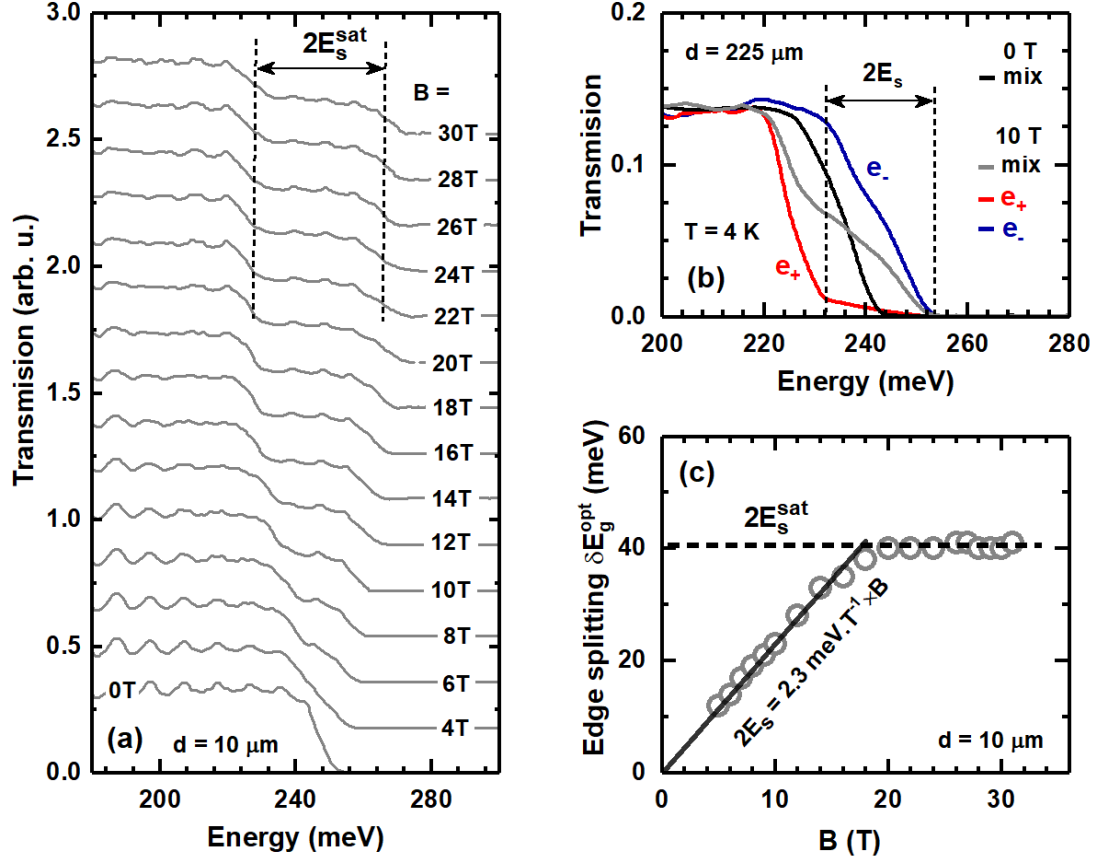


Figure 4.7: (a) The splitting of the absorption edge, observed on a thin sample in a dependence on the magnetic field, gradually develops until the arrival of the saturation around 20 T. (b) The polarization resolved transmission measured on a thick slab demonstrates that the summation of the both components e_+ , e_- gives a double-step absorption edge as for the naturally mixed light in the case of (a). (c) The splitting is firstly proportional to the field, afterwards it reaches a constant value above B_{sat} .

carriers being constant, the electrons are redistributed over the Landau levels in the conduction band according to the general equation

$$N_e = \frac{1}{2\pi} \left(\sum_{n=1}^{n_{\max}^{\uparrow}} k_{Fnz}^{\uparrow} + \sum_{n=0}^{n_{\max}^{\downarrow}} k_{Fnz}^{\downarrow} \right) \zeta_{2D}, \quad (4.16)$$

where $\zeta_{2D} = \frac{eB}{h}$ is the in-plane LL degeneracy and k_{Fnz} denotes the Fermi momentum of the n -th LL in the z -direction satisfying an equation

$$\begin{aligned} E_{F,B} &= E_n^{\uparrow}(B, k_{Fnz}^{\uparrow}) \text{ for } n = 1, \dots, n_{\max}^{\uparrow}, \\ E_{F,B} &= E_n^{\downarrow}(B, k_{Fnz}^{\downarrow}) \text{ for } n = 0, 1, \dots, n_{\max}^{\downarrow}, \end{aligned} \quad (4.17)$$

where $E_{F,B}$ denotes the Fermi level at the specific field and n_{\max} is a number of the last occupied LL. The saturation in the n -type system emerges when the Fermi level $E_{F,B}$ drops from the pinned levels 1^{\uparrow} , 2^{\downarrow} to the level 1^{\downarrow} (Fig. 4.9c). Afterwards, the quantum limit is reached, if $E_{F,B}$ drops from 1^{\downarrow} to 0^{\downarrow} . The both later cases can be related using

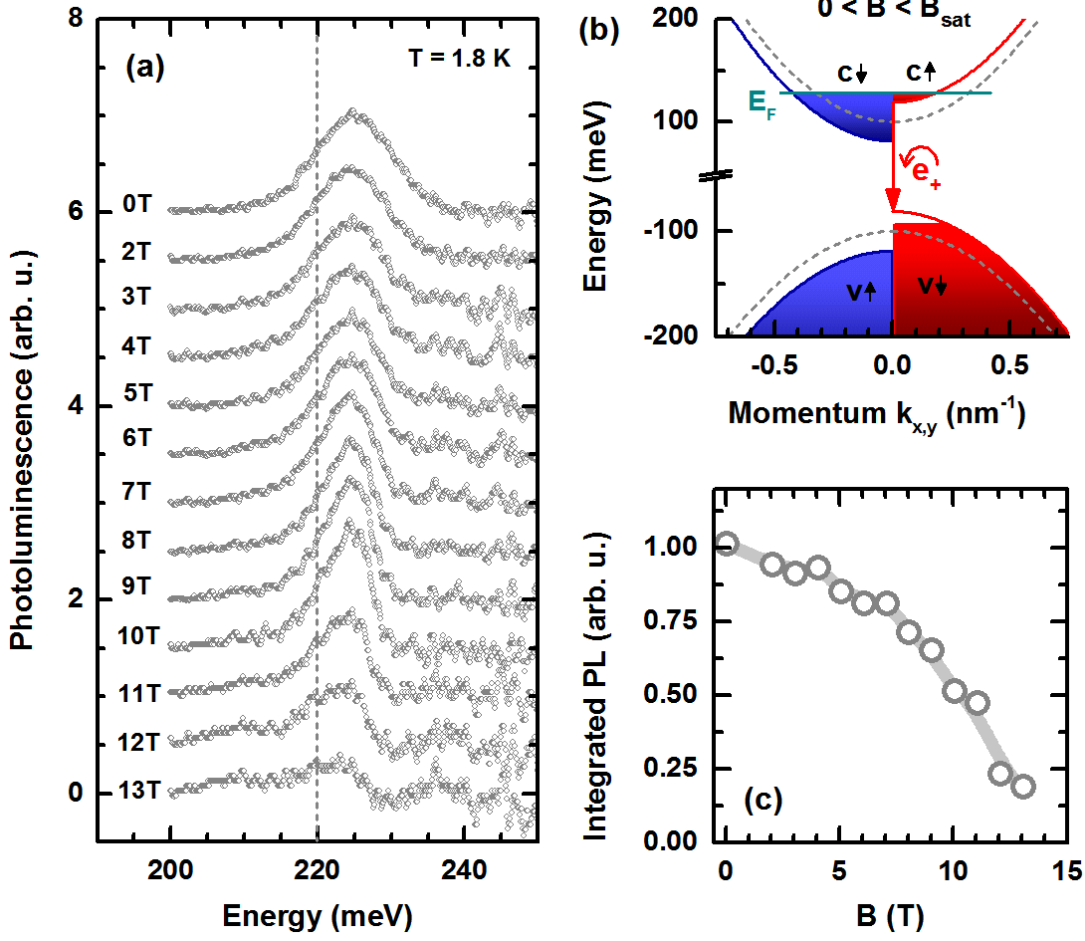


Figure 4.8: (a) The evolution of the PL signal as a function of the magnetic field shows a monotonous extinction of the emission. (b) The splitting causes the transfer of holes into $|v^{\uparrow}\rangle$ which favours the transitions e_+ , while e_- is being suppressed. Besides, the depletion of the conduction band $|c^{\uparrow}\rangle$ leads to the gradual reduction of the PL intensity (c).

eq. (4.16) as

$$\frac{eB_{sat}}{h} \frac{1}{2\pi} (k_{F1z}^{\downarrow,sat} + k_{F0z}^{\downarrow,sat}) = \frac{eB_{QL}}{h} \frac{1}{2\pi} k_{F0z}^{\downarrow,QL} \quad (4.18)$$

and with the use of the saturation condition of $g_e \mu_B B_{sat} = 2\hbar\omega_c^{sat}$ and the change of the band fillings $\hbar\omega_c^{sat} = \frac{\hbar^2(k_{Fz1}^{\downarrow,sat})^2}{2m_e}$, $2\hbar\omega_c^{sat} = \frac{\hbar^2(k_{Fz0}^{\downarrow,sat})^2}{2m_e}$ and $\hbar\omega_c^{QL} = \frac{\hbar^2(k_{Fz0}^{\downarrow,QL})^2}{2m_e}$ respectively, we arrive to the formula between the critical fields

$$B_{QL} = (1 + \sqrt{2})^{\frac{2}{3}} B_{sat}. \quad (4.19)$$

In the quantum limit, the degeneracy grows causing the Fermi level to fall monotonously to zero³ as

$$E_{F,B} = (2\pi)^2 N_e^2 \frac{\hbar^2}{2m_e} \left(\frac{h}{eB} \right)^2, \quad (4.20)$$

³Defined in this context as the bottom of the lowest lying Landau level of the conduction band ($k_z = 0$).

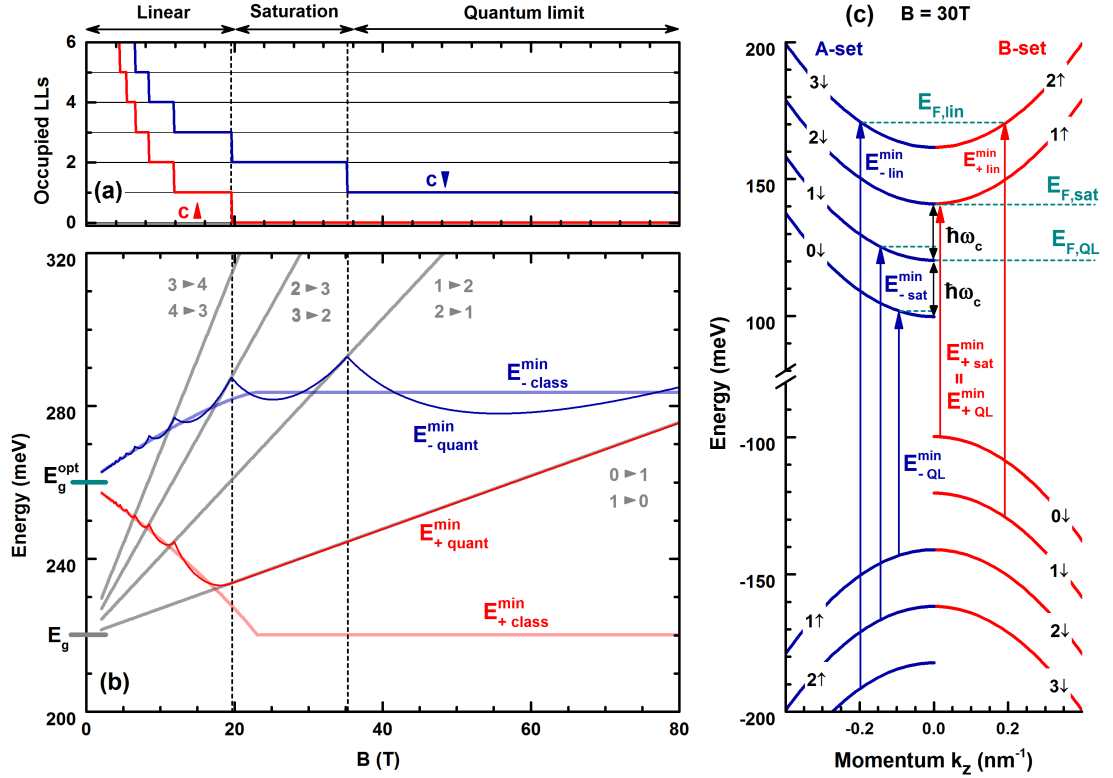


Figure 4.9: A simulated development of the minimal transitions E_+^{\min} , E_-^{\min} as a function of the magnetic field for $E_{F0} = 20$ meV presents three kinds of regime in a dependence on the Landau level occupation of the conduction band. In the linear stage the splitting matches with the classical model. The quantization effects begin to occur when 2^\downarrow is emptied and the splitting is saturated. In the asymptote of the quantum regime, $E_{F,B}$ approaches zero and the minimal transitions become equal $E_{+,QL}^{\min} = E_{-,QL}^{\min}$ as in the beginning for the zero field (for full electron-hole symmetry).

and the both transitions e_+ , e_- asymptotically converge to $L_{1 \rightarrow 0}^A$ and $L_{0 \rightarrow 1}^B$, as is manifested in the simulation in the Fig. 4.9. Such regime continues until the inverted zeroth modes cross at the critical field B_c .

Due to the peculiar structure of the Landau levels (see appendix 9) in the form of mutual pinning between the subsets $E_{A,n,E}$, $E_{B,n+1,E}$ no sizeable effects of the quantization in the spin polarization are visible because the both levels of the A and B set are emptied simultaneously at $B_n < B_{sat}$ for a given index n . This is supported by the fact that $E_{F,B}$ develops continuously in 3D systems which smears out the quantum oscillations of E_+^{\min} , E_-^{\min} transitions.

Spin polarization observed in NMR and Shubnikov-de Haas oscillations

Besides the saturation effect observed in the splitting of the absorption edge or for the quench of the photoluminescence, the net spin polarization of electrons also affects the Knight shift in the NMR and Shubnikov-de Haas oscillations. The polarization depends on the initial Fermi level and magnetic field, therefore the specific property of bismuth selenide $g_e = g_h$ is not necessary needed for the later phenomena as it is demonstrated on the n-type sample with $E_F = 20$ meV. The transport measurement showed SdH

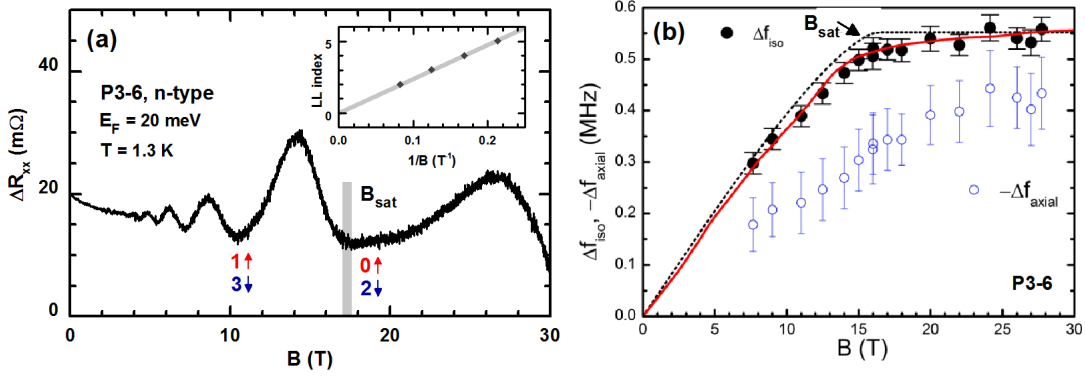


Figure 4.10: (a) A Shubnikov-de Haas signal depicts the oscillation related to the full spin polarization of the electron gas. The onset of the last oscillation signifies that the quantum limit was not yet reached. The inset of the $1/B$ -plot hints the Landau level indexation. (b) A Knight shift observed in ^{209}Bi NMR on the same sample clearly shows the saturation caused by the full spin polarization of the conduction electrons. The anisotropic axial component was subtracted (Adopted after [120]).

oscillations with the frequency $B_f = 20$ T between 4 and 15 T (Fig. 4.10a). The concentration $N_e = 7.5 \times 10^{17} \text{ cm}^{-3}$ was calculated using the SdH frequency and effective mass. The SdH signal ΔR_{xx} exhibits a minimum for $B_{sat} = 18$ T that corresponds to the depletion of the degenerate Landau levels $0^\uparrow, 2^\downarrow$. The quantum limit, when 1^\downarrow becomes de-occupied, is represented in the sequence of the SdH oscillations as the last minimum and its onset appears probably around 33-35 T as is predicted by the eq. (4.19).

In NMR, the resonant frequency f_0 of the ^{209}Bi nuclei with $I = \frac{9}{2}$ is split due to the quadrupolar coupling into nine satellites that are sensitive to the spin polarization of the surrounding conduction electrons [120]. The magnitude of the Knight shift Δf from the bare frequency of bismuth depends on the carrier density, polarization rate δN_e and temperature. Its isotropic component undergoes an analogical saturation behaviour as it was observed for the case of the absorption edge splitting (or Faraday rotation as shown in the next section, eq. (4.31) and it comes at the same field B_{sat} as the minimum in the SdH signal occurs (Fig. 4.10b). Besides, another extracted information from the temperature dependence of Δf at a fixed field was an activation energy E_A of the carriers thermally generated over the bandgap which further contribute to the spin polarization. The value of E_A matches with the result obtained from our optical studies.

4.5 Interband Faraday rotation

Derivation of the Verdet constant

The dichroic absorption at energies E_+^{\min}, E_-^{\min} causes a difference in the dielectric functions $\varepsilon_+, \varepsilon_-$ that gives rise to the interband Faraday rotation (FR). The Faraday rotation is observable in the transparent window $\hbar\omega_p < \hbar\omega < E_g^{opt}$. The formula (3.24)

for the Faraday angle Θ_F can be rewritten for a range of the weak absorption as

$$\Theta_F(\omega) = \frac{\omega d}{4c_0 \bar{n}} (\text{Re } \varepsilon_+(\omega) - \text{Re } \varepsilon_-(\omega)), \quad (4.21)$$

where $\bar{n} = \frac{1}{2}(n_+ - n_-)$ [124]. For the case of a two-band model the interband dielectric contribution reads

$$\text{Im } \varepsilon(\omega) = \frac{1}{4\pi\varepsilon_0} \left(\frac{2\pi e^2}{m_0\omega} \right)^2 |P_{cv}|^2 D_j(\hbar\omega), \quad (4.22)$$

where P_{cv} is a momentum matrix element [35]. The joint density of states $D_j(\hbar\omega)$, in an analogy to the expression (4.13), holds the form

$$D_j(\omega) = \frac{2}{(2\pi)^3} 4\pi \left(\frac{2\mu}{\hbar^2} \right)^{\frac{3}{2}} \frac{\sqrt{\hbar\omega - E_g}}{2}, \quad (4.23)$$

where μ is a reduced mass that for the anisotropic case gives $\mu = \mu_{\parallel}^{\frac{1}{3}} \mu_{\perp}^{\frac{2}{3}}$ [35]. In Bi_2Se_3 the role of the in-plane reduced mass μ_{\perp} is played by the Dirac mass m_D and the out-of-plane component $\frac{1}{\mu_{\parallel}} = \frac{1}{m_e^{\parallel}} + \frac{1}{m_h^{\parallel}}$ can be obtained from the Tab. 4.2 assuming the full electron-hole symmetry $m_e^{\parallel} = m_h^{\parallel}$. The Pauli-blocking is represented by the Heaviside function $\theta(\hbar\omega - E_g^{\text{opt}})$ through the Moss-Burstein shifted optical gap that splits up in the magnetic field into the transitions $E_+^{\text{min}} = E_g^{\text{opt}} - E_s$, $E_-^{\text{min}} = E_g^{\text{opt}} + E_s$ for circularly right and left polarized light. After the insertion of the joint DOS into the eq. (4.22) and assuming $|P_{cv}|^2 = 2m_0v^2$ for the Hamiltonian (4.1), we obtain an expression

$$\text{Im } \varepsilon_{\pm}(\omega) = \frac{A}{(\hbar\omega)^2} \sqrt{\hbar\omega - E_g} \theta(E - E_g^{\text{opt}} \pm E_s) \quad (4.24)$$

with a constant

$$A = \frac{\sqrt{2}e^2v^2\mu^{\frac{3}{2}}}{\varepsilon_0\pi\hbar^5}. \quad (4.25)$$

The real part of the dielectric function can be computed using the Kramers-Kronig relation as

$$\text{Re } \varepsilon_{\pm}(\omega) = \frac{2}{\pi} \mathcal{P} \int_{E_g^{\text{opt}} \pm E_s}^{\infty} \frac{\sqrt{z - E_g}}{z(z^2 - (\hbar\omega)^2)} dz. \quad (4.26)$$

The resulting rotation angle is acquired from the formula (4.21) as

$$\Theta_F(\omega) = \frac{A\omega d}{2\pi c_0 \bar{n}} \int_{E_g^{\text{opt}} - E_s}^{E_g^{\text{opt}} + E_s} \frac{\sqrt{z - E_g}}{z(z^2 - (\hbar\omega)^2)} dz. \quad (4.27)$$

In general, the Verdet law describes the situation of the linear Faraday rotation, which is usually conditioned to low magnetic fields with an angle following

$$\Theta_F(\omega) = V(\omega) B d, \quad (4.28)$$

where $V(\omega)$ denotes the Verdet constant dependent on the photon energy and d is the thickness of a slab. The integration in the eq. (4.27) simplifies for a tiny splitting

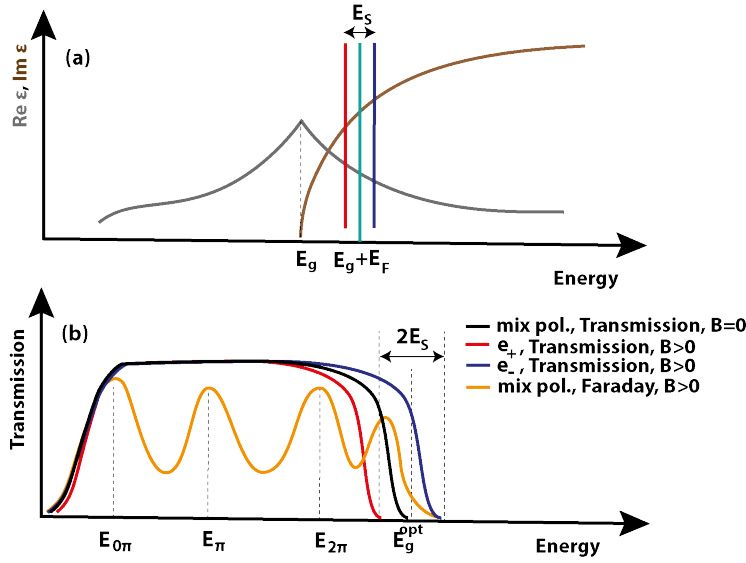


Figure 4.11: (a) The dielectric function of a direct band semiconductor with the initial Fermi level E_F . In the presence of the magnetic field the occupation of the spin up and down states in the conduction band is split by the Zeeman term E_s . (b) The consequence on the transmission spectrum is a splitting of the interband absorption edge. The dichroic onset alters the refraction index for the sub-bandgap excitations and gives rise to the Faraday rotation that causes a modulation pattern in the transmission for the fixed setting of polarizers and unpolarized (mixed) light. The maxima correspond to $\Theta_F(E_m) = \pi m$ multiples.

$E_s \ll E_F, E_g$ and $\hbar\omega < E_g^{opt}$. Then, the variable z can be set to E_g^{opt} on the interval of the length $2E_s = 2g_e\mu_B B$ and we receive

$$V(\omega) = v \frac{8e\alpha_0}{\pi\bar{n}} \frac{\sqrt{E_F E_g}}{E_g^{opt}} \frac{\hbar\omega}{(E_g^{opt})^2 - (\hbar\omega)^2}. \quad (4.29)$$

So, the Verdet constant scales in the reduced energy $x = \frac{\hbar\omega}{E_g^{opt}}$ as

$$V(\omega) \propto \frac{x}{1-x^2} \text{ for } 0 \leq x < 1. \quad (4.30)$$

The Faraday angle (4.28) is proportional to the net spin polarization $\delta N_e = N_e^\downarrow - N_e^\uparrow$ of the conduction band, since

$$\delta N_e \propto E_s D(E_F) \propto B\sqrt{E_F} \propto VB. \quad (4.31)$$

Remarks on the geometry of the Faraday rotation

The experiment of the Faraday rotation was arranged in the configuration of the fixed colinear polarizers with a specimen sandwiched in between (Fig. 2.3e). The Faraday angle is defined as a tilt of the outgoing polarization from the initial direction (Fig. 4.12). The incoming wave $\mathbf{E}_i = \mathbf{e}_y E_0 e^{i(kz - \omega t)}$ splits inside the slab into the two circularly

polarized modes

$$\mathbf{E}_{\pm} = \mathbf{e}_{\pm} \frac{E_0}{\sqrt{2}} e^{ik(n_{\pm} + i\kappa_{\pm})z - i\omega t} \quad (4.32)$$

that propagate in the medium correspondingly to their complex indices of refraction $n_{\pm} + i\kappa_{\pm}$. After a single passage through the thick sample they combine again forming the transmitted wave $\mathbf{E}_t = \tau_+ \mathbf{E}_+ + \tau_- \mathbf{E}_-$ with coefficients [90]

$$\tau_{\pm} = |\tau_{\pm}| e^{i\varphi_{\pm}} = \frac{4n_{\pm}}{(n_{\pm} + 1)^2} e^{ikn_{\pm}d} e^{-k\kappa_{\pm}d}. \quad (4.33)$$

In general, the exiting wave is elliptically polarized with a tilt of the main axis equal to the Faraday angle that is related to the phase difference as

$$\Theta_F = \frac{1}{2}(\varphi_+ - \varphi_-). \quad (4.34)$$

The degree of the ellipticity describes the ratio of the major a and minor b axes $\epsilon = \sqrt{(a^2 - b^2)/a^2}$ as

$$\epsilon = \frac{|\tau_+| - |\tau_-|}{|\tau_+| + |\tau_-|} \approx \frac{1}{2}(\kappa_- - \kappa_+)kd. \quad (4.35)$$

The refractive index n for Bi_2Se_3 was calculated from the Fabry-Perot modulations (Fig. 4.5b) and it can be sufficiently related with the mean value \bar{n} of the eq. (4.21). The transmission of the 10 μm -thin sample is in the limit of $\kappa \ll n$

$$T = \frac{(1 - R)^2}{(1 - R)^2 + 4R \sin^2(nd)} \quad (4.36)$$

with the use of reflectivity rate

$$R = \frac{|n - 1|^2}{|n + 1|^2}. \quad (4.37)$$

After the averaging over the modulations we get

$$T \approx \frac{2n}{n^2 + 1} = 0.35. \quad (4.38)$$

that corresponds with the measured data (Fig. 4.5a).

For the 225 μm thick sample without the interference fringe the residual absorption $A = e^{-2k\kappa d}$ becomes important and the transmission is given as $T = 1 - R - A \approx 0.1$ [125]. The transmittance function of the co-linear polarizers is $T \sim \cos^2 \Theta_F$ and their fixed alignment allows to read out the Faraday angle in the discrete points of minima, maxima or inflexions and to interpolate among them. So, the minima correspond to the values $\Theta_F = \pi(m + \frac{1}{2})$ and maxima to $\Theta_F = \pi m$ for $m = 0, 1, 2, \dots$. The formula (4.21) tells that the rotational angle depends inversely on the ratio of d/λ . Thus, for a fixed retardation length d and known wavelengths λ , we can extract several values of Θ_F from the each FTIR transmission spectrum recorded at a given field. In the range of the validity of the linear law (4.28), the values of the Verdet constant (4.14) collapse on the same curve for any magnetic field.

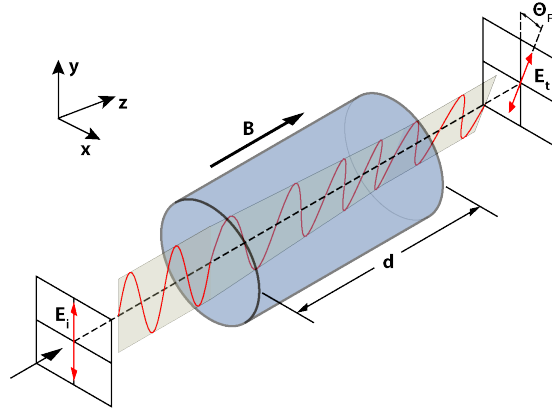


Figure 4.12: A scheme of the Faraday rotation for a non-absorbing medium [126]. An incoming linearly polarized wave is in the material decomposed into the circular polarization modes \mathbf{e}_+ , \mathbf{e}_- that traverse through the slab with the distinct refraction indices n_+ , n_- and thus with the gradual development of the mutual phase shift $(\varphi_+ - \varphi_-)$. At the exit of the sample, the polarizations modes are superimposed again and the final linear polarization is sloped by an angle Θ_F . The situation can be imagined as a gradual rolling of the polarization tilt. In the case of the absorbing medium the outgoing wave has an elliptical polarization with the main axis rotated by Θ_F .

Discussion of the experimental results

As it was analysed in the sec. 4.4, the circular dichroism experiences the three successive stages - linear regime, saturation and quantum limit that are responsible for the distinct behaviours of the Faraday rotation. The linear regime is characteristic with the spin-splitting proportional to the magnetic field within the derived model (4.29) for the Verdet constant. Then, the full spin polarization saturates the splitting of the absorption edge and stops further development of the rotation. In the quantum limit as k_z goes to zero the transition E_-^{min} approaches the $E_{1 \rightarrow 0}^A$ which is degenerated with $E_+^{\text{min}} = E_{0 \rightarrow 1}^B$. In general, the Faraday angle (4.21) can be expressed using the Krammers-Kronig relation in the form

$$\Theta_F(\omega) \propto \frac{2\omega}{\pi} \mathcal{P} \int_0^\infty \frac{z}{z^2 - \omega^2} (\text{Im } \varepsilon_+(z) - \text{Im } \varepsilon_-(z)) dz. \quad (4.39)$$

that depends purely on the difference of dissipative parts of the dielectric functions. In a simple picture considering just lowest lying Landau levels $0_{A,B}$ and $1_{A,B}$, we are able to imply the approximate behaviour of Θ_F in the quantum limit. The absorption is proportional to the joint density of states that in the quantized regime turns into the product of the out-of-plane 1D density $D_j(E) \propto \sqrt{E - E_g}$ and LL degeneracy ζ_{2D} . Due to the discrepancy of ε_\pm , the integration limits of eq. (4.39) reduce to an interval between 0 and $2E_F(B)$. For a given photon energy it turns out that the B-field dependency cancels out, since the Fermi level drops as B^{-2} , thus the Faraday angle remains constant.

However, the experimentally accessible regimes are currently the first two stages for $E_{F0} = 25$ meV with the saturation entering at $B_{\text{sat}}^{\text{exp}} \approx 23$ T (Fig. 4.13). The Faraday angle is encoded in the modulation pattern of the relative transmission T_B/T_0 with a possibility to be extracted for a given intraband energy close to E_g^{opt} using the

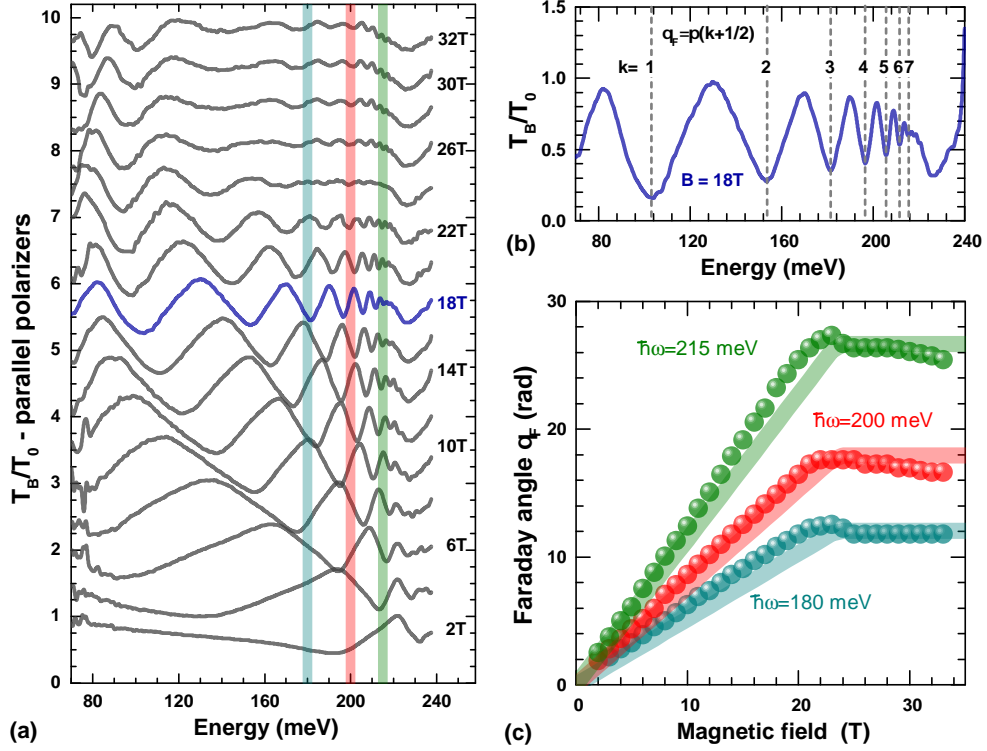


Figure 4.13: (a) The Faraday rotation observed in the form of the oscillations in the relative transmission spectra (vertically shifted by 0.6). The pattern of the the sub-bandgap excitations develops with the augmentation of the magnetic field for until the saturation is reached, then it stays constant. (b) The modulations correspond to the $\frac{\pi}{2}$ -multiples of the Faraday angle at certain values of energies for a given field. This allows to extract the Faraday angle for the selected photon energies close to the E_g^{opt} where the modulations are dense. The curves shows a clear linear trend followed by a plateau (c). The data matches with the classical model of the Verdet law up to the saturation (solid lines).

interpolation method between the discrete values of the extrema for known indexation. The $\Theta_F(B)$ curves consist of a sloped line followed by a plateau for $B > B_s$ that according to the equation (4.15) occurs at $B_{sat}^{th} \approx 25$ T. The Verdet constant (4.29) plays the role of the slope and can be reformulated purely using the saturation field instead of the Fermi energy as

$$V(\omega) = \tilde{A} \frac{v^2 \sqrt{B_{sat}}}{\bar{n} E_g^{opt}} \frac{\hbar\omega}{(E_g^{opt})^2 - (\hbar\omega)^2} \quad (4.40)$$

with a redefined constant $\tilde{A} = \frac{8e\alpha_0}{\pi} \sqrt{2^{\frac{1}{3}} \hbar e}$.

The correction for the full integration of (4.27) is not so significant in the respect to the precision of the deduced E_F , whose major uncertainty originates from the inhomogeneity of the electron concentration or from the large thickness shifting the absorption edge to the lower energies. Another inaccuracy arises from the isotropic approximation that does not influence the actual saturation field but has an impact on the reduced mass μ , since the out-of-plane effective mass is not exactly known but it could be estimated from the g-factor $g_{e,h}^{\parallel} = \frac{2m_0}{m_{\parallel}^D}$ as $m_{e,h}^{\parallel} = 0.2m_0$ in agreement to refs. [112, 120]

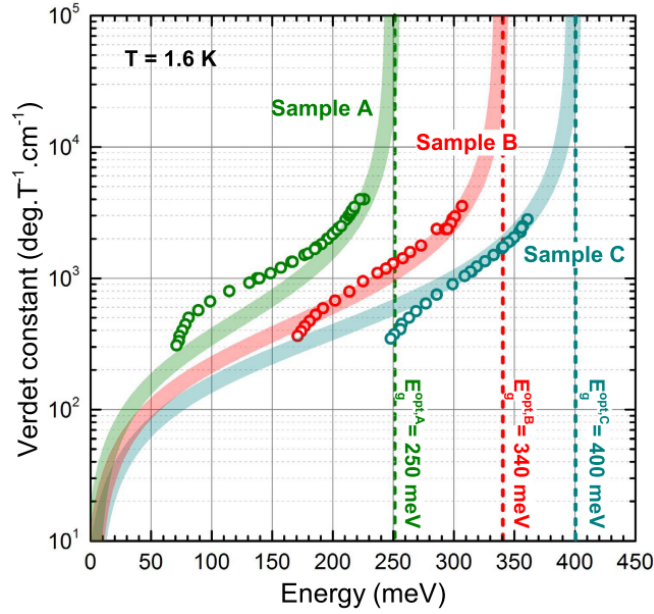


Figure 4.14: The Verdet constant measured in the linear regime of the low magnetic field was fitted by the model (4.29). The datasets on the three samples with the different doping show how the divergence is shifted to the higher energies with the increasing Fermi level.

(Tab. 4.2).

The amplitude of the modulations does not span fully between 0 and 1 (as it could be expected from the transmission function of the polarizers) due to the residual absorption within the gap that gives rise to the non-zero ellipticity. This effect enhances as the saturation is approached and leads to a considerable suppression of the modulations.

The Verdet constant depends on the parameters E_g , v , \bar{n} known from the preceding experiments and apart the Fermi level it does not contain any further tunable variables. So, the data for a series of samples with different carrier concentration may be compared with the theoretically expected behaviour (Fig. 4.14). The model is divergent for $\hbar\omega \rightarrow E_g^{opt}$ and its asymptote shifts according to the Fermi level. Oppositely, the Verdet constant goes to zero as $\hbar\omega \rightarrow 0$. For the photon energies 0.2-0.4 eV, the Verdet constant spans over $0.5\text{-}5 \times 10^3$ deg/T.cm that suggests a significant potential for a strong figure of merit defined as $\text{FM}(E) = V(E)/a(E)$ with $a(E)$ being the absorption coefficient. For the referential line $10 \mu\text{m}$ ($=125$ meV) of the CO_2 laser we obtain $\text{FM} \approx 20$ deg.T.cm $^{-2}$ assuming the attenuation of 50 cm^{-1} (Fig. 4.5 and [125]). The analogical behaviour with similar magnitudes is anticipated for the other representatives of the same material class such as Bi_2Te_3 , Sb_2Te_3 .

The main rotational mechanism is due to the occupational changes, where the doping is essential, exploiting the fact that the g-factors of the valence and conduction band are the opposite in their signs but equal in the absolute value. Any deviation from the theory, viewed as a tilt of the saturation plateau, can be explained by the factor $(g_h - g_e)\mu_B(B - B_{sat})$ as a consequence of the electron-hole asymmetry $g_e \neq g_h$ without requirements for any presence of free carriers. The Faraday rotation for the excitations with energies $\hbar\omega > E_g^{opt}$ has generally a complex behaviour that depends

on the actual structure of the Landau levels. This region was not investigated due to the considerable absorption of the thick samples.

For low energies close to the plasma edge, the contribution to the Faraday rotation due to the free carriers in a parabolic band should be taken into account

$$\Theta_F(\omega) = \frac{2}{3} \frac{e\alpha_0}{\pi} \frac{\sqrt{m_e} E_F^{\frac{3}{2}}}{n_\omega} \frac{Bd}{(\hbar\omega)^2} \quad (4.41)$$

as adjusted after eq. (3.25), but its significance was neglected since the dependence falls as ω^{-2} and the investigated energies lies above 0.1 eV.

The contribution from the cyclotron resonance of the surface state, as found on epitaxial layers [109, 110], was not observed in our case since the Fermi level is situated in the conduction band and the response can be sufficiently interpreted as originating in a bulk. Moreover, the surface FR is a constant function in energy and quantized in the way [103, 109]

$$\tan \Theta_F = \frac{2\alpha_0}{1 + n_s} \left(N_t + \frac{1}{2} + N_b + \frac{1}{2} \right), \quad (4.42)$$

where n_s is the index of refraction of the substrate and N_t, N_b are the highest fully filled LLs of the top and bottom surfaces of the film. Its value is in orders of few or maximally tens of mrad independently of the slab thickness for bulky crystals or on the number of quintuple layers for the case of thin epitaxial samples. The protected surface states can become accessible when the Fermi level is downshifted sufficiently into the gap (e.g. by Cu doping combined with a deposition of a dielectric top layer).

5. Conclusion

Cadmium arsenide

In the first part of the work we investigated Cd_3As_2 by the means of magneto-optics. The material was recently identified as a candidate for the realization of a genuine 3D Dirac semimetal [55–58, 82] with the cone in the conduction band extending over hundreds of meV. We verified the existence of this cone by observing the characteristic \sqrt{B} -dependence of the cyclotron modes in the magneto-reflectivity for the two respective spin-sets (Fig. 3.16). But, we also concluded from the analysis of the behaviour observed in the quantum limit that the system at the investigated energy scale needs to be interpreted as of the Kane-type [25] with a single realization of the cone not as the symmetry-protected Dirac type occurring in a pair. Such findings are in the agreement with the works done in the past but they also raise doubts about the interpretation of the recent ARPES studies. The deduction was made from the consideration of the reasonable values of the bandgap and velocity. This was further supported by the simulation of the Fermi level evolution (Fig. 3.18 and 3.17), whose initial value was independently confirmed from the zero-field conductivity (Fig. 3.7).

To resolve the controversy between the predicted realization of the Dirac cones [15, 54] for Cd_3As_2 and the observed response of the Kane-type we suggest a scenario that includes the coexistence of the both type of the structures at the different energy scales. The Kane fermions act at the larger scale in a six-band approximation of the spin-degenerated electron, light hole and heavy hole bands. In contrast, the Dirac electrons are present at the smaller scale due to the intersection of the inverted light-hole band with the heavy holes caused by the crystal field splitting that originates in the tetragonal distortion of the crystal lattice. This idea is based on the simplified analogy with zinc-blende semiconductors (Bodnar model), developed for this material in the past and also widely used for the explanation of the numerous preceding experimental results. The Bodnar model reduces for the vanishing crystal field splitting and bandgap to the case of the gapless Kane model. The role of the flat heavy-hole band in the Kane model becomes essential for the basic structure of Landau levels as well as for the enhancement of the interband optical absorption due to the singularity in the joint density of states.

This leads us to the proposition that the substructure of the Dirac cones could be artificially engineered via straining of a thin $\text{Hg}_{1-x_c}\text{Cd}_{x_c}\text{Te}$ layer grown on a substrate with an appropriate lattice mismatch [127]. Another approach is offered by alloying of Cd_3As_2 with zinc or phosphorus [51].

Being limited by combination of a strong absorption, surface sensitive plasma edge and quality of the material we were able to observe the flat-to-cone interband transitions in the Pauli-blocked transparent window. The line assignment is fully consistent with the model and the result of the fit gives the estimations of the band parameters. The narrow inverted gap was confirmed with a good precision and agrees to the main works done in the past. However, the error of the additional crystal field parameter δ is

large and the existence of the tiny Dirac cones is not yet sufficiently verified. The experimental conditions are currently limited to rather heavily n-doped bulky samples with the Fermi level lying in the conduction band far above a possible point of the cone coalescence (Lifshitz gap) and all extrapolation to the lower lying bands thus needs to be treated carefully. So, the band structure remains after forty years of the ongoing research still partially undetermined, in contrast to the case of well understood wide-gap semiconductors. It is expected that Landau level spectroscopy carried out on epitaxial layers finally resolves all questions. Importantly, our findings brought a qualitative insight and proves that the infrared Fourier spectroscopy coupled to the quantizing field remains an important technique for the exploration of the electronic band structures.

Bismuth selenide

This material can be considered as a cartoon picture semiconductor with the inverted band ordering. The conduction and valence bands have both a p-like nature with the approximately symmetrical effective masses and they are well separated from the higher bands [91]. Besides, the peculiar condition (eq. 4.3) between the band parameters is obeyed for the topological Bernevig, Hughes and Zhang Hamiltonian and it translates into a particular pinning between the Landau level fancharts of the distinct spin sets. Such property could be expressed in the way that the cyclotron gap is twice as large as the spin gap or by the fact that the electron and hole g-factors are equal within the same A, B family. This leads to the same splitting of the interband transitions for an intrinsic system. However, for the extrinsic case the splitting gives rise to a strong dichroism due to the occupational changes that block the onsets of the interband absorption of the circularly polarized modes of light. In this work, we observed the bulk dichroic behaviour evinced as a splitting of the absorption edge and the linear Faraday rotation in the low magnetic field. We demonstrated that the optical response can be explained using a simple model of the 3D electron gas with the parabolic dispersion. The Verdet law described by eq. (4.29) represents a dominant rotational mechanism and strongly depends on the initial Fermi level through the Moss-Burstein shift (Fig. 4.14). The total spin polarization triggers a special regime of the saturation in higher fields (Fig. 4.13) which is still able to be explained using a classical picture. Although the quantum oscillations are already resolved in the transport measurements, their effect on optics remains minor in three dimensions due to the characteristic LL structure (level pinning). In the quantum regime the Pauli-blocking becomes negligible and dichroic absorption progressively diminishes, while the Faraday rotation remains saturated being sensitive only to the net spin polarization.

We observed a direct gap magneto-photoluminescence in the challenging middle infrared region that is fully consistent with the results obtained from the transmission on the thin slabs (Fig. 4.3) and with the previous Landau level study [73]. From the perspective of the ARPES [32,92–94] the full agreement can be found, if the Dirac point of the surface states is repositioned with respect to the bulk bands from the midgap (in

the interpretation of the camel-back valance band) to the top of the purely parabolic valence band. The bandgap does not represent only a parameter in the BHZ-model but has a deeper significance for the electron-hole excitations in the analogy with the massive Dirac particles obeying the Einstein formula (4.6). The suppression of the PL emission observed in the dependence on the magnetic field is understood as a direct consequence of the the spin-splitting affecting the electron population in the conduction band (Fig. 4.8).

It turned out that the Bi₂Se₃ layers host various physical phenomena in the dependence on the thickness and doping. While the slab with the thickness in the order of magnitudes of 0.5-100 μm are ideal for the investigation of the absorption edge, plasma frequency and bulk Faraday rotation. The thinner layers (10-500 nm) are more suitable for the investigation of the Landau level structure and the effects of the 2D quantum confinement that probably give rise to the camelback structure of the valence band observed by the surface techniques [98]. For the films comprising of few quintuple layers the bridge between a 2D and 3D topological insulator can be traversed [128] and moreover the band ordering could be also restored from the inverted to normal.

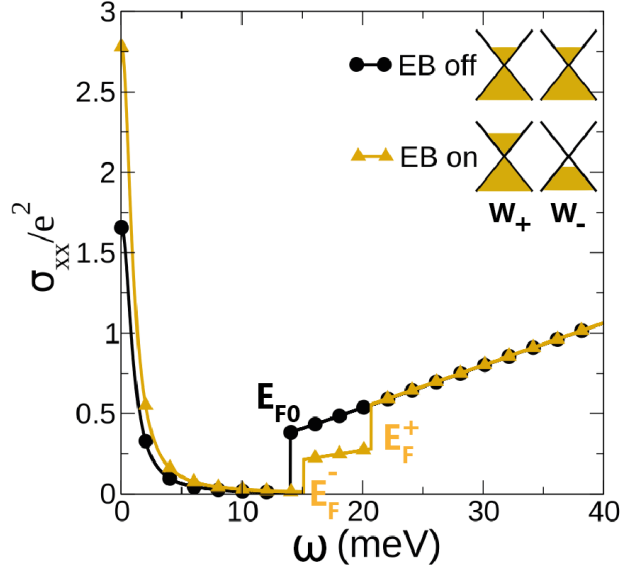
Prospect

The group of materials with relativistic-like electrons probably represents the most active field in infrared magneto-spectroscopy and it steadily encompasses emerging systems with unconventional band structures. In the context of Dirac semimetals, the attention is mainly focused on the following representatives HgCdTe, PbSnSe, ZrTe₅, Cd₃As₂, Na₃Bi, TaAs, NbAs and MoTe₂. The goal is aimed to investigate the form of conical structures, its energy scale, shape (electron-hole symmetry, tilt). The characterization is done in terms of parameters (gap, velocity) with respect to a given effective Hamiltonian. Another important issue is to resolve the protection of the charge neutrality (nodal) point by a symmetry element (n-fold axis, inversion, time-reversal) against perturbations and classify it in the connection to the insulator-semimetal phase transitions. Such methodology became a necessary prerequisite to find out an ideal system with widely extending cones where the low-energy description using relativistic approach is well obeyed. Having a convenient representative, other novel phenomena (in an analogy to high energy physics) can be further studied, such as Klein tunneling, jittering, chiral magneto-effects.

For instance, in order to briefly illustrate the physical picture of the latest case, let us assume a 3D Weyl semimetal obtained from the Dirac structure by breaking the time-reversal symmetry. This system is characteristic by an existence of electrons with different chiralities (spin) in the vicinity of the related Weyl points. An additional presence of the co-parallel non-quantizing E, B -fields give rise to the change in the population of chiral particles between the both valleys (also known as E, B -pumping). The kinetics of this process is governed by a continuity equation for the electron density N_χ [130]

$$\frac{\partial N_\chi}{\partial t} + \nabla \cdot \mathbf{j} = \chi \frac{e^2}{\hbar^2 c} (\mathbf{E} \cdot \mathbf{B}) - \frac{\delta N_\chi}{\tau} \quad (5.1)$$

Figure 5.1: Realization of the chiral anomaly in Weyl semimetal under the application of the co-linear electric and magnetic field in the limit of the classical regime. The interband optical conductivity at the absence of the fields is linear with a step-like onset due to the Pauli blocking related to Fermi level E_{F0} . When the E, B -fields are switched on, the charge is pumped from the Weyl point W_- to W_+ . This causes a splitting of the corresponding absorption edges in a form of the double-step. The missing interband spectral weight is transferred to the Drude peak [129].



with the following definition of the charge current

$$\mathbf{j}_\chi = - \int \frac{d\mathbf{k}}{(2\pi\hbar)^2} (\mathbf{v} + e\mathbf{E} \times \mathcal{F}_\chi + e(\mathcal{F}_\chi \cdot \mathbf{v})\mathbf{B}), \quad (5.2)$$

where \mathcal{F}_χ is the Berry curvature at the valley χ . With the triggered fields the electric charge is driven from one valley to the second, until the pumping is cutoff by a relaxation process with scattering τ . Under the assumption of the conservation of the total number of carriers, the system arrives to a steady state with the distinct Fermi levels [129]

$$E_F^\chi = \left(E_{F0}^3 + \chi \frac{3}{2} e^2 \hbar v^3 \tau \mathbf{E} \cdot \mathbf{B} \right)^{\frac{1}{3}}. \quad (5.3)$$

This situation can be manifested experimentally in optics as a splitting in the onsets of the Pauli-blocked interband absorption (see the profile of the optical conductivity in Fig. 5.1). However, the application of the quasi-static electric field can be challenging due to the significant charge screening at short distances for a bulk semimetallic phase.

6. Perturbative approach for (112)-oriented Bodnar Hamiltonian

In this appendix, we introduce a procedure that was used for the computations of Landau level energies for an arbitrarily oriented Bodnar Hamiltonian (3.8) with the application on the magneto-optical data measured on the naturally grown (112)-faces of Cd₃As₂ crystals [71]. In the tilted magnetic field with a unit vector $(\sin \theta, 0, \cos \theta)^\top$, the commutation relations satisfy

$$[k_x, k_y] = -\frac{i}{l_B^2} \cos \theta, \quad [k_x, k_z] = 0, \quad [k_y, k_z] = -\frac{i}{l_B^2} \sin \theta. \quad (6.1)$$

To handle the quantization easily and to use the ladder algebra, it is necessary to introduce new rescaled and rotated momenta coordinates q_x, q_y, q_z via a transformation

$$\begin{pmatrix} q_x \\ q_y \\ q_z \end{pmatrix} = \begin{pmatrix} \frac{P_\perp}{P} \cos \xi & 0 & -\frac{P_\parallel}{P} \sin \xi \\ 0 & \frac{P_\perp}{P} & 0 \\ \frac{P_\perp}{P} \sin \xi & 0 & \frac{P_\parallel}{P} \cos \xi \end{pmatrix} \begin{pmatrix} k_x \\ k_y \\ k_z \end{pmatrix} \quad (6.2)$$

in which the new commutation relations take form

$$[q_x, q_y] = -\frac{i}{l_B^2} \frac{P_\perp^2}{P^2} \cos \xi, \quad [q_x, q_z] = 0, \quad [q_y, q_z] = \frac{i}{l_B^2} \frac{P_\perp^2}{P^2} \sin \xi. \quad (6.3)$$

By a convenient choice of P, ξ values

$$P = \sqrt{P_\perp^2 \cos \theta}, \quad \tan \xi = \frac{P_\perp}{P_\parallel} \tan \theta, \quad (6.4)$$

the commutations convert to its standard version (1.24) and the Hamiltonian (3.8) undergoes a unitary transform $H_\xi = U_\xi H U_\xi^{-1}$ with the resulting matrix

$$\begin{bmatrix} E_g & P_\perp q_+ & P_\perp q_- & 0 & 0 & 0 & 0 & P_\parallel q_z \\ P_\perp q_- & -\frac{\delta \sin^2 \xi}{2} & -\frac{\delta \sin^2 \xi}{2} & 0 & 0 & 0 & 0 & \frac{\delta \sin 2\xi}{2\sqrt{2}} \\ P_\perp q_+ & -\frac{\delta \sin^2 \xi}{2} & -\frac{\delta \sin^2 \xi}{2} - \frac{2}{3} \Delta & \frac{\sqrt{2}}{3} \Delta & 0 & 0 & 0 & -\frac{\delta \sin 2\xi}{2\sqrt{2}} \\ 0 & 0 & \frac{\sqrt{2}}{3} \Delta & -(\delta \cos^2 \xi + \frac{\Delta}{3}) & P_\parallel q_z & \frac{\delta \sin 2\xi}{2\sqrt{2}} & \frac{\delta \sin 2\xi}{2\sqrt{2}} & 0 \\ 0 & 0 & 0 & P_\parallel q_z & E_g & P_\perp q_- & -P_\perp q_+ & 0 \\ 0 & 0 & 0 & \frac{\delta \sin 2\xi}{2\sqrt{2}} & P_\perp q_+ & -\frac{\delta \sin^2 \xi}{2} & \frac{\delta \sin^2 \xi}{2} & 0 \\ 0 & 0 & 0 & \frac{\delta \sin 2\xi}{2\sqrt{2}} & -P_\perp q_- & \frac{\delta \sin^2 \xi}{2} & -\frac{\delta \sin^2 \xi}{2} - \frac{2}{3} \Delta & \frac{\sqrt{2}}{3} \Delta \\ P_\parallel q_z & \frac{\delta \sin 2\xi}{2\sqrt{2}} & -\frac{\delta \sin 2\xi}{2\sqrt{2}} & 0 & 0 & 0 & \frac{\sqrt{2}}{3} \Delta & -(\delta \cos^2 \xi + \frac{\Delta}{3}) \end{bmatrix} \quad (6.5)$$

After performing the quantization routine of the magnetic field, one concludes that no simple eight-component vector $\Psi = (\psi_j)_{j=1..8} = (a_{j,n} |n\rangle)$ can satisfy all ladder operations (1.25) at once and a more general ansatz for the each component of the

wavefunction ψ_j needs to be selected in the form

$$\psi_j = \sum_{n=0}^{N_{\max}} a_{j,n} |n\rangle . \quad (6.6)$$

When the solution is inserted to the eigenproblem $H\Psi = E\Psi$, we end up with the set of eight equations

$$\sum_{j=1}^8 \sum_{n=0}^{N_{\max}} H_{ij} a_{j,n} |n\rangle = E \sum_{n=0}^{N_{\max}} a_{j,n} |n\rangle . \quad (6.7)$$

If each equation is projected out to the each function $\langle n' |_{n'=1..N_{\max}}$ of the expansion (6.6), then the relations for coefficients $a_{j,n}$ are obtained

$$\sum_{j=1}^8 \sum_{n=0}^{N_{\max}} \langle n' | H_{ij} | n \rangle a_{j,n} = E \sum_{n=0}^{N_{\max}} a_{j,n} \delta_{n',n} . \quad (6.8)$$

So altogether, the set of $N_{\max} \times 8$ equations (6.8) provides energies of N_{\max} Landau levels for one of the eight bands.

By applying similar transform as in ref. [44] to the set (6.2), it is possible to obtain a single dispersion relation for the Landau level E_n with a standard form of the wavefunction $\psi_n = \sum_{i=1}^8 a_i |n\rangle_i u_i$

$$\begin{aligned} \gamma(E_n) = & \frac{\text{sgn} f_1(E_n)(2n+1)}{l_B^2} \sqrt{f_1(E_n)(\cos^2 \theta f_1(E_n) + \sin^2 \theta f_2(E_n))} \\ & + \frac{f_1(E_n) f_2 E_n}{\cos^2 \theta f_1(E_n) + \sin^2 \theta f_2(E_n)} k_z^2 \pm \frac{P_{\perp} \Delta}{3l_B^2} \sqrt{(E_n + \delta)^2 P_{\perp}^2 \cos^2 \theta + E_n^2 P_{\parallel}^2 \sin^2 \theta} \end{aligned} \quad (6.9)$$

for the corresponding sets spin up and down (\pm) that is valid only outside the interval of energies $-\tan \theta < f_1(E_n)/f_2(E_n) < 0$ which covers the region of the HH band for $\delta > 0$.

7. Selection rules

The intensity of inter-Landau level transitions observed in the experiment is determined by the selection rules which depend in general on the joint density of states, matrix element of the interaction, electron occupancy and the polarization of light. All those aspects are inherently contained in the Kubo-Greenwood formula (1.23) for the dynamical conductivity adjusted for the magnetic field [20, 131]

$$\sigma_{\pm}(\omega, B) = \frac{e^2 \zeta_{2D}}{\omega} \int \frac{dk_z}{2\pi} \sum_{n,m} \frac{\left| \langle \psi_{\beta} | v_{\mp} | \psi_{\alpha} \rangle \right|^2}{(E_{\beta} - E_{\alpha}) - \hbar\omega + i\Gamma} (f_{\beta} - f_{\alpha}) \delta(k_{z,\beta} - k_{z,\alpha}). \quad (7.1)$$

Importantly, the matrix elements of the velocity operator $v_i = \frac{1}{\hbar} \frac{\partial H}{\partial \pi_i}$ can be more conveniently expressed using the combination $v_{\pm} = \frac{1}{\sqrt{2}}(v_x \pm i v_y)$ for \mathbf{e}_{\mp} circular polarizations of light, since the k.p Hamiltonian naturally composes of terms including k_{\pm}, k_z, k^2 . The initial and final wavefunctions can be expressed as $\psi_{\alpha} = \sum_i a_i \phi_{n_i} u_i$ and $\psi_{\beta} = \sum_j a_j \phi_{n_j} u_j$ where $a_{i,j}$ are constant coefficients, ϕ_n are harmonic functions (1.32) of α, β -Landau levels and $u_{i,j}$ are Bloch functions of the Hamiltonian H . Then the matrix elements are evaluated as

$$\langle \psi_{\beta} | v_{\pm} | \psi_{\alpha} \rangle = \sum_i \sum_j a_j^* a_i \int \phi_j^* u_j^* \frac{\partial H}{\partial \pi_{\mp}} u_i \phi_i dr^3. \quad (7.2)$$

The outcome depends on the product of elements $a_j^* a_i$, which for the form of diagonal Hamiltonian with decoupled spin blocks is zero, signifying that in the Faraday geometry the allowed transitions take place within the same spin set. For the velocity operator a commutation relation $v_{\pm} = \mp \frac{l_B}{\hbar} [a^{\pm}, H]$ holds [132], which in the simplest case yields $\langle \psi_{\beta} | v_{\pm} | \psi_{\alpha} \rangle = -\frac{l_B}{\hbar} (E_{\alpha} - E_{\beta}) \langle \psi_{\beta} | a_{\pm} | \psi_{\alpha} \rangle$ that is non-zero if $\beta = \alpha + 1$, which is the well-known selection rule $n - 1 \rightarrow n$ for \mathbf{e}_- polarization. The analogical situation holds for the \mathbf{e}_+ polarization with $n + 1 \rightarrow n$. However, in a multi-band Hamiltonian the result is less straightforward, since the Landau levels are formed as superpositions from several harmonic functions, and the operator v_{\pm} is a matrix.

The joint density of states in (7.1) consists of an in-plane part degenerated by a common factor ζ_{2D} for the each LL and with a peak if the photon energy matches $E_{\beta} - E_{\alpha}$ as a denominator in the sum (7.1) implies. The second contribution comes from the out-of-plane dispersion that is described by the condition of equal k_z momenta. As a result the sharp spikes appear in the conductivity added to the linear zero-field background (Fig. 7.1a).

In two dimensions the Landau levels are discrete states whereas in 3D the residual non-quantized dimension gives rise to the LL subbands whose dispersion affects the lineshape of the observed LL transition. For parabolic bands the joint density of states of the residual dimension is hyperbolic E^{-1} but for conical bands it is a constant, c.f. Fig. 1.4. Hence, a transition between the parabolic bands is resonantly enhanced for $E_F = 0$ due to the singularity at $k = 0$ but for the linear case it is independent of E_F .

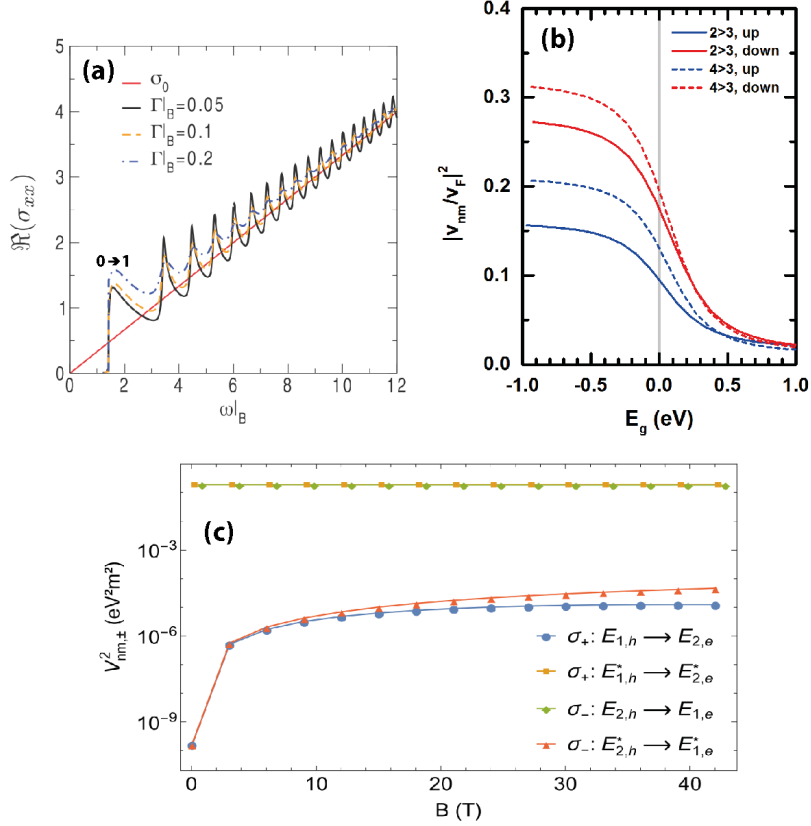


Figure 7.1: (a) A real part of the optical conductivity (in units $e^2/8\pi l_B$) for a 3D Dirac system with $E_F = 0$ and for several values of broadening Γ [131]. The red line shows the conductivity in the absence of the magnetic field. In the quantizing field the intercone transitions appear as sharp peaks superimposed onto σ_0 with tails oriented to high energies. The first peak signifies cyclotron resonance $0 \rightarrow 1$. The x -axis is scaled in ωl_B units which means that the patterns remains intact upon a sweep of the field. (b) Flat-to-cone transitions with $n_f = 3$ for the 3D Kane system show comparable intensities given by the velocity matrix element in a wide span of the bandgap energies E_g . The Fermi velocity was chosen as 10^6 m/s. (c) In contrast to the former case, one half of all interband transitions for the topological Hamiltonian (4.1) of Bi_2Se_3 is completely suppressed. For the each spin set either the transition $n - 1 \rightarrow n$ or $n + 1 \rightarrow n$ are realized exclusively [73].

As an example, we can address a situation of the cyclotron resonance in the quantum limit (sec. 3.8) for a Dirac and Kane dispersion in 3D, where the Dirac model is featured with the 0-th linear level but the Kane model has parabolic LL subbands for $n = 1$.

The Dirac and Kane models exhibit similar amplitudes of the interband transitions for both series $n \rightarrow n \pm 1$ that develop with a bandgap energy E_g . The same holds also for the flat-to-cone transitions. However, a peculiar structure of the Bi_2Se_3 Hamiltonian (4.1) implies a complete suppression of one of the selection rules $\Delta n = \pm 1$ by several orders of magnitude due to the mass term M , when a relatively small gap is opened [73] (Fig. 7.1b,c).

8. On formation of Dirac cones

The situation when Dirac and Kane massless electrons appear on two different scales, as it was proposed in the chap. 2, is not particular to the studied material Cd_3As_2 but it could be engineered by an artificial strain in thin layers deposited on a substrate with a different mismatch of the lattice constants in a condition of the inverted band regime, as for example in $\text{Hg}_x\text{Cd}_{1-x}\text{Te}$ with $x < 17\%$ [127]. Here, the layer should not overgrow a critical thickness $d_{\text{max}} < 150$ nm necessary for the strain relaxation. On the other hand, a minimal film thickness is required to remove two-dimensional quantum confinement. With the increasing thickness the individual subbands of the quantum well become densely arranged until they form a quasi-discrete continuum E_n in the out-of-plane direction for $d_{\text{min}} > 70$ nm according to the formula for $E_n = \frac{\hbar^2 \pi^2 n^2}{2m_e d^2}$ at $k_z = 0$. In a regime $d_{\text{min}} < d < d_{\text{max}}$, the distortion is characterized by a diagonal strain tensor ε with the in-plane components $\varepsilon_{xx} = \varepsilon_{yy} = \frac{a_S - a_L}{a_L}$ reflecting the mismatch between the lattice parameters of the substrate a_S and the epilayer a_L [133]. The z -component is proportional to the in-plane strain via elastic parameters $\varepsilon_{zz} = -2\frac{C_{12}}{C_{11}}\varepsilon_{xx}$. So, for instance, when the substrate forces the layer to laterally elongate, the height is being compressed. The deformation transfers to the band structure through the Bir-Pikus Hamiltonian added to the unperturbed Hamiltonian. In the linear approximation, the LH and HH bands shift by factor $\pm V_\varepsilon = \frac{1}{2}b(\varepsilon_{xx} + \varepsilon_{yy} - 2\varepsilon_{zz}) = b(1 + \frac{C_{12}}{C_{11}})\varepsilon_{xx}$ that opens either a positive gap or gives rise to the band crossing (positioned on the remaining C_4 -axis) in a dependence on the sign of the strain [134].

Experimental demonstration of strain-induced changes in the band structure can be documented on the work [82] where cadmium arsenide layer with thickness 200 nm was deposited on GaAs substrate with the lattice cell $a_0 = 5.65$ nm inducing a theoretical strain $\varepsilon_{xx} = 4\%$. The position of the cyclotron resonance $1^\downarrow \rightarrow 2^\downarrow$ was shifted by 20 meV at 10 T. In a study [135], the dependence of the volume pressure imposed on bulk samples showed a shift of the SdH oscillations and the related geometrical phase. The presence of the gap between LH and HH and an ambipolar transport character can be also measured directly on gated structures [136].

The problem can be further extended to the case when negative E_g is large and the inverted bands are purely parabolic, as for example in HgTe with $E_g = -0.3$ eV. The band crossing can not be regarded as linear anymore, since it results from the intersection of the parabola with the flat band. The remote (downshifted) E band can be directly neglected from the minimal description of the LH and HH bands, which on the other hand requires to include the Luttinger terms with parameters $\gamma_1, \gamma', \gamma'', \kappa$. The Hamiltonian in the presence of the magnetic field becomes particularly simple [137, 138]

$$H_{\gamma, \uparrow} = \hbar\omega_c \begin{pmatrix} (\gamma_1 + \gamma')(n + \frac{1}{2}) + \frac{3}{2}\kappa + V_\varepsilon & -\sqrt{3}\gamma''a^2 \\ -\sqrt{3}\gamma''a^2 & (\gamma_1 - \gamma')(n + \frac{1}{2}) - \frac{1}{2}\kappa - V_\varepsilon \end{pmatrix} \quad (8.1)$$

with an analogical structure for the spin down. The mutual coupling between spins was suppressed.

According to ref. [51], it was also foreseen that the Dirac cones between HH and LH bands can also occur as a result of the composition tuning within $\text{Cd}_3\text{As}_{2-x}\text{P}_x$ alloy. The compound Cd_3P_2 has a normal band ordering with $E_g = 0.53$ eV [48, 50]. The ab-initio model [51] anticipates the existence of the two critical concentrations x_c - one for the formation of the Dirac cones and the second for the E-LH band inversion.

The time reversal symmetry can be effectively broken at the low magnetic field via the incorporation of few percents of a paramagnetic impurity such as Mn to turn four-fold degenerated Dirac cones into two pairs of Weyl cones. The $3d^5$ electrons brings an additional exchange interaction

$$E_{ex} = - \sum_{R_n} J(\mathbf{r} - \mathbf{R}_n) \boldsymbol{\sigma} \cdot \mathbf{S}_n \quad (8.2)$$

that enhances the splitting of Landau levels, where $\boldsymbol{\sigma}$ is the spin operator of the band electrons, \mathbf{S}_n is the total spin operator of Mn atom occupying the position \mathbf{R}_n and $J(\mathbf{r} - \mathbf{R}_n)$ is an electron-ion exchange integral. Its matrix representation was elaborated in ref. [139] for Cd_3As_2 and for HgTe in [26].

9. Landau level structure in Bi₂Se₃

A ladder of Landau levels for bismuth selenide can be obtained by applying a routine procedure of the quantization in the magnetic field (from the section 1.7 or [73]) on the Hamiltonian (4.1) assuming $k_z = 0$ giving a spectrum of the upper block A

$$E_{A,n} = l_B^{-2}(2nC + M) \pm \sqrt{[\Delta + l_B^{-2}(C + 2nM)]^2 + 2nl_B^{-2}(\hbar v)^2} \quad (9.1)$$

and for the bottom block B

$$E_{B,n} = l_B^{-2}(2nC - M) \pm \sqrt{[\Delta + l_B^{-2}(-C + 2nM)]^2 + 2nl_B^{-2}(\hbar v)^2} \quad (9.2)$$

for $n \geq 1$ with eigenfunctions of the form $\psi_{A,n} = (a_1 |n\rangle, a_2 |n-1\rangle)^T$ and $\psi_{B,n} = (b_1 |n-1\rangle, b_2 |n\rangle)^T$. The plus sign is related to LLs of electrons whereas the minus sign to the hole LLs respectively. The zeroth Landau levels are specific and their solutions needs to be treated separately

$$E_{A,0,E} = \Delta + (C + M)l_B^{-2}, \quad E_{B,0,H} = -\Delta + (C - M)l_B^{-2} \quad (9.3)$$

with the electron $\psi_{A,0,E} = (a_1 |0\rangle, 0)^T$ and hole $\psi_{B,0,H} = (0, b_2 |0\rangle)^T$ wavefunctions.

For the perfectly parabolic bands the condition (4.3) applies which leads after the expansion in the low-field to a simple but relatively accurate LL structure

$$\begin{aligned} E_{A,n,E} &= E_{A,0,E} + n\hbar\omega_{c,E} \\ E_{B,n+1,E} &= E_{A,0,E} + n\hbar\omega_{c,E} + \hbar\omega_{c,D} \\ E_{A,n+1,H} &= E_{B,0,H} - n\hbar\omega_{c,H} - \hbar\omega_{c,D} \\ E_{B,n,H} &= E_{B,0,H} - n\hbar\omega_{c,H} \end{aligned} \quad (9.4)$$

where the cyclotron resonance energies are denoted as $\omega_{c,E} = \frac{eB}{m_e}$, $\omega_{c,H} = \frac{eB}{m_h}$, $\omega_{c,D} = \frac{eB}{m_D}$.

The main feature of the linear LL fanchart (Fig. 9.1b) is an irregularity of the pinning 1_B to 2_A in the conduction band keeping the levels 0_A and 1_A isolated from the others. For a negligible $C = 0$, the fancharts of the A and B set coincide from $n \geq 1$. An analogical situation holds for the valence band spectrum. Secondly, the zeroth level $0_{A,E}$ disperse downwards while $0_{B,H}$ goes up, which necessary leads to the crossing of levels at the critical field $B_c = \frac{\hbar\Delta}{e|M} \approx 300$ T (Fig. 9.1b). The residual out-of-plane dispersion at B_c can be easily computed from the effective sub-Hamiltonian of (4.1)

$$H_{0\text{-th LL}} = \begin{pmatrix} E_{A,0,E} & -\hbar v^\perp k_z \\ -\hbar v^\perp k_z & E_{B,0,H} \end{pmatrix} \quad (9.5)$$

giving a purely linear dependence $E_0(k_z) = \pm \hbar v^\perp |k_z|$.

Experimentally, the LL transitions were observed on an epitaxially grown 290 nm thick n-doped sample with the mobility $\mu \approx 10^3$ cm²/V.s and the initial Fermi level $E_{F0} = 15$ meV [73]. The cyclotron resonance $0_A \rightarrow 1_A$ in a quantum limit was recog-

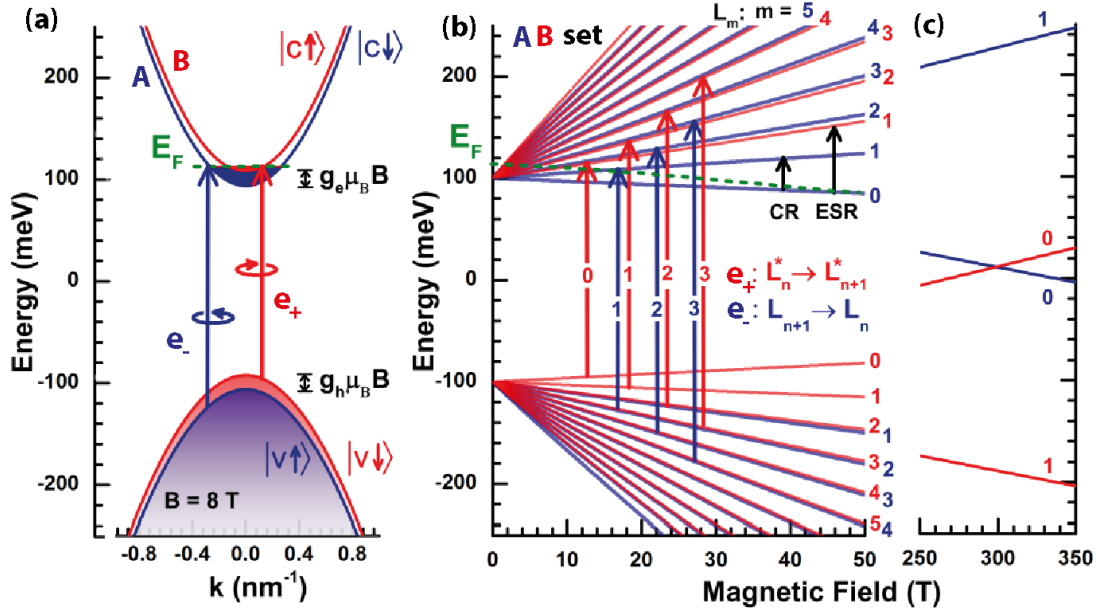


Figure 9.1: (a) In the classical regime of the low magnetic field, the band structure of Bi_2Se_3 is affected by the Zeeman splitting that lifts the degeneracy of the conduction and valence band by the same magnitude, which keeps the interband transitions equal at $k_z = 0$. In a doped system, the splitting causes a disparity between the occupation of the spin-split bands that shifts the mutual onset of the minimal transitions and brings about a circular dichroism. (b) The fanchart consists of the linearly dispersing Landau levels, where 1_B is pinned to 2_A for the conduction band and 1_A is pinned to 2_B for the valence band. This leads to the degeneracy of the transitions $L_{n+1 \rightarrow n}^A$ and $L_{n-1 \rightarrow n}^B$, while the second part of all transitions $L_{n-1 \rightarrow n}^A$, $L_{n+1 \rightarrow n}^B$ is strongly suppressed. (c) The crossing of the zeroth Landau modes is unavoidable for the inverted bands since the 0_A and 0_B disperse down and up respectively, but its realization is projected to the rather extreme field of $\approx 300 \text{ T}$ (Adopted from [73]).

nised above 18 T when the CR peak becomes clearly shaped from the α , β phonon lines (Fig. 9.2a). The linear fitting of the cyclotron mode signifies that at low energies the conduction band is fairly well parabolic and the related slope provides an electron mass $m_e = (0.14 \pm 0.05)m_0$.

Due to the presence of the mass term M in the Hamiltonian (4.1), a half of all possible transitions vanish and just one selection rule $n+1 \rightarrow n$ for A set and $n-1 \rightarrow n$ for B set is realized (appendix 7). In an approximation of the absolute electron-hole symmetry $C = 0$, the LL splitting between the A and B set is negligible and thus the transitions $L_{n+1 \rightarrow n}^A$ and $L_{n-1 \rightarrow n}^B$ are degenerated in energy, but they could be distinguished in the experiment with circularly polarized light (inset of Fig. 9.2). The interband transitions within the same set (A or B) do not conserve the spin. For example, in the A set the transition $L_{n+1 \rightarrow n}^A$ takes place from the state $|v^\uparrow\rangle$ to $|v^\downarrow\rangle$ that can be intuitively understood as a transfer of the photon momentum $L = -1$ of the \mathbf{e}_- component (Fig. 9.1a).

Within the introduced framework, one can define g-factors describing the Zeeman splitting of the spin degenerate selenium conduction band or for the bismuth valence

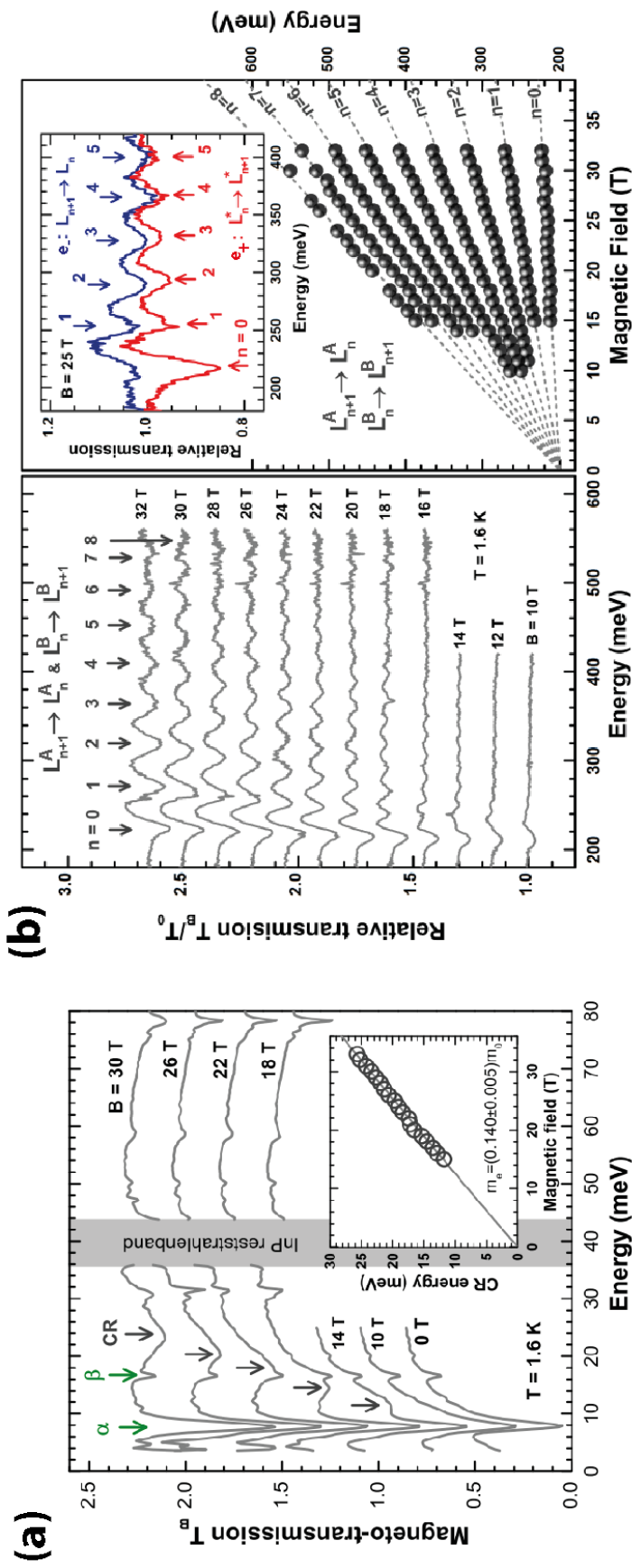


Figure 9.2: (a) A cyclotron resonance observed in the transmission on an n-doped epitaxial layer in the high magnetic field has a linear trend which hints a parabolic nature of the conduction band. (b) The interband excitations extrapolate to the common intercept of the bandgap energy 0.2 eV. The transitions are twice degenerate with respect to the set A and B. The experiment with the definite circular polarization resolved two almost identical spectral patterns that overlay for the natural light, see the inset (Adopted from [73]).

band correspondingly as

$$\begin{aligned} g_c &= \frac{1}{\mu_B B} (E_{Se,n}^\uparrow - E_{Se,n}^\downarrow) = \frac{1}{\mu_B B} (E_{B,n+1,e}^\uparrow - E_{A,n,e}^\downarrow) \\ g_v &= \frac{1}{\mu_B B} (E_{Bi,n}^\uparrow - E_{Bi,n}^\downarrow) = \frac{1}{\mu_B B} (E_{A,n+1,h}^\uparrow - E_{B,n,h}^\downarrow) \end{aligned} \quad (9.6)$$

for $n \geq 1$, where $\mu_B = \frac{e\hbar}{2m_0}$ is the Bohr magneton. The g-factors are independent of the energy since the LL spacing is equidistant for the parabolic bands. The transitions occur within the both spin families, so it is useful to complete the definition of g-factors with respect to the same set (A or B) as $g_e = g_c$ and $g_h = -g_v$. This means that the both bands from the set A (i.e. $|c^\uparrow\rangle$ and $|v^\downarrow\rangle$) split up in the magnetic field and the both bands from the set B (i.e. $|c^\downarrow\rangle$ and $|v^\uparrow\rangle$) split downwards by the same amount, which maintains the transitions $L_{n+1 \rightarrow n}^A$ and $L_{n-1 \rightarrow n}^B$ degenerate. Thus, the splitting of the absorption edge observed in the Fig. 4.5 needs to be explained purely on the basis of the disparity in the electronic occupation of $|c^\uparrow\rangle$ and $|c^\downarrow\rangle$ that leads to the dichroic properties in the optical response.

The definition (9.6) implies that the spin splitting $E_s = g\mu_B B$ in the parabolic approximation is equal to $\hbar\omega_D$ and the respective g-factor is $g_e = 2\frac{m_0}{m_D}$. Then the relation between the cyclotron energy $E_c = \hbar\omega_c$ and spin splitting becomes unusual $2E_c = E_s$, in clear distinction to a free electron in vacuum where the quantum electrodynamics dictates $g = 2$ and the both quantities are identical $E_c = E_s$. In numbers, the computed value of g-factors $g_e = g_h \approx 25$ (using effective masses) is close to the experimental values 27 [121] from the EPR resonance and 32-33 [120] determined from the NMR shift (Tab. 4.2).

10. Author's publications related to this work

- [1] M. Hakl, S. Tchoumakov, A. Akrap, I. Crasse, B. I. Piot, C. Faugeras, O. Caha, J. Novák, M. Goerbig, M. Potemski, M. Orlita et al.: *Landau level infrared spectroscopy of Kane electrons in Cd_3As_2* , submitted to Phys. Rev. X (November-2017)
- [2] M. Hakl, S. Tchoumakov, A. Akrap, I. Crasse, B. I. Piot, C. Faugeras, O. Caha, J. Novák, M. Goerbig, M. Potemski, M. Orlita et al.: *Cyclotron resonance of Kane electrons observed in Cd_3As_2* , IRMMW-THz 2017, Conference proceedings
- [3] I. Crasse, E. Martino, C. Homes, O. Caha, J. Novák, P. Tüeckmantel, M. Hakl, M. Orlita, A. Akrap et al.: *Non-uniform carrier density in Cd_3As_2 evidenced by optical spectroscopy*, submitted to Phys. Rev. B (January-2018)
- [4] A. Akrap, M. Hakl, S. Tchoumakov, I. Crassee, J. Kuba, M. Goerbig, C. Homes, C. Faugeras, G. Martinez, M. Potemski, M. Orlita et al.: *Magneto-optical signature of massless Kane electrons in Cd_3As_2* , Phys. Rev. Lett. **117**, (2016) 136401
- [5] M. Hakl, L. Ohnoutek, M. Veis, Č. Drašar, A. Materna, G. Strzelecka, A. Hruban, A. Slobodeniuk, B. I. Piot, G. Martinez, M. Potemski and M. Orlita: *Saturation of Faraday rotation in n-doped Bi_2Se_3* , Europhysics Letters **117**, (2017) 47006
- [6] L. Ohnoutek, M. Hakl, M. Veis, B. I. Piot, C. Faugeras, G. Martinez, M. Yakushev, R. W. Martin, Č. Drašar, A. Materna, G. Strzelecka, A. Hruban, M. Potemski and M. Orlita: *Strong interband Faraday rotation in Bi_2Se_3* , Scientific Report **6**, (2016) 19087
- [7] G. Martinez, B. I. Piot, M. Hakl, C. Faugeras, Y. S. Hor, Č. Drašar, A. Materna, G. Strzelecka, A. Hruban, M. Potemski and M. Orlita: *Determination of the energy bandgap of Bi_2Se_3* , Scientific Report **7**, (2017) 6891

Author's communication related to this work

- [1] International Conference on Infrared, Millimeter and Terahertz Waves, IRMMW-THz
August 2017, Cancún, Mexico
Talk: *Infrared Landau level spectroscopy of Kane electrons in Cd_3As_2*
- [2] 46-th International School & Conference on the Physics of Semiconductors, Jaszowiec 2017
June 2017, Szczyrk, Poland
Talk: *Infrared Landau level spectroscopy of Kane electrons in Cd_3As_2*
- [3] Rencontres des Jeunes Physiciens, Société Française de Physique
March 2017, Grenoble, France
Talk: *Dirac matter*
- [4] New Frontiers in 2D materials: Approaches & Applications, Winter School
January 2017, Villard de Lans, France
Poster: *Infrared Landau level spectroscopy of Kane electrons in Cd_3As_2*
- [5] Meso School of Topological matter, Interactions & Light-matter Coupling, November 2016, Cargèse, France
Poster: *Faraday rotation in Bi_2Se_3*
- [6] Conférence sur les Matériuex et Phases Topologique, October 2016, Lyon, France
Poster: *Faraday rotation in Bi_2Se_3*
- [7] 17-th International Conference on Narrow Gap Semiconductors & New Trends in Topological Insulators, July 2016, Würzburg, Germany
Poster: *Saturation effects in Bi_2Se_3*
- [8] Rencontres des Jeunes Physiciens, Société Française de Physique
April 2016, Grenoble, France
Talk: *Faraday rotation in Bi_2Se_3*

Bibliography

- [1] S. Trivedi, A. Srivastava, and R. Kurchania. *Silicene and germanene: A first principle study of electronic structure and effect of hydrogenation-passivation.* *Journal of Theoretical Computational and Theoretical NanoScience*, 11(3):781–788, 2014.
- [2] L. Matthes, P. Gori, O. Pulci, and F. Bechstedt. *Universal infrared absorbance of two-dimensional honeycomb group-IV crystals.* *Phys. Rev. B*, 87:035438, 2013.
- [3] Shun-Qing Shen. *Topological insulators - Dirac equation in condensed matter.* Springer, 2012.
- [4] F. Teppe, M. Marcinkiewicz, S. S. Krishtopenko, S. Ruffenach, C. Consejo, A. M. Kadykov, W. Desrat, and et al. *Temperature-driven massless Kane fermions in HgCdTe crystals.* *Nature Communications*, 7:12576, 2016.
- [5] P. Dziawa, B. Kowalski, K. Dybko, R. Buczko, A. Szczerbakow, and et al. *Topological crystalline insulator states in $\text{Pb}_{1-x}\text{Sn}_x\text{Se}$.* *Nat. Mat.*, 11(12):1027, 2012.
- [6] B. Duplantier, V. Rivasseau, and J.-N. Fuchs. *Dirac matter.* Birkhäuser Basel, 2017.
- [7] Jérôme Cayssol. *Introduction to Dirac materials and topological insulators.* *Comptes Rendus Physique*, 14(9–10):760 – 778, 2013.
- [8] S. M. Young, S. Zaheer, J. C. Y. Teo, C. L. Kane, E. J. Mele, and A. M. Rappe. *Dirac semimetal in three dimensions.* *Phys. Rev. Lett.*, 108:140405, 2012.
- [9] H.B. Nielsen and M. Ninomiya. *Absence of neutrinos on a lattice.* *Nuclear Physics B*, 193(1):173 – 194, 1981.
- [10] Zhijun Wang, Hongming Weng, Quansheng Wu, Xi Dai, and Zhong Fang. *Three-dimensional Dirac semimetal and quantum transport in Cd_3As_2 .* *Phys. Rev. B*, 88:125427, 2013.
- [11] Phillip Ashby. *Physics at Dirac point – The optical conductivity of Dirac materials.*
- [12] C. J. Tabert, J. P. Carbotte, and E. J. Nicol. *Optical and transport properties in three-dimensional Dirac and Weyl semimetals.* *Phys. Rev. B*, 93:085426, 2016.
- [13] B. Q. Lv, N. Xu, H. M. Weng, J. Z. Ma, P. Richard, X. C. Huang, L. X. Zhao, G. F. Chen, C. E. Matt, F. Bisti, V. N. Strocov, and et al. *Observation of Weyl nodes in TaAs.*
- [14] J. L. Mañes. *Existence of bulk chiral fermions and crystal symmetry.* *Phys. Rev. B*, 85:155118, 2012.
- [15] Bohm-Jung Yang and Naoto Nagaosa. *Classification of stable three-dimensional Dirac semimetals with nontrivial topology.* *Nature Communications*, 5:4898, 2014.

- [16] Sumathi Rao. *Weyl semimetals: a short review*. *ArXiv*, page 1603.02821, 2016.
- [17] A. Raoux, M. Morigi, J.-N. Fuchs, F. Piéchon, and G. Montambaux. *From dia- to paramagnetic orbital susceptibility of massless fermions*. *Phys. Rev. Lett.*, 112:026402, 2014.
- [18] A. D. Kovács, G. Dávid, B. Dóra, and J. Cserti. *Frequency-dependent magneto-optical conductivity in the generalized α -T₃ model*. *Phys. Rev. B*, 95:035414, 2017.
- [19] J. D. Malcolm and E. J. Nicol. *Frequency-dependent polarizability, plasmons, and screening in the two-dimensional pseudospin-1 dice lattice*. *Phys. Rev. B*, 93:165433, 2016.
- [20] J. D. Malcolm and E. J. Nicol. *Magneto-optics of massless Kane fermions: Role of the flat band and unusual Berry phase*. *Phys. Rev. B*, 92:035118, 2015.
- [21] E. Illes, J. P. Carbotte, and E. J. Nicol. *Hall quantization and optical conductivity evolution with variable Berry phase in the α -T₃ model*. *Phys. Rev. B*, 92:245410, 2015.
- [22] J. D. Malcolm and E. J. Nicol. *Analytic evaluation of Kane fermion magneto-optics in two and three dimensions*. *Phys. Rev. B*, 94:224305, 2016.
- [23] Balázs Dóra, Janik Kailasvuori, and R. Moessner. *Lattice generalization of the Dirac equation to general spin and the role of the flat band*. *Phys. Rev. B*, 84:195422, 2011.
- [24] Christian Vérié. *Narrow bandgap semiconductors*, pages 1–19. Springer Berlin Heidelberg, 1970.
- [25] M. Orlita, D. M. Basko, M. S. Zholudev, F. Teppe, W. Knap, V. I. Gavrilenko, N. N. Mikhailov, S. A. Dvoretiskii, P. Neugebauer, C. Faugeras, A.-L. Barra, G. Martinez, and M. Potemski. *Observation of three-dimensional massless Kane fermions in a zinc-blende crystal*. *Nat. Phys.*, 10(3):233–238, 2014.
- [26] E. G. Novik, A. Pfeuffer-Jeschke, T. Jungwirth, V. Latussek, C. R. Becker, G. Landwehr, H. Buhmann, and L. W. Molenkamp. *Band structure of semi-magnetic Hg_{1-y}Mn_yTe quantum wells*. *Phys. Rev. B*, 72:035321, 2005.
- [27] Michel Fruchart and David Carpentier. *An introduction to topological insulators*. *Comptes Rendus Physique*, 14(9):779 – 815, 2013.
- [28] Chao-Xing Liu, Xiao-Liang Qi, HaiJun Zhang, Xi Dai, Zhong Fang, and Shou-Cheng Zhang. *Model Hamiltonian for topological insulators*. *Phys. Rev. B*, 82:045122, 2010.
- [29] Andrei Bernevig and Taylor Hughes. *Topological insulators and topological superconductors*. Princeton university press, New Jersey, 2013.
- [30] M. König, H. Buhmann, L. Molenkamp, T. Hughes, Chao-Xing Liu, Xiao-Liang Qi, and Shou-Cheng Zhang. *The quantum spin Hall effect: theory and experiment*. *Journal of the Physical Society of Japan*, 77(3):031007, 2008.

- [31] K. S. Novoselov, A. K. Geim, S. V. Morozov, D. Jiang, Y. Zhang, Dubonos, and et al. **Electric field effect in atomically thin carbon films.** *Science*, 306(5696):666–669, 2004.
- [32] Y. Xia, D. Qian, D. Hsieh, L. Wray, A. Pal, H. Lin, A. Bansil, D. Grauer, Y. S. Hor, R. J. Cava, and M. Z. Hasan. **Observation of a large-gap topological-insulator class with a single Dirac cone on the surface.** *Nat. Phys.*, 5(6):398–402, 2009.
- [33] D. N. Basov, R. D. Averitt, D. van der Marel, M. Dressel, and K. Haule. **Electrodynamics of correlated electron materials.** *Rev. Mod. Phys.*, 83:471–541, 2011.
- [34] R. S. Kim and S. Narita. **Far-infrared interband magnetoabsorption and band structure of $\text{Hg}_{1-x}\text{Cd}_x\text{Te}$ alloys.** *Physica Status Solidi (b)*, 73(2):741–752, 1976.
- [35] P. Yu and M. Cardona. *Fundamentals of semiconductors*. Springer, Berlin Heidelberg, 1996.
- [36] R. K. Willardson and A. C. Beer. *Defects, (HgCd)Se, (HgCd)Te*. Semiconductors and semimetals, Vol. 16.
- [37] M. Orlita, I. Crassee, C. Faugeras, A. B. Kuzmenko, F. Fromm, M. Ostler, T. Seyller, G. Martinez, M. Polini, and M. Potemski. **Classical to quantum crossover of the cyclotron resonance in graphene: a study of the strength of intraband absorption.** *New Journal of Physics*, 14(9):095008, 2012.
- [38] Peter R. Griffiths and James A. de Haseth. *Fourier transform infrared spectroscopy*. Wiley-Interscience, 2007.
- [39] G. Klatt, R. Gebs, C. Janke, T. Dekorsy, and A. Bartels. **Rapid-scanning terahertz precision spectrometer with more than 6 THz spectral coverage.** *Opt. Express*, 17(25):22847–22854, 2009.
- [40] M. Beck, H. Schäfer, G. Klatt, J. Demsar, S. Winnerl, M. Helm, and T. Dekorsy. **Impulsive terahertz radiation with high electric fields from an amplifier-driven large-area photoconductive antenna.** *Opt. Express*, 18(9):9251–9257, 2010.
- [41] M. N. Ali, Q. Gibson, S. Jeon, B. B. Zhou, A. Yazdani, and R. J. Cava. **The crystal and electronic structures of Cd_3As_2 , the three-dimensional electronic analogue of graphene.** *Inorganic Chemistry*, 53(8):4062–4067, 2014.
- [42] J. Bodnar. *Band structure of Cd_3As_2 from Shubnikov de-Haas and Haas-van Alphen effects*. Conference Proceeding of Narrow Gap Semiconductors, Warsaw, 1977.
- [43] I. Rosenman. **Effet Shubnikov de Haas dans Cd_3As_2 : Forme de la surface de Fermi et modele non parabolique de la bande de conduction.** *Journal of Physics and Chemistry of Solids*, 30(6):1385–1402, 1969.
- [44] P. R. Wallace. **Electronic g-factor in Cd_3As_2 .** *Physica Status Solidi (b)*, 92(1):49–55, 1979.
- [45] M. Singh, J. Cisowski, P. R. Wallace, J. C. Portal, and J. M. Broto. **The band structure of Cd_3P_2 in the presence of a magnetic field.** *Physica Status Solidi (b)*, 114(2):481–486, 1982.

- [46] M. Singh and P. R. Wallace. Theory of the intraband magneto-optics of cadmium arsenide. *Journal of Physics C: Solid State Physics*, 16(20):3877, 1983.
- [47] B. Plenkiewicz, P. R. Wallace, and P. Plenkiewicz. The role of vacancies in the band structure of Cd_3As_2 . *Solid State Communications*, 50(7):681 – 684, 1984.
- [48] K. Sierański, J. Szatkowski, and J. Misiewicz. Semiempirical tight-binding band structure of II_3V_2 semiconductors: Cd_3P_2 , Zn_3P_2 , Cd_3As_2 , and Zn_3As_2 . *Phys. Rev. B*, 50:7331–7337, 1994.
- [49] E. K. Arushanov. Crystal growth, characterization and application of $\text{II}_3\text{-V}_2$ compounds. *Progress in Crystal Growth and Characterization*, 13(1):1–38, 1986.
- [50] Marinus Johannes Gelten. *Optical properties of Cd_3P_2 and Cd_3As_2* . Dissertation thesis, Eindhoven, 1985.
- [51] A. Narayan, D. Di Sante, S. Picozzi, and S. Sanvito. Topological tuning in three-dimensional Dirac semimetals. *Phys. Rev. Lett.*, 113:256403, 2014.
- [52] Fabien Tran and Peter Blaha. Accurate band gaps of semiconductors and insulators with a semilocal exchange-correlation potential. *Phys. Rev. Lett.*, 102:226401, 2009.
- [53] Irene Aguilera. Private communication. *Peter Grünberg Institute, Jülich*, 2017.
- [54] A. M. Conte, O. Pulci, and F. Bechstedt. Electronic and optical properties of topological semimetal Cd_3As_2 . *Scientific Reports*, 7:45500, 2017.
- [55] S. Borisenko, Q. Gibson, D. Evtushinsky, V. Zabolotnyy, B. Büchner, and R. J. Cava. Experimental realization of a three-dimensional Dirac semimetal. *Phys. Rev. Lett.*, 113:027603, 2014.
- [56] M. Neupane, S. Xu, R. Sankar, N. Alidoust, G. Bian, C. Liu, I. Belopolski, T. Chang, H. Jeng, H. Lin, A. Bansil, F. Chou, and M. Z. Hasan. Observation of a three-dimensional topological Dirac semimetal phase in high-mobility Cd_3As_2 . *Nature Communications*, 5:3786, 2014.
- [57] Z. K. Liu, J. Jiang, B. Zhou, Z. J. Wang, Y. Zhang, H. M. Weng, D. Prabhakaran, S.-K. Mo, H. Peng, and et al. A stable three-dimensional topological Dirac semimetal Cd_3As_2 . *Nat. Mater.*, 13(7):677–681, 2014.
- [58] S. Jeon, B. B. Zhou, A. Gyenis, B. E. Feldman, I. Kimchi, A. C. Potter, Q. D. Gibson, R. J. Cava, and et al. Landau quantization and quasiparticle interference in the three-dimensional Dirac semimetal Cd_3As_2 . *Nat. Mater.*, 13(9):851–856, 2014.
- [59] M. J. Aubin, L. G. Caron, and J. P. Jay-Gerin. Band structure of cadmium arsenide at room temperature. *Phys. Rev. B*, 15:3872–3878, 1977.
- [60] T. Liang, Q. Gibson, M. N. Ali, M. Liu, R. J. Cava, and N. P. Ong. Ultrahigh mobility and giant magnetoresistance in the Dirac semimetal Cd_3As_2 . *Nat. Mater.*, 14(3):280–284, 2015.

- [61] Enze Zhang, Yanwen Liu, Weiyi Wang, Cheng Zhang, Peng Zhou, Zhi-Gang Chen, Jin Zou, and Faxian Xiu. *Magnetotransport properties of Cd₃As₂ nanostructures*. *ACS Nano*, 9(9):8843–8850, 2015.
- [62] T. Schumann, M. Goyal, D. A. Kealhofer, and S. Stemmer. *Negative magnetoresistance due to conductivity fluctuations in films of the topological semimetal Cd₃As₂*. *Phys. Rev. B*, 95:241113, 2017.
- [63] Junzhi Cao, Sihang Liang, Cheng Zhang, Yanwen Liu, Junwei Huang, Zhao Jin, Zhi-Gang Chen, Zhijun Wang, Qisi Wang, Jun Zhao, Shiyan Li, Xi Dai, and et al. *Landau level splitting in Cd₃As₂ under high magnetic fields*. *Nature Communications*, 6:7779, 2015.
- [64] Shih-Ting Guo, R. Sankar, Yung-Yu Chien, Tay-Rong Chang, Horng-Tay Jeng, Guang-Yu Guo, F. C. Chou, and Wei-Li Lee. *Large transverse Hall-like signal in topological Dirac semimetal Cd₃As₂*. *Scientific Reports*, 6:27487, 2016.
- [65] P. Moll, N. L. Nair, T. Helm, A. C. Potter, I. Kimchi, A. Vishwanath, and J. G. Analytis. *Transport evidence for Fermi-arc-mediated chirality transfer in the Dirac semimetal Cd₃As₂*. *Nature*, 535(7611):266–270, 2016.
- [66] Ben-Chuan Lin, Shuo Wang, Li-Xian Wang, Cai-Zhen Li, Jin-Guang Li, Dapeng Yu, and Zhi-Min Liao. *Gate-tuned Aharonov-Bohm interference of surface states in a quasiballistic Dirac semimetal nanowire*. *Phys. Rev. B*, 95:235436, 2017.
- [67] L. Aggarwal, A. Gaurav, G. S. Thakur, Z. Haque, A. K. Ganguli, and G. Sheet. *Unconventional superconductivity at mesoscopic point contacts on the 3D Dirac semimetal Cd₃As₂*. *Nat. Mater.*, 15(1):32–37, 2016.
- [68] Roland Winkler. *Spin-orbit coupling effects in two-dimensional electron and hole systems*. Springer Berlin Heidelberg, 2003.
- [69] H. Kildal. *Band structure of CdGeAs₂ near $k = 0$* . *Phys. Rev. B*, 10:5082–5087, 1974.
- [70] A. Akrap, M. Hakl, S. Tchoumakov, I. Crassee, J. Kuba, M. O. Goerbig, C. C. Homes, O. Caha, J. Novák, F. Teppe, W. Desrat, S. Koohpayeh, L. Wu, N. P. Armitage, and et al. *Magneto-optical signature of massless Kane electrons in Cd₃As₂*. *Phys. Rev. Lett.*, 117:136401, 2016.
- [71] Sergeuï Tchoumakov. *Signatures relativistes en spectroscopie de matériaux topologiques : en volume et en surface*. Dissertation thesis, Université Paris Sud, 2017.
- [72] Y. Guldner, C. Rigaux, M. Grynberg, and A. Mycielski. *Interband $\Gamma_6 \rightarrow \Gamma_8$ Magnetoabsorption in HgTe*. *Phys. Rev. B*, 8:3875–3883, 1973.
- [73] M. Orlita, B. A. Piot, G. Martinez, N. K. Sampath Kumar, C. Faugeras, M. Potemski, C. Michel, E. M. Hankiewicz, T. Brauner, Č. Drašar, and et al. *Magneto-optics of massive Dirac fermions in bulk Bi₂Se₃*. *Phys. Rev. Lett.*, 114:186401, 2015.

- [74] R. Sankar, M. Neupane, S.-Y. Xu, C. J. Butler, I. Zeljkovic, I. Panneer Muthuselvam, F.-T. Huang, S.-T. Guo, Sunil K. Karna, M.-W. Chu, W. L. Lee, and et al. Large single crystal growth, transport property, and spectroscopic characterizations of three-dimensional Dirac semimetal Cd_3As_2 . *Scientific Reports*, 5:12966, 2015.
- [75] E. K. Arushanov. $\text{II}_3\text{-V}_2$ compounds and alloys. *Progress in Crystal Growth and Characterization of Materials*, 25(3):131–201, 1992.
- [76] A. Rambo and M. J. Aubin. The preparation and passive annealing of Cd_3As_2 platelets. *Canadian Journal of Physics*, 57(12):2093–2095, 1979.
- [77] N. Tajabor and D. R. Lovett. Etching and chemical polishing of (112) surfaces of Cd_3As_2 and Zn_3As_2 crystals. *Physica Status Solidi (a)*, 34(2):K191–K194, 1976.
- [78] R. Stepniewski, K. Pastor, and M. Grynberg. Γ_8 -bands anisotropy and selection rules for far-infrared magneto-optical transitions in HgTe . *Journal of Physics C: Solid State Physics*, 13(31):5783, 1980.
- [79] I. Crasse, E. Martino, C. Homes, O. Caha, J. Novák, P. Tückmantel, M. Hakl, M. Orlita, A. Akrap, and et al. Non-uniform carrier density in Cd_3As_2 evidenced by optical spectroscopy. *submitted to Phys. Rev. B*, 2018.
- [80] A. B. Kuzmenko. Kramers–Kronig constrained variational analysis of optical spectra. *Review of Scientific Instruments*, 76(8):083108, 2005.
- [81] S. Das Sarma and E. H. Hwang. Collective modes of the massless Dirac plasma. *Phys. Rev. Lett.*, 102:206412, 2009.
- [82] Xiang Yuan, Peihong Cheng, Longqiang Zhang, Cheng Zhang, Junyong Wang, Yanwen Liu, Qingqing Sun, Peng Zhou, David Wei Zhang, Zhigao Hu, and et al. Direct observation of Landau level resonance and mass generation in Dirac semimetal Cd_3As_2 thin films. *Nano Letters*, 17(4):2211–2219, 2017.
- [83] H. El Alaoui Lamrani and M. J. Aubin. The magneto-optical properties of Cd_3As_2 exposed to circularly polarized radiation: interband transitions. *Canadian Journal of Physics*, 65(3):199–203, 1987.
- [84] M. Hakl, S. Tchoumakov, I. Crassee, A. Akrap, B. I. Piot, and et al. Landau level spectroscopy of Kane electrons in Cd_3As_2 . *submitted to Phys. Rev. X*, 2017.
- [85] D. Neubauer, J. P. Carbotte, A. A. Nateprov, A. Löhle, M. Dressel, and A. V. Pronin. Interband optical conductivity of the (001)-oriented Dirac semimetal Cd_3As_2 . *Phys. Rev. B*, 93:121202, 2016.
- [86] G. S. Jenkins, C. Lane, B. Barbiellini, A. B. Sushkov, R. L. Carey, Fengguang Liu, J. W. Krizan, S. K. Kushwaha, Q. Gibson, Tay-Rong Chang, and et al. Three-dimensional Dirac cone carrier dynamics in Na_3Bi and Cd_3As_2 . *Phys. Rev. B*, 94:085121, 2016.
- [87] A. I. Kozlov, V. V. Sobolev, and A. F. Knjazev. Reflection spectra of two polymorphic modifications of cadmium arsenide. *Semiconductors*, 39(3):285–288, 2005.

- [88] M. Zivitz and J. R. Stevenson. Optical properties of the $\text{Cd}_3\text{As}_2\text{-Cd}_3\text{P}_2$ semiconductor alloy system. *Phys. Rev. B*, 10:2457–2468, 1974.
- [89] M. O. Goerbig, G. Montambaux, and F. Piéchon. Measure of Diracness in two-dimensional semiconductors. *Europhysics Letters*, 105(5):57005, 2014.
- [90] E. D. Palik and J. K. Furdyna. Infrared and microwave magnetoplasma effects in semiconductors. *Reports on Progress in Physics*, 33(3):1193, 1970.
- [91] S. K. Mishra, S. Satpathy, and O. Jepsen. Electronic structure and thermoelectric properties of bismuth telluride and bismuth selenide. *Journal of Physics: Condensed Matter*, 9(2):461, 1997.
- [92] Chaoyu Chen, Shaolong He, Hongming Weng, Wentao Zhang, Lin Zhao, Haiyun Liu, Xiaowen Jia, Daixiang Mou, Shanyu Liu, Junfeng He, Yingying Peng, and et al. Robustness of topological order and formation of quantum well states in topological insulators exposed to ambient environment. *Proceedings of the National Academy of Sciences*, 109(10):3694–3698, 2012.
- [93] M. Bianchi, R. d C. Hatch, Zheshen Li, P. Hofmann, Fei Song, Jianli Mi, B. B. Iversen, Z. M. Abd El-Fattah, and et al. Robust surface doping of Bi_2Se_3 by rubidium intercalation. *ACS Nano*, 6(8):7009–7015, 2012.
- [94] O. Chiatti, C. Riha, D. Lawrenz, M. Busch, S. Dusari, J. Sánchez-Barriga, A. Mogilatenko, L. V. Yashina, and et al. 2D layered transport properties from topological insulator Bi_2Se_3 single crystals and micro flakes. *Scientific Reports*, 6:27483, 2016.
- [95] T. Hanaguri, K. Igarashi, M. Kawamura, H. Takagi, and T. Sasagawa. Momentum-resolved Landau level spectroscopy of Dirac surface state in Bi_2Se_3 . *Phys. Rev. B*, 82:081305, 2010.
- [96] Peng Cheng, Canli Song, Tong Zhang, Yanyi Zhang, Yilin Wang, Jin-Feng Jia, Jing Wang, Yayu Wang, Bang-Fen Zhu, Xi Chen, Xucun Ma, Ke He, and et al. Landau quantization of topological surface states in Bi_2Se_3 . *Phys. Rev. Lett.*, 105:076801, 2010.
- [97] Haijun Zhang, Chao-Xing Liu, Xiao-Liang Qi, Xi Dai, Zhong Fang, and Shou-Cheng Zhang. Topological insulators in Bi_2Se_3 , Bi_2Te_3 and Sb_2Te_3 with a single Dirac cone on the surface. *Nat. Phys.*, 5(6):438–442, 2009.
- [98] M. S. Bahramy, P. D. C. King, A. de la Torre, J. Chang, M. Shi, L. Patthey, G. Balakrishnan, Ph Hofmann, R. Arita, N. Nagaosa, and F. Baumberger. Emergent quantum confinement at topological insulator surfaces. *Nature Communications*, 3:1159, 2012.
- [99] I. Aguilera, C. Friedrich, G. Bihlmayer, and S. Blügel. GW study of topological insulators Bi_2Se_3 , Bi_2Te_3 and Sb_2Te_3 : Beyond the perturbative one-shot approach. *Phys. Rev. B*, 88:045206, 2013.
- [100] H. Köhler and J. Hartmann. Burstein shift of the absorption edge of n- Bi_2Se_3 . *Physica Status Solidi (b)*, 63(1):171–176, 1974.

- [101] K. W. Post, B. C. Chapler, Liang He, Xufeng Kou, Kang L. Wang, and D. N. Basov. Thickness-dependent bulk electronic properties in Bi_2Se_3 thin films revealed by infrared spectroscopy. *Phys. Rev. B*, 88:075121, 2013.
- [102] G. Martinez, B. I. Piot, M. Hakl, C Faugeras, Y. S. Hor, Č Drašar, G. Materna, A. Strzelecka, and et al. Determination of the energy bandgap of Bi_2Se_3 . *Scientific Reports*, 7:6891, 2017.
- [103] Wang-Kong Tse and A. H. MacDonald. Magneto-optical and magnetoelectric effects of topological insulators in quantizing magnetic fields. *Phys. Rev. B*, 82:161104, 2010.
- [104] M. Orlita and M. Potemski. Dirac electronic states in graphene systems: optical spectroscopy studies. *Semiconductor Science and Technology*, 25(6):063001, 2010.
- [105] C. Faugeras, M. Amado, P. Kossacki, M. Orlita, M. Kühne, A. Nicolet, Y. Latyshev, and M. Potemski. Magneto-Raman scattering of graphene on graphite: electronic and phonon excitations. *Phys. Rev. Lett.*, 107:036807, 2011.
- [106] Y. Ikebe, T. Morimoto, R. Masutomi, T. Okamoto, H. Aoki, and R. Shimano. Optical Hall effect in the integer quantum Hall regime. *Phys. Rev. Lett.*, 104:256802, 2010.
- [107] R. Shimano, G. Yumoto, J. Y. Yoo, R. Matsunaga, S. Tanabe, H. Hibino, T. Morimoto, and H. Aoki. Quantum Faraday and Kerr rotations in graphene. 4:1841, 2013.
- [108] L. Wu, W. Tse, M. Brahlek, C. M. Morris, R. V. Aguilar, N. Koirala, S. Oh, and N. P. Armitage. High-resolution Faraday rotation and electron-phonon coupling in surface states of the bulk-insulating topological insulator $\text{Cu}_{0.02}\text{Bi}_2\text{Se}_3$. *Phys. Rev. Lett.*, 115:217602, 2015.
- [109] L. Wu, M. Salehi, N. Koirala, J. Moon, S. Oh, and N. P. Armitage. Quantized Faraday and Kerr rotation and axion electrodynamics of a 3D topological insulator. *Science*, 354(6316):1124–1127, 2016.
- [110] Y. Shao, K. W. Post, J. Wu, S. Dai, A. J. Frenzel, A. R. Richardella, J. S. Lee, N. Samarth, M. M. Fogler, A. V. Balatsky, D. E. Kharzeev, and D. N. Basov. Faraday rotation due to surface states in the topological insulator $(\text{Bi}_{1-x}\text{Sb}_x)_2\text{Te}_3$. *Nano Letters*, 17(2):980–984, 2017.
- [111] Bartłomiej Wiendlocha. Resonant Levels, Vacancies, and Doping in Bi_2Te_3 , $\text{Bi}_2\text{Te}_2\text{Se}$, and Bi_2Se_3 Tetradymites. *Journal of Electronic Materials*, 45(7):3515–3531, 2016.
- [112] H. Köhler. Conduction band parameters of Bi_2Se_2 from Shubnikov-de Haas investigations. *Physica Status Solidi (b)*, 58(1):91–100, 1973.
- [113] M. Stordeur, K. K. Ketavong, A. Priemuth, H. Sobotta, and V. Riede. Optical and electrical investigations of n-type Bi_2Se_3 single crystals. *Physica Status Solidi (b)*, 169(2):505–514, 1992.

- [114] J. G. Analytis, Jiun-Haw Chu, Yulin Chen, F. Corredor, R. D. McDonald, Z. X. Shen, and I. R. Fisher. Bulk Fermi surface coexistence with Dirac surface state in Bi_2Se_3 : A comparison of photoemission and Shubnikov-de Haas measurements. *Phys. Rev. B*, 81:205407, 2010.
- [115] A. B. Sushkov, G. S. Jenkins, D. C. Schmadel, N. P. Butch, J. Paglione, and H. D. Drew. Far-infrared cyclotron resonance and Faraday effect in Bi_2Se_3 . *Phys. Rev. B*, 82:125110, 2010.
- [116] H. Gobrecht and S. Seeck. Abhängigkeit der effektiven Masse von der Ladungsträgerkonzentration im Bi_2Se_3 . *Zeitschrift für Physik*, 222(1):93–104, 1969.
- [117] K. Eto, Z. Ren, A. A. Taskin, K. Segawa, and Y. Ando. Angular-dependent oscillations of the magnetoresistance in Bi_2Se_3 due to the three-dimensional bulk Fermi surface. *Phys. Rev. B*, 81:195309, 2010.
- [118] N. P. Butch, K. Kirshenbaum, P. Syers, A. B. Sushkov, G. S. Jenkins, H. D. Drew, and J. Paglione. Strong surface scattering in ultrahigh-mobility Bi_2Se_2 topological insulator crystals. *Phys. Rev. B*, 81:241301, 2010.
- [119] B. A. Piot, W. Desrat, D. K. Maude, M. Orlita, M. Potemski, G. Martinez, and Y. S. Hor. Hole Fermi surface in Bi_2Se_3 probed by quantum oscillations. *Phys. Rev. B*, 93:155206, 2016.
- [120] S. Mukhopadhyay, S. Krämer, H. Mayaffre, H. F. Legg, M. Orlita, C. Berthier, M. Horvatić, G. Martinez, M. Potemski, B. A. Piot, A. Materna, and et al. Hyperfine coupling and spin polarization in the bulk of the topological insulator Bi_2Se_3 . *Phys. Rev. B*, 91:081105, 2015.
- [121] A. Wolos, S. Szyszko, A. Drabinska, M. Kaminska, S. G. Strzelecka, A. Hruban, A. Materna, M. Piersa, J. Borysiuk, and et al. g-factors of conduction electrons and holes in Bi_2Se_3 three-dimensional topological insulator. *Phys. Rev. B*, 93:155114, 2016.
- [122] A. D. LaForge, A. Frenzel, B. C. Pursley, Tao Lin, Xinfei Liu, Jing Shi, and D. N. Basov. Optical characterization of Bi_2Se_3 in a magnetic field: Infrared evidence for magnetoelectric coupling in a topological insulator material. *Phys. Rev. B*, 81:125120, 2010.
- [123] N. W. Ashcroft and N. D. Mermin. *Solid State Physics*. Saunders College, Philadelphia, 1976.
- [124] I. M. Boswarva, R. E. Howard, and Lidiard A. B. Faraday effect in semiconductors. *Proc. Roy. Soc., Ser. A(Math. 269)*:125–141, 1962.
- [125] A. Sklenár, C. Drašar, A. Krejcová, and P. Losták. Optical properties of $\text{Bi}_2\text{Se}_{3-x}\text{As}_x$ single crystals. *Crystal Research and Technology*, 35(9):1069–1076, 2000.
- [126] Wikipedia. Faraday effect.

- [127] P. Leubner, L. Lunczer, C. Brüne, H. Buhmann, and L. W. Molenkamp. Strain engineering of the band gap of HgTe quantum wells using superlattice virtual substrates. *Phys. Rev. Lett.*, 117:086403, 2016.
- [128] Yi Zhang, Ke He, Cui-Zu Chang, Can-Li Song, Li-Li Wang, Xi Chen, Jin-Feng Jia, Zhong Fang, Xi Dai, Wen-Yu Shan, Shun-Qing Shen, Qian Niu, and et al. Crossover of the three-dimensional topological insulator Bi₂Se₃ to the two-dimensional limit. *Nat. Phys.*, 6(8):584–588, 2010.
- [129] Phillip E. C. Ashby and J. P. Carbotte. Chiral anomaly and optical absorption in Weyl semimetals. *Phys. Rev. B*, 89:245121, 2014.
- [130] D. T. Son and B. Z. Spivak. Chiral anomaly and classical negative magnetoresistance of Weyl metals. *Phys. Rev. B*, 88:104412, 2013.
- [131] P. E. C. Ashby and J. P. Carbotte. Magneto-optical conductivity of Weyl semimetals. *Phys. Rev. B*, 87:245131, 2013.
- [132] K. Suzuki and J. C. Hensel. Quantum resonances in the valence bands of germanium. I. Theoretical considerations. *Phys. Rev. B*, 9:4184–4218, 1974.
- [133] Alexander Pfeuffer-Jeschke. *K.p theory of HgCdTe quantum wells*. Dissertation thesis, Würzburg University, 2000.
- [134] R. Yoshizaki and S. Tanaka. Magnetic sub-band structure of HgTe under uniaxial stress. *Solid State Communications*, 20(9):909 – 912, 1976.
- [135] Cheng Zhang, Jianping Sun, Fengliang Liu, Awadhesh Narayan, Nana Li, Xiang Yuan, Yanwen Liu, Jianhong Dai, Youwen Long, Yoshiya Uwatoko, and et al. Evidence for pressure-induced node-pair annihilation in Cd₃As₂. *ArXiv*, 1612.05874, 2016.
- [136] Enze Zhang, Yanwen Liu, Weiyi Wang, Cheng Zhang, Peng Zhou, Zhi-Gang Chen, Jin Zou, and Faxian Xiu. Magnetotransport properties of Cd₃As₂ nanostructures. *ArXiv*, 1503.00422, 2016.
- [137] S. Uchida and S. Tanaka. Far infrared magneto-optical effects in HgTe. *Journal of the Physical Society of Japan*, 40(1):118–127, 1976.
- [138] R. Yoshizaki and S. Tanaka. Uniaxial Stress Effect of Magneto-Optical Properties of HgTe. *Journal of the Physical Society of Japan*, 42(5):1601–1608, 1977.
- [139] J. J. Neve, J. Kossut, C. M. van Es, and F. A. P. Blom. Landau levels in anisotropic (Cd_{1-x}Mn_x)₃As₂ alloys. *Journal of Physics C: Solid State Physics*, 15(23):4795, 1982.
- [140] Kozlov, D. A. and Bauer, D. and Ziegler, J. and Fischer, R. and Savchenko, M. L. and Kvon, Z. D. and Mikhailov, N. N. and Dvoretzky, S. A. and Weiss, D. Probing quantum capacitance in a 3D topological insulator. *Phys. Rev. Lett.*, 116:166802, 2016.

- [141] B. Buttner, C. X. Liu, G. Tkachov, E. G. Novik, C. Brune, H. Buhmann, E. M. Hankiewicz, P. Recher, B. Trauzettel, S. C. Zhang, and L. W. Molenkamp. *Single valley Dirac fermions in zero-gap HgTe quantum wells*. *Nat. Phys.*, 7(5):418–422, 2011.
- [142] Clement Faugeras. *Magneto-optical study of 2D systems with high densities*. Dissertation thesis, High Magnetic Field Laboratory, Grenoble, 2003.
- [143] P. J. Lin-Chung. *Energy band structures of Cd₃As₂ and Zn₃As₂*. *Phys. Rev.*, 188:1272–1280, 1969.
- [144] L. Zdanowicz and T. Kwiecien. *Some optical properties of thin Cd₃As₂ films*. *Vacuum*, 27(4):409 – 412, 1977.
- [145] M. Iwami, M. Yoshida, and K. Kawabe. *Infrared optical absorption in Cd₃As₂*. *Japanese Journal of Applied Physics*, 12(8):1276, 1973.
- [146] F. P. Missell and M. S. Dresselhaus. *Study of the optical Shubnikov-de Haas effect*. *Phys. Rev. B*, 5:1364–1382, 1972.
- [147] Y. Liu, Y. Y. Li, S. Rajput, D. Gilks, L. Lari, P. L. Galindo, M. Weinert, V. K. Lazarov, and L. Li. *Tuning Dirac states by strain in the topological insulator Bi₂Se₃*. *Nat. Phys.*, 10(4):294–299, 2014.